Components and Metrology for Terahertz Imaging

by

Charles Robert Dietlein

B.S., Seattle Pacific University, 2003

M.S., University of Colorado, 2005

A thesis submitted to the

Faculty of the Graduate School of the

University of Colorado in partial fulfillment

of the requirements for the degree of

Doctor of Philosophy

Department of Electrical and Computer Engineering

2008

ProQuest LLC
789 East Eisenhower Parkway
P.O. Box 1346
Ann Arbor, MI 48106-1346

This thesis entitled:

Components and Metrology for Terahertz Imaging

written by Charles Robert Dietlein

has been approved for the Department of Electrical and Computer Engineering

Zoya Popović

Erich N. Grossman

Date

The final copy of this thesis has been examined by the signatories, and we

Find that both the content and the form meet acceptable presentation standards

Of scholarly work in the above mentioned discipline.

Dietlein, Charles Robert (Ph.D., Electrical Engineering)

Components and Metrology for Terahertz Imaging

Thesis directed by Professor Zoya Popović

This thesis addresses detectors, components, and calibration tools for both passive and active imaging systems and radiometers in the millimeter-wave and terahertz frequency range from approximately $f = (75–110)$ GHz to $f = (2–3)$ THz. The components developed in this work combine techniques from both the microwave and infrared ranges of the electromagnetic spectrum.

To date, there have been no standardized methods for measuring detector responsivity in the millimeter-wave/terahertz frequency range. This thesis describes a new water-based calibration source that uses the unique properties of water in this frequency range combined with "optical trap" methods from the infrared and visible regions of the spectrum. The calibration source has an uncertainty of less than ±200 mK in the range of $f = (75–450)$ GHz.

Antenna-coupled microbolometers, a specific form of direct thermal detectors, are characterized in this thesis; device responsivity and antenna patterns are measured; Nb and NbN are compared side-by-side. Using these detectors, measurements of expanded polystyrene foam are performed. Low-level forward scattering (grating lobes) are observed from this nominally random matrix of expanded polystyrene spheres. Additionally, images are acquired with these passive detectors. In this frequency range, clothing and other materials are quite transparent, making the detectors highly useful for concealed threat detection when integrated with a suitable imaging system.

In addition to broadband passive imaging, a fundamental component for monostatic active imaging systems was investigated. Specifically, a quasi-optical linear-to-circular polarizer at $f = 95$ GHz is developed in this thesis, with a loss of 0.4 dB and axial ratio of 0.23 dB.

In summary, the contributions of this thesis pave the way for standardized measurements for a variety of components useful in passive and active direct-detection imaging systems at millimeter-wave and terahertz frequencies.

DEDICATION

To my family.

PERSONAL ACKNOWLEDGMENTS

I owe to the current and former students in our research group who made the day-to-day mundanity of graduate school survivable my genuine appreciation: Dr. Patrick Bell, Dr. Alan Brannon, Dr. Jason Breitbarth, Dr. Michael Buck, Jonathan Chisum, Evan Cullens, Negar Ehsan, Mike Elsbury, Erez Falkenstein, Dr. Michael Forman, Dr. Joseph Hagerty, John Hoversten, Miloš Janković, Nicola Kinzie, Dr. Néstor López, Dr. Hung Loui, Dr. Milan Lukić, Qianli Mu, John O'Brien, Dr. Srdjan Pajić, Mabel Ramírez, Dr. Sébastien Rondineau, Luke Sankey, Aaron Scher, Jason Shin, Dr. Wayne Shiroma, Dr. Kenneth Vanhille, Christi Walsh, Dr. Narisi Wang, and our never-tiring administrative staff, including Jarka Hladišová, Adam Sadoff, and Rachael Tearle.

The ski resort and backcountry hut trips, the road cycling and mountain biking, the barbecues, Amante, Southern Sun, Mountain Sun, the former Trilogy, and the giant gin and tonic parties will never be forgotten.

PROFESSIONAL ACKNOWLEDGMENTS

My extreme gratitude is bestowed upon Professor Zoya Popović, who has, without fail, always provided motivation, opportunity, an amazing research group, and a lively lab environment. Without her, none of this would have had a remote chance of happening.

I sincerely thank Dr. Erich N. Grossman for providing support and guidance throughout the past three years, since I started working at NIST in June 2005 under my NSF grant. Both his wisdom and impetus to do science "right" are ideals that I strive to reach every day.

I am deeply grateful to the countless others who have been instrumental in the completion of this thesis, including Dr. Arttu Luukanen (VTT Technical Research Centre of Finland), Dr. Jon Eyvindur Bjarnason (formerly at UCSB, now a post-doc at NIST), my other colleagues at NIST including Dr. Aaron Miller, and those at VTT. Last but not least, a big "thank you" to my committee members for their time and energy spent both teaching me and listening to me.

CONTENTS

List of Tables

List of Figures

CHAPTER 1

INTRODUCTION

To be pleased with one's limits is a wretched state.

—Johann Wolfgang von Goethe

A thinker sees his own actions as experiments and questions—as attempts to find out something. Success and failure are for him answers above all.

—Friedrich Wilhelm Nietzsche

CONTENTS

1.1 SCOPE OF THIS THESIS

We are at the frontier of a new chapter in sensing and imaging. While many categories of imaging systems—also known as cameras—exist for wavelengths including x-ray, visible, infrared, millimeter-wave, microwave & UHF radar, in the frequency range between $f = 100\,\mathrm{GHz}$ and $f = 10\,\mathrm{THz}$ they are still in their infancy. Spectroscopic techniques are also highly advanced in the microwave [1] and infrared. For frequencies above several terahertz, constraints on distance due to high atmospheric attenuation [2, 3] will greatly limit adoption for terrestrial applications, but below several terahertz, standoff applications at distances up to hundreds of meters in both imaging and spectroscopy are quite attractive. Many materials in this frequency range contain highly interesting features. Some substances and materials that are transparent at visible wavelengths are completely opaque in the millimeter-wave/terahertz frequency range (such as water [4]), some *vice versa* (such as expanded polystyrene foam [5]), and many gases and explosives have unique spectral signatures [6].

This thesis discusses the design, implementation, and characterization of some components utilized in passive bolometric millimeter-wave/terahertz frequency imagers. These imaging systems differ primarily in their number of simultaneously operating detectors; the first-generation system has a single detector, the second has eight, and the third has 128. Additionally, the 128-detector system utilizes conical scanning, rather than the raster scanning employed by the other two systems. They are all operated cryogenically (in order to achieve the necessary temperature resolution when used indoors) in the range of $T = (2.5\text{–}5.5)\,\mathrm{K}$, but each has its own cryostat, electronics readout system, wiring, infrared filtering, optics, and mechanical design. The antenna-coupled microbolometers with which these systems detect blackbody radiation are examined in this thesis. The unique (broadband) information content of the resulting images acquired by these systems is explained and discussed in detail. Measurements of a common structural material—expanded polystyrene foam—for systems in the rf through low terahertz frequency range are detailed. Additionally, a quasi-optical W-band polarization converter and isolator that is fundamental to active imaging systems in this frequency regime is discussed at length. A metrological infrastructure is not yet well-developed in the millimeter-wave/terahertz frequency range. In order to characterize detectors for a passive millimeter-wave imaging program [7], a new water-based blackbody calibration source was developed and is applicable to a variety of laboratory-based calibration measurements, from below $f = 100\,\mathrm{GHz}$ to over $f = 1\,\mathrm{THz}$.

The contributions of this thesis include can be summarized as follows:

- The first detailed dc and rf comparison of Nb and NbN suspended air/vacuum bridge bolometers operated at both room and cryogenic temperatures [8, 9],
- The development of a new calibration source for the millimeter-wave/terahertz frequency regime [10, 11],
- The first comprehensive measurements and phenomenology of the transmission, reflection, and scattering properties of expanded polystyrene foam [12],
- Investigation of the phenomenology of passive millimeter-wave/terahertz images taken with the above-mentioned imaging systems [13], plus examples of image processing [14, 15], and
- Explanation of the design and testing of a quasi-optical component that is fundamental in *active* imaging systems [16].

1.2 The electromagnetic spectrum

Because the imaging systems that this work is devoted to are primarily operated in the passive modality—much like x-ray, visible, and infrared cameras—it is important to be familiar with the spectra of radiation as a function of frequency and temperature. All objects in the universe emit a quantifiable electromagnetic spectrum, governed by Planck's law of blackbody radiation. As a function of frequency and temperature, Planck's law of blackbody radiation is

$$L_f\left(f,T\right)=\frac{2hf^3}{c^2}\frac{1}{e^{\frac{hf}{k_BT}}-1}\quad[\mathrm{W}\cdot\mathrm{m}^{-2}\cdot\mathrm{Hz}^{-1}\cdot\mathrm{sr}^{-1}],\tag{1.1}$$

where L_f is the spectral radiance emitted by a blackbody at physical temperature T, f is frequency, c is the speed of light in a vacuum, h is Planck's constant, and k_B is Boltzmann's constant. The Planck relations apply strictly to "black" objects, i.e., those with emissivity $\epsilon = 1$. Alternatively, Planck's law can be written as a function of free-space wavelength $\lambda = c/f$ and temperature:

$$L_\lambda\left(\lambda,T\right)=\frac{2hc^2}{\lambda^5}\frac{1}{e^{\frac{hc}{\lambda k_BT}}-1}\quad[\mathrm{W}\cdot\mathrm{m}^{-3}\cdot\mathrm{sr}^{-1}].\tag{1.2}$$

The units of spectral radiance (see Table 1.5) in both (1.1) and (1.2) differ because one is a function of frequency and one is a function of wavelength. Depicted in Figure 1.1 are blackbody spectra curves for four temperatures of objects we are familiar with; their frequency of peak blackbody emission is calculable from Wien's law:

$$f_{peak}\approx T\cdot 5.88\times 10^{10}\quad[\mathrm{Hz}].\tag{1.3}$$

Figure 1.1 contains additional information, related to both standard microwave bands and classical infrared imaging regions. Typical infrared or thermal imaging is performed in the "thermal" or "long-wave" ($\lambda \approx 10\,\mu\mathrm{m}$) infrared region, where the the blackbody radiation spectrum has a peak at human body temperature. Closely related are night-vision devices, also known as illuminators, operating at $\lambda \approx 1\,\mu\mathrm{m}$. They essentially amplify the existing ambient light that our eyes do not detect, so they cannot be used in completely darkness unless an infrared light source is utilized. Due to the fact that the sun effectively peaks around $T = 5780\,\mathrm{K}$, the majority of the radiation around and on our planet corresponds to what we see as visible light, thus, the wavelengths that our eyes are most sensitive to. Similarly, the heat from a campfire is sensed by an excellent temperature detector in the infrared—our skin.

The frequency range considered here is denoted as "millimeter-wave and terahertz," covering $f = 100\,\mathrm{GHz}$ through nearly $f = 4\,\mathrm{THz}$. This range, and up to $f = 10\,\mathrm{THz}$, is the last

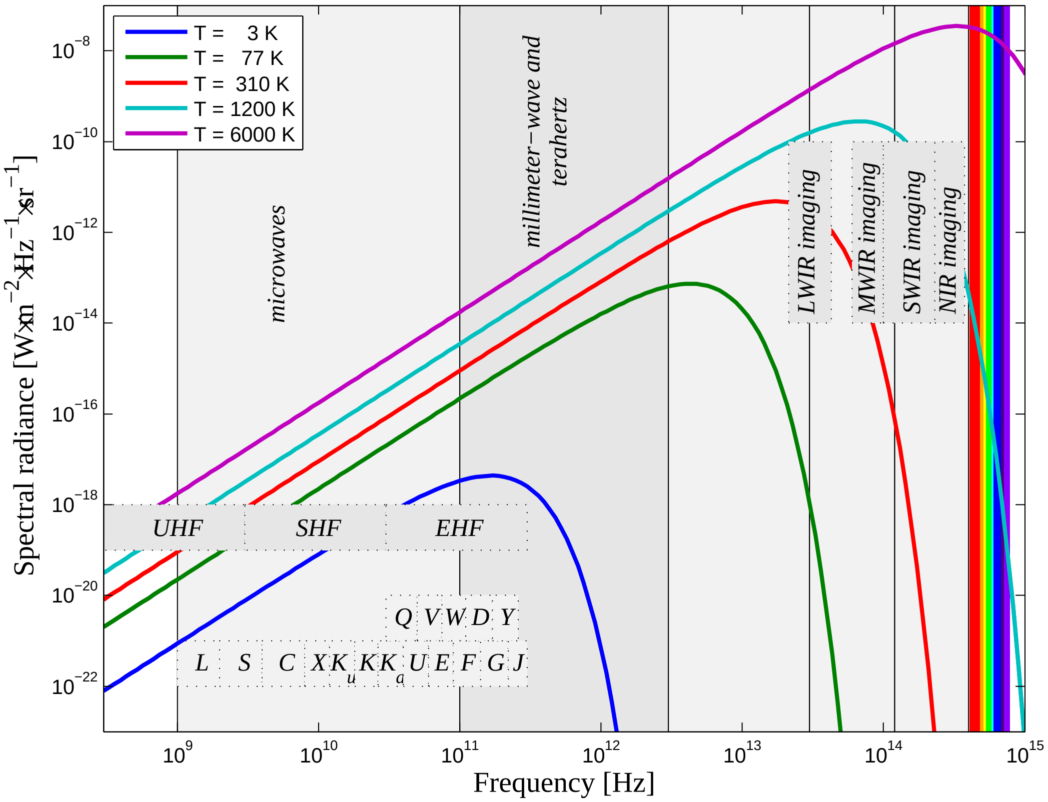

Figure 1.1: Planck's law of blackbody radiation plotted for four temperatures as a function of frequency. $T = 3\,\mathrm{K}$ is the cosmic microwave background temperature, $T = 310\,\mathrm{K}$ is human body temperature, $T = 1200\,\mathrm{K}$ is the approximate temperature of a wood-based fire, and $T = 6000\,\mathrm{K}$ is the temperature of the surface of the sun. The region denoted "millimeter-wave and terahertz" is the frequency range in which the work in this thesis resides.

electromagnetic region, the "final frontier," for which sources and detectors are being developed; even now, sources above several hundred gigahertz are low-power (below several milliwatts) and realized by either frequency multiplier chains [17], vacuum tubes such as backward wave oscillators (BWO), or quantum cascade lasers (QCL) [18], none of which have *yet* shown the ability to capture the playing field. Micromachined vacuum electronic sources are one example of a new source that may become a contender [19]. Detectors in this frequency range are usually based on some form of bolometer, zero-bias diode, or superconducting junction; a specific implementation of the former is used as the detector in the imaging systems discussed in this thesis, and detailed in Chapter 2.

The Rayleigh-Jeans approximation (i.e., $hf/k_BT \ll 1$) to Planck's law can be used in the frequency range of the work in this thesis. Figure 1.2 compares spectral radiance between the exact Planck's law, the Rayleigh-Jeans approximation, and the Wien approximation. The Rayleigh-Jeans approximation is, as a function of frequency,

$$L_f(f,T) = \frac{2k_B T f^2}{c^2} \quad [\mathrm{W} \cdot \mathrm{m}^{-2} \cdot \mathrm{sr}^{-1} \cdot \mathrm{Hz}^{-1}]. \tag{1.4}$$

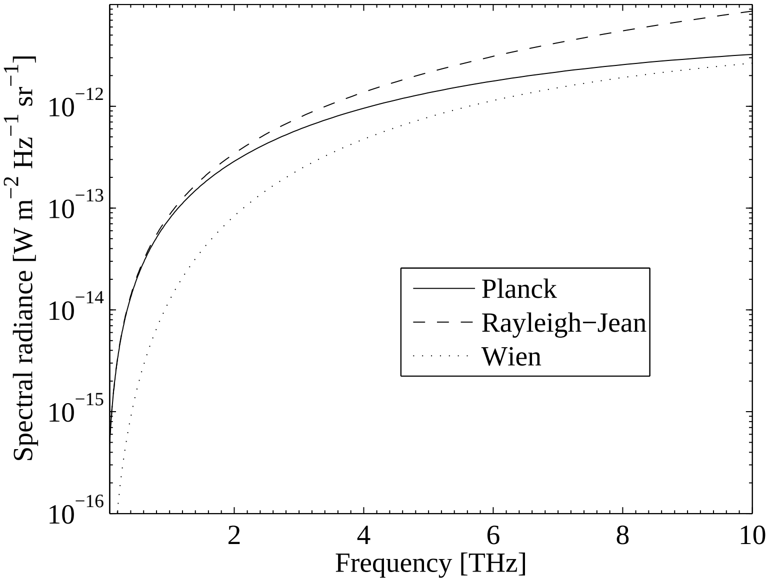

Figure 1.2: A comparison of spectral radiance calculated from Planck's law, the Rayleigh-Jean approximation, and the Wien approximation, for a blackbody at $T = 295\,\mathrm{K}$. In the millimeter-wave/terahertz frequency range covered in this thesis (up to $f \approx 4\,\mathrm{THz}$), the Rayleigh-Jeans approximation is considered valid for objects near room temperature.

1.3 IMAGING HISTORY

The term "imaging" refers to the process of producing images, or any sort of spatial representation—usually two-dimensional—of a physical object or scene of objects. The most basic image includes only intensity data per pixel, e.g. an image produced from black-and-white film. This data set clearly contains no spectral information. A slightly more complex data set, containing e.g. red, green, and blue pixel information, can also be viewed in a two-dimensional plane—a typical color photograph. Imaging is further commonly categorized: photography (digital or film for common everyday use), medical imaging (radiographs, tomography, ultrasound), microscopy (scanning electron microscopes, atomic force microscopes), or radar (weather, satellite-based, synthetic aperture radar).

The earliest known photograph was produced by Nicéphore Niépce in 1826. By 1840, William Talbot had devised the negative, coating paper sheets with silver chloride, allowing positive prints to be reproduced much like film used today. An interesting fact for electromagnetics engineers and physicists is that James Clerk-Maxwell produced the first permanent color photograph in 1861 (Figure 1.3). 147 years later, we now see false-color weather radar images of clouds, wind and rain, x-ray images of broken bones, x-ray backscatter images for security screening, thermal or radar images for military use on the battlefield, high-resolution visible and infrared (including hyperspectral) images of the earth taken from satellite orbit, as well as scanning electron microscopy, ultrasound (an application of acoustic imaging), and many other categories too numerous to list here.

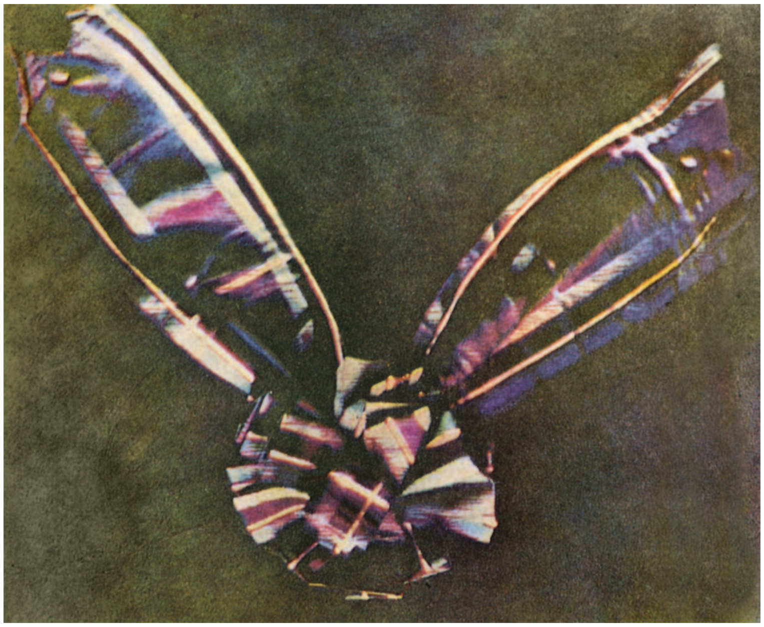

Figure 1.3: The first permanent color photograph, taken by James Clerk-Maxwell. The tartan ribbon, tied into a bow, was photographed three times—each time with a different filter in place. The photographic plates exist today in a museum in Scotland—the house in which Maxwell was born.

Other than the end use or application of each image, of interest to us is the frequency range of the data which make up the image. Frequencies substantially distant from the visible light region can contain information which is quite different from what we are used to observing. The visibility of any object at a specific frequency is a function of its material properties and scattered, transmitted, absorbed, and reflected radiation, as well as the imaging modality employed—the two most simplistic classes being either passive or active. In passive imaging, which is a specific sub-field of radiometry, the radiometric temperature of an object at a specific frequency, $T_{rad}(f)$, is usually approximated by

$$T_{rad}(f) = \epsilon(f)T_{obj} + [1 - \epsilon(f)]T_{bg} \quad \text{[K]}, \tag{1.5}$$

where T_{obj} is the physical temperature of the object, $\epsilon(f)$ is the emissivity of the object, and T_{bg} is the physical temperature of the surrounding scene, or background. An immediate conclusion can be drawn from this simple formula, which is that the visibility of the object is due to the radiometric temperature difference between the object and the background. An expansion of this trivial expression will be discussed in Chapter 6. The emissivity $\epsilon(f)$ is frequency-dependent, and whether or not one considers this a positive aspect, varies enough in the millimeter-wave/terahertz frequency range for materials of interest that multispectral imaging becomes attractive.

In active imaging systems such as radar, the visibility of an object is deduced from similar concepts; the primary difference is that an active source is utilized to provide the illumination that in passive imaging is merely the surrounding background scene radiance. In the active modality, reflectivity is a more important parameter than transmissivity or emissivity (critical in the passive modality). An important distinction should be made at this point: when the term "passive" is used in this thesis, it is meant that no artificial illumination whatsoever is used. Several published papers have applied "passive" to refer to radiometric imagers in which additional temperature contrast is attained by the use of a diffuse source providing orders of magnitude greater irradiance than would otherwise be found in the scene, e.g., liquid nitrogen cooled walls in a portal-based imaging system for security screening [20].

Table 1.1: Comparison of passive imaging modalities

technology	sensitivity	price	max. frequency [GHz]
coherent heterodyne	good	huge	> 1000
coherent direct (with pre-amp)	good	high	200
cryogenic antenna-coupled microbolometers	good	medium	> 1000
incoherent direct (no pre-amp)	medium	low	600
300 K antenna-coupled microbolometers	poor	very low	> 1000

1.4 PREVIOUS AND PARALLEL WORK

The first publication of the detector highlighted in this thesis—the hotspot antenna-coupled microbolometer—was in 2003 [21], implying that this technology is relatively new. But as discussed in the beginning of Chapter 2, this detector was the product of many earlier studies. In the imaging realm—at the system level—a large body of prior and existing work should be acknowledged. Many passive and active systems in the millimeter-wave, terahertz, and long-wave infrared regions utilize similar concepts (or in the case of x-ray backscatter, produce images which appear similar to the end user) in terms of imaging systems and applications. Existing technologies and systems are listed here, categorized by modality. Table 1.1 compares the passive imaging modalities, which provide the most similar images to those discussed in this thesis (Chapter 6). Active imaging in the millimeter-wave/terahertz frequency range has been compared to looking around in a dark room with a spotlight; images acquired in the active modality contain severe specular reflections, and require extensive signal processing in order to achieve the natural appearance native to passive images.

1.4.1 MICROWAVE/MILLIMETER-WAVE ACTIVE IMAGING

A part of this thesis is directly applicable to a W-band ($f = 95\,\mathrm{GHz}$) system utilizing 128 detectors—each an air-bridge bolometer at the feedpoint of a slot-ring antenna [22]—and a conically-scanned linear array, designed by Grossman et al. [23]; it is a standoff system with a range of several meters. The quasi-optical polarizer/isolator discussed in Chapter 5 is a critical component in this system.

The most impressive example of a system operating in the microwave region ($f = 30\,\mathrm{GHz}$, in this case) is the holgraphic three-dimensional system developed at Pacific Northwest National Laboratory (PNNL) [24, 25]. This system utilizes phase information to achieve high resolution at these relatively low frequencies, and cylindrically (via mechanical rotation of antenna arrays) scans the individual in a single-person portal. The scan requires between (2–10) s, and has a spatial resolution of better than 1 mm. The Transportation Security Administration (TSA) recently announced that 30 of these systems will soon be installed in test programs at several airports in the USA. An example image taken by one of these systems of a mannequin with concealed objects beneath its clothing is shown in Figure 1.4.

Figure 1.4: Image from an active $f = (27\text{–}33)$ GHz holographic imaging system, developed at PNNL. The test subject is a mannequin with concealed objects beneath its clothing, and a weapon in its hand. Image taken from [25].

1.4.2 Passive heterodyne imaging

Most radio astronomy is performed using passive heterodyne systems, as they allow accurate and precise measurements of the content of stars and galaxies. A number of passive heterodyne systems are currently being developed for terrestrial imaging, however. One current example is a hot-electron bolometer system operated at $f = 850\,\text{GHz}$ [26], which has a spatial resolution of 4 mm and a temperature resolution of 0.5 K. The local oscillator (LO) is a frequency multiplier chain from Virginia Diodes.

An example image from a $f = 640\,\text{GHz}$ Schottky diode mixer system [27] is shown in Figure 1.5. This waveguide-based detector was originally built as part of the prototype spectrometer for a space-borne mission; the mixer is a subharmonically pumped double-sideband design, with an integrated X-band IF amplifier, and the LO chain is a tripled Gunn oscillator.

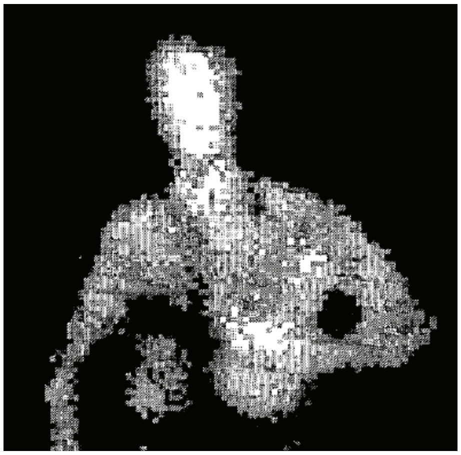

Figure 1.5: Image from a passive, single-pixel, heterodyne, Schottky diode system. A metal wrench concealed underneath the shirt can be seen as a dark shape on the left side. Image taken from [27].

1.4.3 Passive direct microwave/millimeter-wave imaging

Developments in this category are more extensive than in the other categories; several examples follow. In 1992, Goldsmith et al. [28] demonstrated a dual-mode (active and passive) imaging system at $f \approx 140\,\text{GHz}$, and successfully imaged mannequins (active) and human subjects (passive) with concealed objects beneath their clothing. Also in the early 1990s, TRW Inc. was developing a 1040-detector (40×26), video rate passive camera, for operation between $f = 84\,\text{GHz}$ and $f = 94\,\text{GHz}$. The MMIC is an InGaAs HEMT with a 10 GHz bandwidth and a noise figure of 5.5 dB [29]; the final MMIC achieves temperature resolution of approximately 0.5 K. Integrated in the system, temperature resolution of 2 K per frame was achieved at a image refresh rate of 17 Hz.

A frame taken from a video taken indoors of a human subject with a bag of shrapnel beneath a sweatshirt is shown in Figure 1.6. Although TRW Inc. was acquired by Northrop Grumman, the developers of the TRW camera have continued to work on low-noise PHEMT MMIC amplifiers for passive imaging systems, through a related program on millimeter-wave/terahertz focal plane array technology [30].

Figure 1.6: Passive W-band image of an individual wearing a sweatshirt with a plastic bag of metal shrapnel concealed beneath it. Darker shades in this image represent warmer temperatures. Image taken from [31].

The most significant program in the last several years is the Microantenna Arrays: Technology and Applications (MIATA) program [7]. The researchers utilizing the passive direct approach included HRL Laboratories, LLC, and Teledyne Scientific (previously Rockwell Scientific). Initially meant to combine W-band ($f = 95\,\mathrm{GHz}$) and long-wave infrared ($\lambda = (8\text{–}12)\,\mu\mathrm{m}$) focal plane arrays in the same aperture, the requirements were relaxed to focus only on the W-band region, with a phase-two goal of NETD $= 2\,\mathrm{K}$ temperature resolution. National Institute of Standards and Technology (NIST) was employed to verify the performance of the detectors developed in MIATA; the calibration source described in Chapter 3 is a byproduct of that effort.

Last but not least are the imaging systems developed by Appleby et al. [32, 33], which operate at near-video ($\approx 25\,\mathrm{Hz}$) frame refresh rates in the range of $f = 30\,\mathrm{GHz}$ to $f = 95\,\mathrm{GHz}$. The most recent iteration of the receiver design is a three-stage InP LNA chain, utilizing a biased Schottky diode detector. The MMIC package has an integrated horn, and realized temperature resolution is approximately 0.75 K [34]. These systems have been integrated with helicopter landing systems and in security screening at checkpoints.

1.4.4 PASSIVE DIRECT BROADBAND IMAGING

The systems that produce the images in Chapter 6 fall into this category. An example is shown in Figure 1.7. We utilize cryogenic antenna-coupled microbolometers, and as a bolometer is inherently frequency-independent, the bandwidth of the detector is defined by the antenna. In the case of the detectors discussed in this thesis (see Chapter 2), the rf—or imaging—bandwidth is in the range of $f = 100$ GHz to $f = 3.6$ THz. A spiral antenna is the radiation receiving structure, and the microbolometer is suspended at the feedpoint of the antenna. See Chapter 6 for more example images.

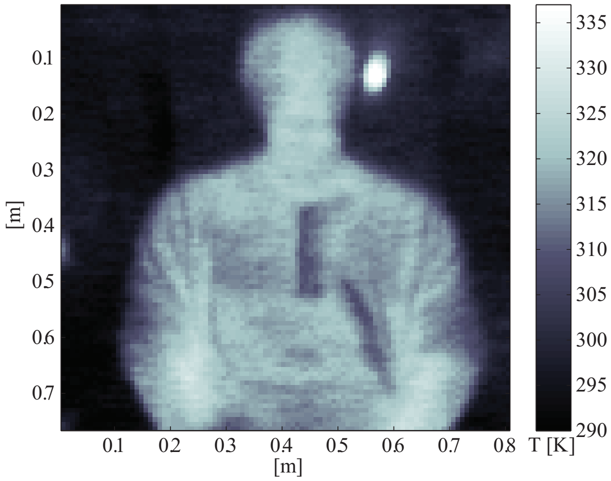

Figure 1.7: Passive broadband millimeter-wave/terahertz image, over the band $f = (100\text{–}1200)$ GHz. The human subject is wearing a long-underwear type of sweater, with the sleeves pushed up. Folds in the clothing are observed, as is the increased radiometric temperature from the unclothed arms. The concealed object on the right is a ceramic (ZrO_2) knife. The circular hot spot in the background is a primitive calibration target—an expanded polystyrene foam cup of hot water.

1.4.5 Terahertz time-domain

No discussion of modalities would be complete without the pioneers and soldiers of the terahertz frequency range, those who brought us—and continue to further—terahertz time-domain spectroscopy (TDS). Because these systems generate frequency content by taking the Fourier transform of ultrafast pulses, they are inherently broadband, and enable reliable measurements from $f = 100\,\mathrm{GHz}$ to $f = 10\,\mathrm{THz}$. It is likely that this category of system will soon provide a tool in the millimeter-wave/terahertz frequency range analogous to the vector network analyzer in the microwave regime. Many material measurement campaigns have been carried out with these systems, including several that are important in this thesis [4, 35].

1.4.6 Photomixing (frequency-domain)

Similar to the end user as a terahertz TDS are systems from companies such as EMCORE, who utilize photomixing [36] to produce a very broadband ($f = 20\,\mathrm{GHz}$ to approximately $f = 2\,\mathrm{THz}$), high resolution ($\Delta f = 250\,\mathrm{MHz}$) source [37]. It is also likely that, similar to TDS, a system utilizing photomixing will enable an instrument similar to a network analyzer.

1.5 Organization of this thesis

This thesis is divided into chapters as follows:

- In Chapter 2, antenna-coupled bolometric detectors are examined at both room and cryogenic temperatures. Their electrical properties are measured, compared with theory, and discussed. Antenna patterns are also measured at several frequencies in the bandwidth range of interest. These measurements, as well as those required for another program [7], led to the development of the calibration source described in the following chapter.

- In Chapter 3, an aqueous blackbody calibration source for the millimeter-wave/terahertz frequency range is described in detail. This source is an entirely new design, utilizing water as the blackbody, and an "optical trap" geometry to increase the emissivity at the aperture.

- In Chapter 4, an examination of the transmission and scattering properties of expanded

Table 1.2: SI base quantities, base units names, and base unit symbols.

	SI base unit	
base quantity	name	symbol
length	meter	m
mass	kilogram	kg
time	second	s
electric current	ampere	A
thermodynamic temperature	kelvin	K
amount of substance	mole	mol
luminous intensity	candela	cd

polystyrene (EPS) foam is completed. This work relates to that in Chapter 3, in that the calibration source is manufactured from EPS foam, and its electromagnetic properties affect the performance of the source above $f = 450\,\mathrm{GHz}$.

- Chapter 5 provides a detailed discussion of the imaging systems and the images acquired with them. A quasi-optical linear-to-circular polarization converter at $f = 95\,\mathrm{GHz}$ (also known as a $\lambda/4$ plate in optics) is discussed due to its use in an active imaging system for concealed weapons detection. Additionally, some previous work in discrete lens arrays that is not directly applicable to the terahertz frequency regime, but still falls in the quasi-optical category, is considered.
- Finally, Chapter 6 describes the imaging systems, and provides descriptive phenomenology of the resulting images, resulting in a recommendation for a minimum temperature resolution for passive millimeter-wave/terahertz imaging indoors.

1.6 A NOTE ON UNITS

The SI system of units is followed throughout this thesis. Table 1.2 lists the seven SI base quantities and their names, the so-called “SI base units.” Noted is that the kelvin and its symbol (K) are additionally used to denote the value of a temperature difference. The candela is not used in this thesis as it is considered a photometric rather than radiometric quantity, but it is included in the base unit table for completeness.

SI *derived units* are expressed in terms of base units or other derived units, including the

Table 1.3: SI derived units in terms of base units

	SI derived unit	
derived quantity	name	symbol
area	square meter	m^2
volume	cubic meter	m^3
speed, velocity	meter per second	$m\ s^{-1}$
acceleration	meter per second squared	$m\ s^{-2}$
wave number	reciprocal meter	m^{-1}
mass density (density)	kilogram per cubic meter	$kg\ m^{-3}$
specific volume	cubic meter per kilogram	$m^3\ kg^{-1}$
current density	ampere per square meter	$A\ m^{-2}$
magnetic field strength	ampere per meter	$A\ m^{-1}$
luminance	candela per square meter	$cd\ m^{-2}$

supplementary units (radian and steradian). Derived units are obtained by multiplication and division. The SI derived units used in this thesis, in terms of base units, are listed in Table 1.3.

Some derived SI units have special names and symbols; these are listed in Table 1.4. Included are the supplementary units, the radian and steradian. Additionally, the first radiometric quantity encountered thus far is defined in Table 1.4—radiant flux.

Finally, SI derived units that can be expressed in terms of other SI derived units having special names and symbols, including the radian and steradian, are listed in Table 1.5. This may be the most relevant listing of derived units, as it includes the radiometric quantities which are frequently used throughout this thesis, including irradiance, radiant intensity, and radiance. Although a common term in the microwave community for irradiance is “power density,” the SI naming convention will be followed in this thesis.

One additional unit which is not included in the SI base or derived units is the *bel*, designated “B.” A tenth of a bel, a decibel, or 1 dB, is the unit used to refer to relative power or voltage levels. Referenced to absolutes such as the volt or milliwatt, a suffix is added in agreement with the common parlance, in this case, dBV and dBm respectively.

1.7 A NOTE ON TERMINOLOGY

Besides the emphasis on correct SI units, several specifics regarding common terminology throughout this thesis should be set forth.

Table 1.4: SI derived units with special names and symbols

	SI derived unit			
derived quantity	name	symbol	compound form	base unit form
plane angle	radian	rad	—	m $\mathrm{m}^{-1} = 1$
solid angle	steradian	sr	—	$\mathrm{m}^2\ \mathrm{m}^{-2} = 1$
frequency	hertz	Hz	—	s^{-1}
force	newton	N	—	m kg s^{-2}
pressure, stress	pascal	Pa	$\mathrm{N/m}^2$	m^{-1} kg s^2
energy, work, heat	joule	J	N m	m^2 kg s^{-2}
power, *radiant flux*	watt	W	J/s	m^2 kg s^{-1}
electric charge	coulomb	C		A s
electric potential	volt	V	W/A	m^2 kg s^{-3} A^{-1}
capacitance	farad	F	C/V	m^{-2} kg^{-1} s^4 A^2
resistance	ohm	Ω	V/A	m^2 kg s^{-3} A^{-2}
conductance	siemens	S	A/V	m^{-2} kg^{-1} s^3 A^2
magnetic flux	weber	Wb	V s	m^2 kg s^{-2} A^{-1}
magnetic flux density	tesla	T	$\mathrm{Wb/m}^2$	kg s^{-2} A^{-1}
inductance	henry	H	Wb/A	m^2 kg s^{-2} A^{-2}

Table 1.5: SI derived units expressed in terms of SI derived units having special names and symbols

	SI derived unit		
derived quantity	name	symbol	base unit form
angular velocity	radian per second	rad/s	m m^{-1} $\mathrm{s}^{-1} = \mathrm{s}^{-1}$
angular acceleration	radian per second squared	$\mathrm{rad/s}^2$	m m^{-1} $\mathrm{s}^{-2} = \mathrm{s}^{-2}$
irradiance	watt per square meter	$\mathrm{W/m}^2$	kg s^{-3}
radiant intensity	watt per steradian	W/sr	m^2 kg s^{-3} sr^{-1}
radiance	watt per square meter steradian	$\mathrm{W/(m^2\ sr)}$	kg s^{-3} sr^{-1}

- The imaginary unit $\sqrt{-1}$ is denoted $\jmath$ throughout this thesis, and is not intended to be defined as $\jmath = -\imath$ as is done in some texts, but simply a convention to follow in these pages.

- At microwave frequencies, we use $\hat{\epsilon} = \epsilon' - \jmath\epsilon''$ to refer to the dielectric constant of a material, and $\hat{n} = n - \jmath k$ to denote the refractive index of a material. The relationships between $\hat{\epsilon}$ and $\hat{n}$ are:

  $$\epsilon' = n^2 - k^2 \tag{1.6}$$

  and

  $$\epsilon'' = 2nk, \tag{1.7}$$

  or conversely,

  $$n = \left(\frac{\sqrt{\epsilon'^2 + \epsilon''^2} + \epsilon'}{2} \right)^{1/2} \tag{1.8}$$

  and

  $$k = \left(\frac{\sqrt{\epsilon'^2 + \epsilon''^2} - \epsilon'}{2} \right)^{1/2}. \tag{1.9}$$

  Because of the use of quasi-optical techniques in this thesis, as well as the fact that radiometry (and therefore radiometric temperature) is a significant subject of this thesis, ϵ will denote the emissivity of an object or system of objects. The complex refractive index will be used in place of the complex dielectric constant when discussing dielectric material parameters.

- Finally, the frequency range from approximately W-band to several terahertz is termed the “millimeter-wave/terahertz” frequency range (refer to Figure 1.1), because it encompasses parts of both of these (i.e., millimeter-wave and terahertz) frequency ranges. In the past, the millimeter-wave band ranging from $f = 30\,\text{GHz}$ to $f = 300\,\text{GHz}$ and the sub-millimeter-wave band ranging from $f = 300\,\text{GHz}$ to $f = 3\,\text{THz}$ encompassed the frequency range where most research was performed. Recently, however, the “terahertz” band has broadly overlapped the sub-millimeter-wave band, and continues up to $f = 10\,\text{THz}$ (followed by far-infrared, near-infrared, mid-infrared, etc.). The usage of “millimeter-wave/terahertz” to describe this broad frequency regime is now accepted and preferred [38].

CHAPTER 2

ANTENNA-COUPLED MICROBOLOMETERS

> *You can know the name of a bird in all the languages of the world, but when you're finished, you'll know absolutely nothing whatever about the bird... So let's look at the bird and see what it's doing — that's what counts.*
>
> —Richard Phillips Feynman

CONTENTS

2.1 INTRODUCTION

Detection of electromagnetic radiation from radio frequencies to gamma-rays is performed, at the highest level, by two distinct types of sensors: Coherent (phase-preserving) and incoherent (direct). Coherent detectors multiply the incident electric field with the electric field from a local oscillator, which results in a beat (intermediate) frequency that carries the phase and amplitude information of the incident field, as long as the local oscillator is stable. Incoherent detectors are categorized into thermal detectors and photon detectors. Thermal detectors absorb incident electromagnetic radiation and convert it to heat, causing both a temperature change in the absorbing element and a corresponding change in some, usually electrical, measurable property of the detector. Photon detectors respond directly to absorbed photons. An absorbed photon frees bound charge carriers that produce one or more of several measurable effects, such as changes in the chemical or electrical properties of the detector material.

The antenna-coupled microbolometers that this chapter discusses are a subset of bolometers, which, in turn, are members of the class of thermal detectors. Thermal detectors can measure either energy, usually denoted E, or power, usually denoted P. A subtle distinction is made between these two detection concepts; the thermal detectors that measure energy are called *calorimeters*, from the Latin *calor*, meaning *heat*. In them, single photons are detected—one by one—as individual quanta of absorbed energy. The time constant of the calorimeter is shorter than the arrival period between photons; this is the standard mode of operation at x-ray wavelengths.

Bolometers, on the other hand, measure an incident *flux* of photons. The Greek *bole* means *ray*, so a bolometer is a "ray-meter" that measures power in units of [J/s]. The time constant of the bolometer is then, by definition, greater than the arrival period between photons. This is the *modus operandi* in the millimeter-wave/terahertz frequency regime. Bolometers are also in the category of square-law detectors, meaning that their output voltage or current is proportional to the square of the detected signal amplitude, i.e., signal power.

The term "bolometer," with no other qualifications, defines an absorber with an attached thermometer, both of which are thermally isolated from a heat sink by an intentionally created thermal link G. This generic bolometer is depicted in Figure 2.1. It has several fundamental parameters—its heat capacity C and its thermal time constant $\tau_0 = C/G$, where G is the thermal conductance between the absorber and the heat bath at temperature T_0. The average bolometer temperature is denoted T. Because of the thermal isolation between the absorber and the heat sink, power absorbed by the bolometer causes a temperature rise in the heat capacity C at T of $\Delta T = P/G$ at the rate of $dT/dt = P/C$, which has the limiting value $T = T_0 + P/G$. The temperature rise is measured by a thermometer, of which the sensing element is thermally linked with the absorbing element of the bolometer. The thermometer can be any of several types, including a temperature-dependent resistance, capacitance [39, 40], or inductance [41, 42]. In this chapter we restrict our focus to temperature-dependent resistance. Bolometers can be classified as either "simple" or "composite." The difference is that in the composite case, the absorber and thermometer are physically distinct elements, though still well-coupled thermally. Examples of these are discussed extensively in [43]. In the simple case, which is the class that this chapter describes, the absorber and thermometer element are physically the same.

Area-absorber bolometers are commonly used at infrared frequencies, though they are generally outperformed by semiconductor photon detectors such as HgCdTe at wavelengths shorter than $\lambda \approx 10\,\mu\text{m}$. Photoconductive photon detectors cannot operate at waevlengths longer than $\lambda \approx 200\,\mu\text{m}$, so thermal detectors are really the only option below $f = 1.5\,\text{THz}$. At millimeter-wave and terahertz frequencies, the size of the absorbing element becomes quite large and therefore

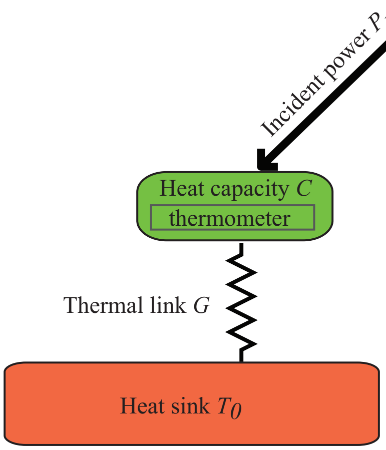

Figure 2.1: Simplified generic bolometer. Incident power causes a temperature rise in the absorber with heat capacity C. Heat exits via the thermal link G to the heat sink at temperature T_0, at a rate of $G(T - T_0)$.

slow. By reducing the size of the bolometer and putting it at the feedpoint of an antenna, the "antenna-coupled microbolometer" is achieved. This technique extends the frequency range of these thermal detectors into the microwave and millimeter-wave regime, and results in a very effective direct detector. At the high end of the millimeter-wave/terahertz frequency range, antennas have been coupled to microbolometers at frequencies as high as $f = 31.6\,\mathrm{THz}$ [44].

Antennas at millimeter-wave and terahertz frequencies can be integrated with microbolometers using standard photolithographic techniques. Simple resistive microbolometers, either freestanding or substrate-supported, were some of the first detectors to be integrated with these antennas. In those early days, bismuth—a semimetal—was the most commonly used room-temperature bolometer material [45] because it was understood that for practical microbolometer dimensions, metals would provide too low a resistance to efficiently match to typical $R \approx 100\,\Omega$ antenna impedances, while semiconductors would provide too high an impedance. At that time, with film thicknesses less than 100 nm difficult to achieve, this was indeed a reasonable conclusion, but as thin-film fabrication techniques improved it became straightforward to make much thinner films with good control and reproducibility. Thus, antenna-coupled microbolometers (ACMB) made from thin (20 nm or less) Nb were demonstrated [46, 47], and many other uncooled bolometer materials have also been explored [43] in pursuit of infrared focal plane arrays.

One of the original motivations for the use of Nb, versus other high-resistivity metals, was its compatibility with superconducting devices. Nb deposition and patterning techniques, as well as understanding of its properties in thin-film form, were developed quite early because of interest in superconducting devices, particularly tunnel junctions [48]. Thus, the same freestanding microbolometer bridge used at room-temperature has also been investigated in superconducting mode [49, 50]. In the cryogenic case, its operation is quite different than at room temperature, because the internal temperature gradients within the bridge are large compared to the width of the superconducting transition; at room-temperature, the internal temperature gradients are much smaller than the temperature scale over which the resistance changes significantly. These temperature gradients are in both cases created by the dissipation of Joule heat in the bridge from the applied bias. In the superconducting case, the Joule heat creates a "hotspot" at the center of the bridge, where the temperature lies above the superconducting transition temperature T_c of the film. This hotspot generates all the dc voltage appearing across the bridge. The theory of detection and mixing in superconducting hotspots has been developed and experimentally verified within the last decade [51, 52], though it was preceded by early work in superconducting wires [53].

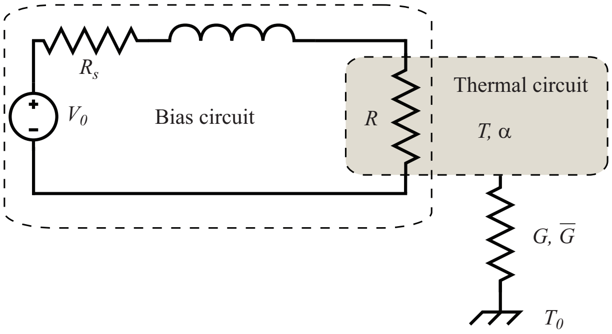

Figure 2.2: Schematic of overlapping bias and thermal circuits, which interact at the bolometer. The resistor R denotes the bolometer, and the source impedance is $Z_s(\omega) = R_s + \jmath\omega L$.

NbN is another material whose development in thin film form was largely stimulated by interest in superconducting devices. It has a somewhat higher transition temperature (T_c) than pure Nb, though in both cases T_c depends strongly on film thickness as well as internal film stress and other properties controlled by deposition conditions. In its normal state, NbN is a "granular metal" [54] meaning that electronic conduction can be described by grains, each consisting of a standard Drude metal (i.e., conductivity follows $\sigma(\omega) = \sigma_0/(1 + \jmath\omega\tau)$, where $\omega = 2\pi f$ and τ is the mean free time of a charge carrier) separated by inter-granular tunneling barriers. The typical grain size can be longer or shorter than the Drude mean free path, depending on deposition conditions; on a macroscopic scale, NbN films have resistivities that are considerably higher than pure Nb, and have temperature coefficients of resistance (TCR) that can either be positive or negative depending on deposition conditions, similar to semimetals.

The higher resistivity of NbN motivates its investigation as an alternative to Nb for antenna-coupled microbolometers. If the normal-state resistance of the bolometer is held fixed to match a specific antenna impedance, the difference in material resistivities requires that the NbN bridge will be thicker and/or shorter than its Nb counterpart. This in turn implies a higher T_c and/or a lower inductance, respectively. Inductance contributes to an impedance mismatch between the antenna and bolometer, and adds a frequency dependence to the otherwise broadband antenna and frequency-independent microbolometer impedances. This inductance can cause a significant impedance mismatch loss between the microbolometer and the antenna at high frequencies, where it becomes large.

2.1.1 CALCULATION OF RESPONSIVITY

Jones [55], Mather [56, 57], and Richards [58] have each presented the theory of bolometer performance, and can be referenced for a more rigorous treatment than is provided here. This subsection contains only the directly applicable results from those articles; the goal in this subsection is to derive responsivity from the basic thermodynamic and electric principles that govern the behavior of a bolometer. The heat flow equation for a bolometer is given by

$$P_{rf}e^{\jmath\omega t} + P_b + \frac{dP_b}{dT}\Delta T = \overline{G}(T - T_0) + G\Delta T + C\frac{d\left(\Delta T e^{\jmath\omega t}\right)}{dt}, \tag{2.1}$$

where P_b is the power deposited by the bias circuitry (and any other constant power being deposited in the absorber), $\overline{G}$ is the average thermal conductance, $G = dP/dT$ is the dynamic thermal conductance, and ΔT represents the temperature change due to $P_{rf}e^{\jmath\omega t}$. Equating the steady-state terms not associated with P_{rf} in (2.1) produces $P_b = \overline{G}(T - T_0)$, and thus the average bolometer temperature is found:

$$T = \frac{P_b}{\overline{G}} + T_0. \tag{2.2}$$

In the case of a plain wire as a bolometer (the situation in this chapter) when the thermal conductivity of the material is approximately constant with temperature, the average thermal conductance $\overline{G}$ is given by

$$\overline{G} = 12\kappa\frac{A}{l} \quad \text{[W/K]}, \tag{2.3}$$

where A, l, and κ are the cross-sectional area, length, and thermal conductivity of the bridge, respectively [59]. On the other hand, if κ is a strong function of T and there are thermal gradients in the wire, the thermal conductance is [58]

$$\overline{G} = \frac{A/l}{T_0 - T}\int_{T}^{T_0} \kappa(T)dT \quad \text{[W/K]}. \tag{2.4}$$

Equating the terms in (2.1) that are associated with the signal $P_{rf}e^{\jmath\omega t}$ produces

$$P_{rf}e^{\jmath\omega t} = G\Delta T + C\frac{d\left(\Delta T e^{\jmath\omega t}\right)}{dt} - \frac{dP_b}{dT}\Delta T, \tag{2.5}$$

and then isolating the temperature variation,

$$\Delta T = \frac{P_{rf}}{G + \jmath\omega C - dP_b/dT}. \tag{2.6}$$

The third term in (2.1) and the last term in (2.5) are due to electrothermal feedback (ETF). ETF is a concise means of saying that the bias power to keep a device at a selected bias point is dependent on the resistance of the device, which is dependent on the incident rf power. An example clarifies: if the rf power incident on the bolometer increases, the temperature of the bolometer increases; in materials with a positive TCR the resistance of the bolometer increases, and in the case of a constant voltage bias, the current through the bolometer decreases. Ideally, ETF keeps the bolometer operating point constant. In this case (negative ETF), this effect of keeping the operating point constant is realized by reducing the bias power when the rf power increases, which reduces the temperature rise. In general, the electrothermal term— last in the denominator of (2.6)—can be written as

$$\frac{dP_b}{dT} = \frac{dP_b}{dR}\frac{dR}{dT} = -\Lambda\frac{P_b\alpha}{T}, \tag{2.7}$$

where $\alpha = (T/R)(dR/dT)$ and $\Lambda = (R - Z_S)/(R + Z_S)$ takes into account the bias circuit on the ETF [50]; R is the resistance of the bolometer and Z_S is the impedance of the bias circuit. $\Lambda = 1$ defines a perfect voltage bias ($Z_S \ll R$) and negative ETF, while $\Lambda = -1$ defines a perfect current bias ($Z_S \gg R$) and positive ETF. The loop gain of the ETF path can be written as

$$\mathcal{L}(\omega) = \frac{\alpha P_b}{GT}\frac{\Lambda(\omega)}{\sqrt{1 + \omega^2\tau_0^2}}. \tag{2.8}$$

One of the effects of ETF is a reduction of the time constant from τ_0 to $\tau_{eff} = \tau_0/\left(1 + \mathcal{L}_0\right)$, where $\mathcal{L}_0$ is the low-frequency loop gain $P_b\alpha/(GT)$. The limit for uncooled bolometers, in the current-biased case, is

$$\frac{\alpha P_b}{GT} = \frac{P_b}{R}\left(\frac{1}{G}\frac{dR}{dT}\right) = \frac{P_b}{R}\beta, \tag{2.9}$$

where β is known as the "specific responsivity."

The responsivity of a simple bolometer is defined as either the variation in voltage (for a current-biased bolometer) or current (for a voltage-biased bolometer) per watt of absorbed signal power. For a voltage-biased bolometer the current responsivity is

$$S_I \equiv \frac{dI}{dP_{rf}} = \frac{dI}{dR}\frac{dR}{dT}\frac{dT}{dP_{rf}}. \tag{2.10}$$

To voltage bias a bolometer, a constant current I is driven through the parallel combination of the bolometer R and a shunt resistor R_S. If $R_S \ll R$ the bolometer is voltage biased. The voltage across and current through the bolometer allow a calculation of $dI/dR = -I\left(\Lambda+1\right)/(2R)$, and dR/dT is simply $\alpha R/T$. Finally,

$$\frac{dT}{dP_{rf}} = \frac{1}{G}\frac{1}{1+\jmath\omega\tau_0+\mathcal{L}_0\Lambda}, \tag{2.11}$$

ultimately giving the current responsivity as

$$S_I \equiv \frac{dI}{dP_{rf}} = -\frac{1}{2V}\frac{(1+\Lambda)\mathcal{L}_0}{1+\Lambda\mathcal{L}_0} \quad [\mathrm{A/W}], \tag{2.12}$$

where for a perfect voltage bias ($\Lambda = 1$) and high loop gain, $S_I = -1/V$. For $\Lambda\mathcal{L}_0 = 1$, which is the situation that provides the maximum SNR with our chosen electronics [60], $S_I = -1/2V$.

To achieve a current bias in reality, the resistor R_S is placed in series with the bolometer. For the current biased case,

$$S_V \equiv \frac{dV}{dP_{rf}} = \frac{1}{2I}\frac{(1-\Lambda)\mathcal{L}_0}{1+\Lambda\mathcal{L}_0} \quad [\mathrm{V/W}]. \tag{2.13}$$

In the limit of a perfect current bias ($\Lambda = -1$) and high loop gain, $S_V = -1/I$; this is the case for superconducting devices. On the other hand, uncooled bolometers are in the limit of low loop gain, since $R \propto T$ at room temperature giving $\alpha \approx 1$, and a δT of approximately 30 K is expected for a typical biased device.

2.1.2 BOLOMETER NOISE

Noise in bolometers arises from several sources—the Johnson noise due to their nonzero resistance, the phonon noise inherent in the thermal conductance G, and noise in the photon flux; additional contributions that are not intrinsic to the bolometer itself are sometimes included, such as amplifier noise. Noise-equivalent power, or NEP, is the most common figure of merit used to describe detector sensitivity. It is defined as the signal power that produces an rms SNR of unity in a system with a 1 Hz bandpass, and is given in units of $[\mathrm{W{\cdot}Hz^{-1/2}}]$. NEP is related to the signal-to-noise ratio by

$$\mathrm{NEP} = \frac{P_{rf}\sqrt{\tau_{int}}}{\mathrm{SNR}}, \tag{2.14}$$

where τ_{int} is the post-detection integration time and P_{rf} is the absorbed signal power. Often P_{rf} is defined as the incident signal power, and an efficiency factor η is then included to describe the overall coupling and detection efficiency, which includes filter and window transmission, lens interface reflections, polarization mismatch loss, and antenna-bolometer mismatch loss. The NEP can also be expressed in terms of, for example, current responsivity and current noise:

$$\mathrm{NEP} = \frac{i_n}{S_I}. \tag{2.15}$$

Ideally, the limiting factor in any detection system is the noise in the photon flux itself, but more often, noise contributions by the detector, amplification, and readout circuitry dominate. The total NEP is the quadrature sum of the individual contributions because they are uncorrelated noise sources, and is given by

$$\mathrm{NEP}_{tot} = \sqrt{\mathrm{NEP}_t^2 + \mathrm{NEP}_j^2 + \mathrm{NEP}_p^2 + \mathrm{NEP}_r^2}, \tag{2.16}$$

where NEP_t represents the noise contribution from the thermal conductance G (also called phonon noise or thermal fluctuation noise), NEP_j denotes the contribution to the total NEP from the Johnson noise, and the readout electronics contribution is denoted NEP_r. The thermal fluctuation noise originates from electrons or phonons passing through the material that comprises the conductance G. This fluctuation in G directly affects the current or voltage noise at the detector output. It is given by [56]

$$\mathrm{NEP}_t = \sqrt{4k_B T^2 G \Xi}, \tag{2.17}$$

where Ξ accounts for the temperature gradient in the bolometer. For room-temperature metals, $\Xi \approx 0.75$, and for superconductors, $\Xi \approx 0.67$ [56]. The Johnson noise contribution, referenced to current, is given by

$$\mathrm{NEP}_j = \sqrt{4k_B T/R}, \tag{2.18}$$

where R is the bolometer resistance. Including the results of ETF, the term $(1+\Lambda)/[2\,(1+\mathcal{L})]$ should be multiplied with NEP_j in order to provide the resulting Johnson noise at the readout. Electrothermal gain does not amplify Johnson noise, a fact which is exploited in the electronics readout scheme we have chosen [60]. The ultimate noise source to be limited by is that arising from statistical fluctuations in the incident photon stream. For antenna-coupled (single-mode) detectors, this is given by

$$\mathrm{NEP}_p = k_B T\sqrt{2\Delta f}, \tag{2.19}$$

where Δf is the detection bandwidth defined in the case of this chapter by the antenna. It has been shown that the antenna-coupled microbolometers described in this chapter are approaching this limit [61], when operated in the superconducting mode with appropriate electronics. The contribution from the readout electronics, NEP_r, varies from system to system, and will not be discussed here. A treatment of the electronics utilized by the systems that acquire images such as those in Chapter 6 is provided in [60].

The electrical NEP, that is, NEP derived from the noise spectral density and the responsivity calculated from the I–V curve is approximately $25\,\mathrm{fW}\cdot\mathrm{Hz}^{-1/2}$ for the devices in this thesis [49]. However, similar devices have shown even lower values $\mathrm{NEP} = 14\,\mathrm{fW}\cdot\mathrm{Hz}^{-1/2}$ [21]. The rf NEP, that is, NEP derived from response to a known incident power, is below $100\,\mathrm{fW}\cdot\mathrm{Hz}^{-1/2}$; exact values are difficult to estimate due to the various losses (attenuation by the windows/filters and antenna mismatch loss).

2.1.3 Figures of merit

In this chapter, several variants of antenna-coupled microbolometers are examined, where the bridge geometries and microbolometer materials are the varying parameters. The important figures of merit that are compiled from the measurements later in this chapter are explained briefly here. In the room-temperature case, the chief parameters governing the operation of an antenna-coupled microbolometer, and characterizing its sensitivity, are the specific responsivity

$$\beta = \frac{1}{G}\frac{dR}{dT} \quad [\mathrm{V} \cdot \mathrm{W}^{-1} \cdot \mathrm{mA}^{-1}], \tag{2.20}$$

and the zero-bias resistance, R_0. The zero-bias resistance is exactly what it declares to be, that is, the fit parameter of device resistance when no current is passing through it. Thermal runaway in a bolometer occurs when the thermal conductance, G, is not great enough to allow the heat in the bridge to flow to the heat bath; the bridge temperature continues to rise until the bridge material is destroyed from thermal effects. This occurs in the room-temperature current-biased Nb devices, for example, when $\beta I_{\mathrm{b}}^2 = 1$, which is made clear by Equation (2.22). At room temperature, this is mitigated by careful selection of the bias current, based on the thermal conductance of the bridge. In the superconducting modality, negative ETF is utilized in order to ensure a stable operating point, as discussed in the previous sections.

In the superconducting case, the normal-state resistance R_n, and the saturation power

$$P_{sat} = G\,(T_c - T_0) \quad [\mathrm{W}] \tag{2.21}$$

are the extracted parameters of importance; G is the thermal conductance between the bolometer and the heat bath (the substrate). P_{sat} is the maximum amount of power that can be deposited on the bridge, either by dc bias, incident rf, or a combination of the two, before the entire bridge temperature exceeds the superconducting transition temperature T_c. At this point, the resistance variations due to incident rf become immeasurable, and the detector is saturated.

2.2 Materials and geometries

2.2.1 Nb ACMB

The Nb detectors have been described in prior publications [21, 62]. In short, a $20\,\mathrm{nm} \times 1\,\mu\mathrm{m} \times l\,\mu\mathrm{m}$ Nb bridge is suspended at the feed point of a spiral antenna. The length of the bridge, l, determines the high-frequency cutoff, f_c, of the spiral antenna, and for Nb bridges in this chapter it is either 12 µm or 24 µm, corresponding to $f_c = 3.6$ THz or 1.8 THz, respectively. The Si substrate beneath the bridge is removed with an isotropic XeF_2 etch, leaving the Nb bridge free-standing (though surrounded by a small amount of SiO_2). The thermal conductivity of the bridge to the heat bath, G, consists of two additive components: that due to the Nb bolometer itself and that due to thermal conduction through the SiO_2 that encapsulates the Nb. A rendering of the cross section is seen in Figure 2.3. The depth of the XeF_2 etch varies between 4 µm and 8 µm from chip to chip. Because the etch windows in the SiO_2 are separated by 4 µm total (2 µm on either side of the centerline of the Nb bridge), the minimum etch depth in order to fully "release" the Nb bridge from the Si substrate is 2 µm. Etch depths greater than 2 µm ensure that the bridge is free-standing, but also remove Si from beneath the inner-most radiating section of the antenna. An optical micrograph of a typical Nb detector is shown in Figure 2.4, and an scanning electron micrograph of a Nb detector is shown in Figure 2.5.

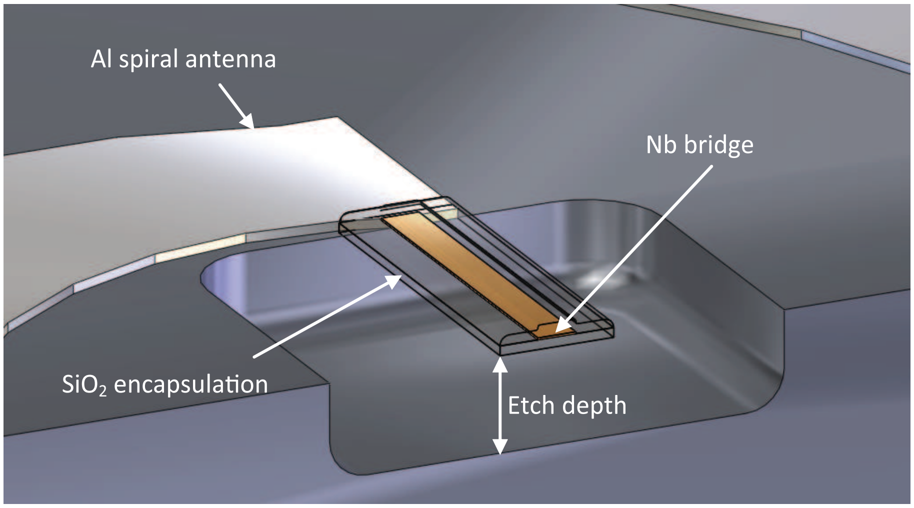

Figure 2.3: Cross-section rendering of an Nb bridge encapsulated in SiO_2, suspended above Si at the feed-point of a circular spiral antenna. Rendering is simplified and not to scale. In actuality, the Si floor of the etch pit is rough, and the sidewalls of the pit are concave.

2.2.2 NbN ACMB

To compensate for the higher resistivity of NbN and present an impedance similar to the Nb bridges at the antenna feed point, the NbN bridge aspect ratio is changed, increasing both width ($w = 2$ µm) and thickness ($t = 250$ nm). Length l defines antenna bandwidth, and is either

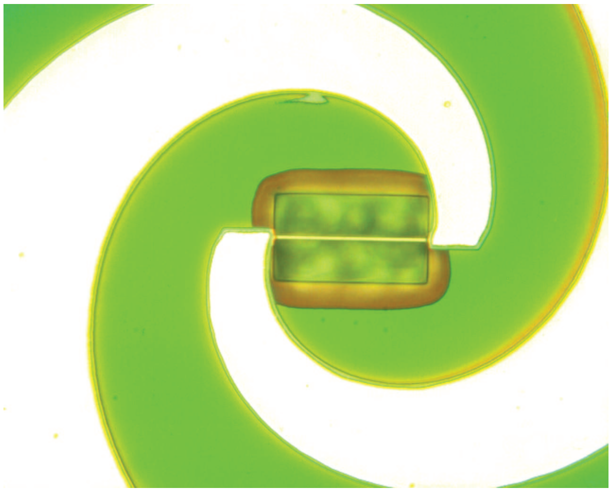

Figure 2.4: Optical micrograph of Nb antenna-coupled microbolometer.

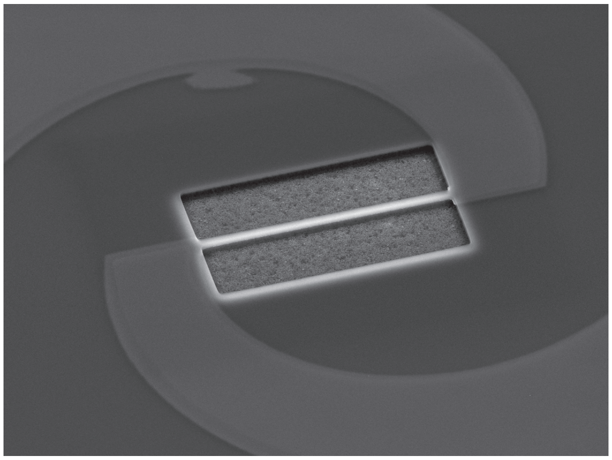

Figure 2.5: Scanning electron micrograph of Nb antenna-coupled microbolometer.

$l = 8\,\mu\text{m}$ (corresponding to $f_c = 5.4\,\text{THz}$) or $l = 19\,\mu\text{m}$. The NbN bridges lie atop SiO_2, but have no SiO_2 on top of them. The Si etch is anisotropic, that is, partially directional, and shown in the scanning electron micrograph of Figure 2.6. SEM images of the etched devices show that the etch pit size reduces from the initial etch window size, as depth increases. This anisotropy decreases the under-etch of the inner-most portion of the antenna, but leaves a vertical Si "fin" standing collinear beneath the NbN bridge, approximately half the height of the total etch depth.

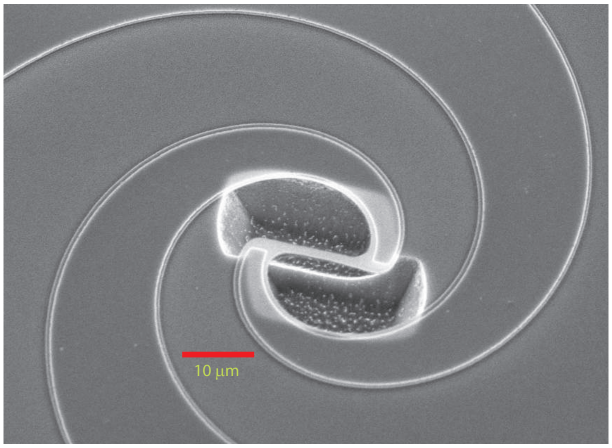

Figure 2.6: Scanning electron micrograph of NbN antenna-coupled microbolometer.

2.3 TEST CONFIGURATIONS

Shown in Figure 2.7 is a diagram of the chip, substrate lens, and antenna, depicting the important geometry and associated dimensions. The spiral antenna is 380 µm in diameter, and located at the center of the chip, directly below the apex of the lens. The bolometer axis is collinear with the bias traces extending from the arms of the antenna. It is assumed that the dc bias traces will affect the low-frequency antenna response, producing a modified loaded dipole pattern. The parameter focused on in prior work [63] is the dimensionless extension length of the lens, which we parameterize by the quantity $n(h+t)/R$. For an aplanatic design, this is unity. For the optimum efficiency elliptical design described in [63], this is larger, typically 1.3–1.6 depending on design frequency. Our configuration corresponds to $n(h+t)/R = 1.41$. A metallic mount in the form of a slotted ring captures the substrate lens at its outer diameter, similar to the configuration described in [63]. The ring geometrically vignettes the incident radiation at an angle of 48° from broadside. The drawing in Figure 2.7 is to scale, but additional traces and devices are not included for clarity; they are positioned in the upper right-hand $(1,1)$ and lower left-hand $(-1,-1)$ corners, in actuality. The central device shown is $(0,0)$. A photograph of the assembled module is shown in Figure 2.8.

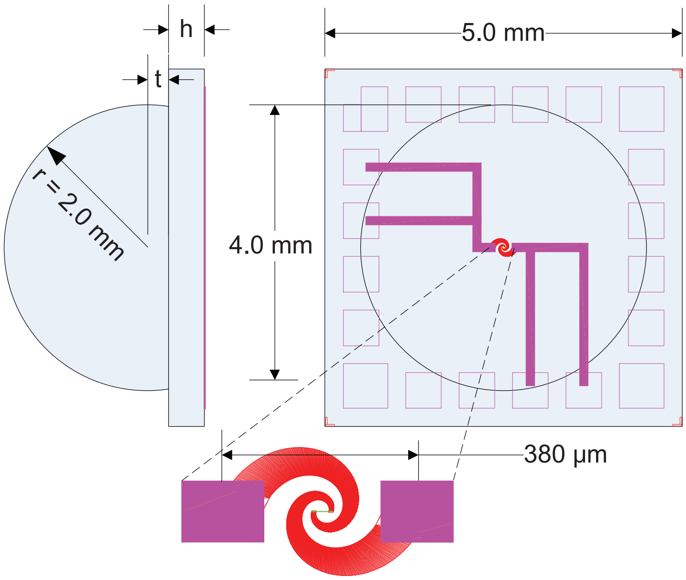

Figure 2.7: Top-view (right) and 90° rotated view (left) of the 5 mm chip, the hyper-hemispherical lens, and an accurate layout of the pertinent traces on the chip. The extension length of the hyper-hemisphere is $t = 0.3\,\mathrm{mm}$ and the thickness of the Si substrate is $h = 0.5\,\mathrm{mm}$. In this chapter, co- and cross-polarized measurements are defined as those in which the incident linearly-polarized field is parallel with and perpendicular to the bolometer axis (and dc bias traces), respectively.

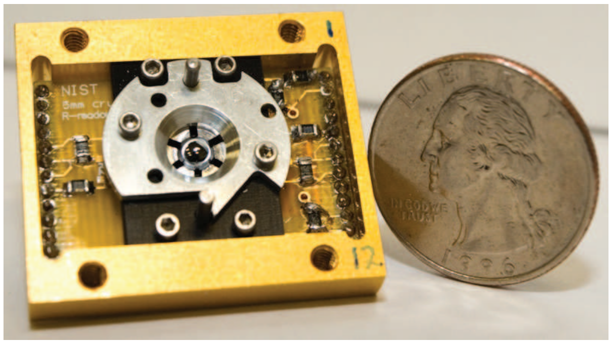

Figure 2.8: Photograph of an assembled 5 mm chip mount, as used in the tests in both this chapter and Chapter 4.

2.3.1 ROOM-TEMPERATURE ELECTRICAL AND RADIATION MEASUREMENTS

At room temperature, device I–V curves are measured using a simple current-bias circuit. Bias currents are on the order of several hundred microamps. Device failure occurs above 1 mA, i.e., for current densities $J > 5 \times 10^6\,\mathrm{A \cdot cm^{-2}}$. NbN devices fail at approximately a factor of two greater current than Nb devices, but because of the larger cross-section of the NbN bridges this corresponds to a lower current density, $J > 5 \times 10^5\,\mathrm{A \cdot cm^{-2}}$. I–V curves are measured and the data fit to

$$V = I\left(R_0 + \beta I V\right) = \frac{I R_0}{\left(1 - \beta I^2\right)}, \tag{2.22}$$

where R_0 is the zero-bias resistance of the bridge and β is its normalized electrical responsivity [46, 22]. Antenna patterns are measured with an azimuth-elevation stage and a backward-wave oscillator (BWO) at $f \approx 650\,\mathrm{GHz}$. The beam is mechanically chopped at the BWO horn aperture at frequencies between $f = 30\,\mathrm{Hz}$ and $f = 400\,\mathrm{Hz}$, and the detector response is monitored with a lock-in amplifier. Additionally, antenna patterns are also measured at $f = 95\,\mathrm{GHz}$ and $f = 238\,\mathrm{GHz}$. At the former frequency, an HP 83624B synthesized sweeper is used to drive an HP 83558A millimeter-wave source module. The source is amplitude-modulated at $f = 1.1\,\mathrm{kHz}$, and the bolometer bias current is set to $I_{\mathrm{bias}} = 200\,\mu\mathrm{A}$. For these measurements, the bolometer axis is fixed in the elevation scan direction, and the incident electric field polarization is co-polarized, cross-polarized, and circularly-polarized in both senses. At $f = 238\,\mathrm{GHz}$, a Gunn diode oscillator [64] is followed by a commercial frequency doubler. The beam is mechanically chopped at $80\,\mathrm{Hz}$ and the electric field is linearly polarized; the bolometer is rotated by 90° to measure both linear polarization senses. The irradiance at the plane of the detector from the linearly polarized transmit horn is on the order of $40\,\mu\mathrm{W{\cdot}mm^{-2}}$. The bolometer bias current is set at $I_{\mathrm{bias}} = 550\,\mu\mathrm{A}$, and the dynamic range of the measurement is 25 dB due to the greater source power. The FWHM beamwidths are increased by a factor of ≈ 2.6, which is close to the frequency ratio between $f = 650\,\mathrm{GHz}$ and $f = 238\,\mathrm{GHz}$. The scan limits in both azimuth and elevation are $\pm 55^\circ$.

2.3.2 Cryogenic electrical measurements

The Nb devices are tested at $T_0 = 4.2\,\mathrm{K}$ in a liquid He cryostat. I–V curves and response to a primitive 77 K blackbody radiation source—an expanded polystyrene foam cup of liquid nitrogen—are read out by either the room-temperature electronics discussed in [60], or a simple resistive-readout bias circuit. A closed-cycle cryogen-free pulse-tube cryorefrigerator is used for testing the NbN devices at temperatures down to $T_0 = 2.6\,\mathrm{K}$. Multiple device I–V curves are measured simultaneously using a multiple-channel version of the room-temperature electronics.

In the limit of zero rf power (P_{rf}) dissipated in the bridge—the small-signal limit—the superconducting I–V curves for Nb and NbN bridges are given by

$$I(V) = \frac{V}{R_n} + \frac{P_{sat}}{V} = \frac{Vwt}{\rho_n l} + \frac{4\kappa(T_c - T_0)wt}{Vl}, \tag{2.23}$$

where $P_{sat} = V_{min}^2/R_n$, V_{min} is the voltage at the minimum in the I–V curve, ρ is the normal-state resistivity of the bridge, and κ is the thermal conductivity of the bridge. The last term in (2.23) is due to ETF. Hotspot superconducting bridge responsivity is $-1/2V_{min}$ when operated at the minimum of the I–V curve (excluding the $R = 0\,\Omega$ superconducting branch). This is the optimum bias point for the readout electronics, which maximizes the SNR [60]. Therefore, devices with lower saturation power are theoretically more sensitive. When radiation is incident on the antenna, adding extra power, the form is

$$I(V) = \frac{V}{R_n}\left\{1 + 2\left[(p_0 + p_e - 1) + \sqrt{(p_0 + p_e + 1)^2 - 4p_0}\right]^{-1}\right\}, \tag{2.24}$$

where the normalized powers are designated $p_0 = P_{rf}/P_{sat}$ and $p_e = V^2/(R_n P_{sat})$ [49]. To examine the effects of the parameters in (2.24) on the I–V curves, we vary the parameters R_n, P_{sat}, and P_{rf}. Resulting I–V curves can be seen in Figures 2.9, 2.10, and 2.11. First, R_n is varied from $100\,\Omega$ to $400\,\Omega$ in Figure 2.9. The result is obvious, in that the normal-state resistance branch of the I–V curve simply changes slope. The asymptote to that branch, at high enough device voltages, is equal to R_n.

Next, P_{sat} is varied from 10 nW to 120 nW, which is a reasonable range for both Nb and NbN devices. No rf power is contributing to the device heating ($P_{rf} = 0\,\mathrm{nW}$), and R_n is fixed at $200\,\Omega$. Given that responsivity is $-1/2V_{min}$ when using the chosen readout electronics scheme [60], it is clear that lower P_{sat} increases responsivity.

In Figure 2.11, P_{rf} is varied from 5 nW to 55 nW, with the normal-state resistance again fixed at $R_n = 200\,\Omega$ and the saturation power set to 40 nW. The trace that passes through the origin is

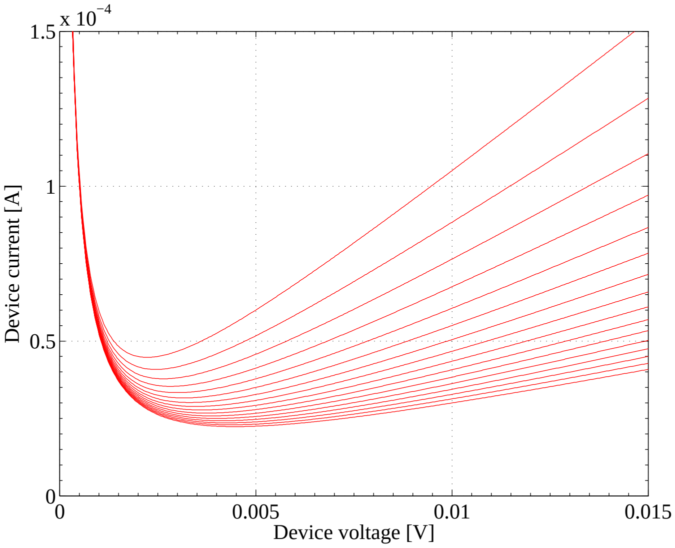

Figure 2.9: Theoretical cryogenic I–V curve varying R_n from 100 Ω to 400 Ω, for $P_{sat} = 50$ nW and $P_{rf} = 0$ nW.

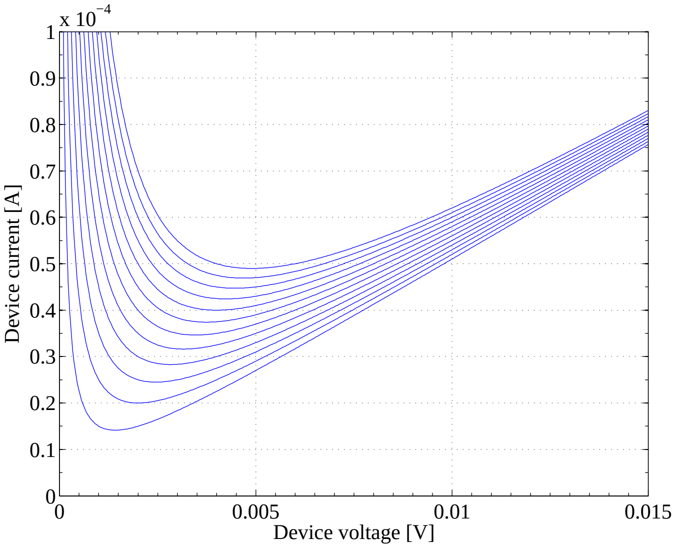

Figure 2.10: Theoretical cryogenic I–V curve varying P_{sat} from 10 nW to 120 nW, for $R_n = 200\,\Omega$ and $P_{rf} = 0$ nW.

for $P_{rf} = 1$ mW, demonstrating the I–V curve of a device that is truly saturated ($P_{rf} \gg P_{sat}$).

Finally, in Figure 2.12, the red curves represent a constant product of $P_{sat} \times R_n$, and the blue curves are a constant quotient of P_{sat}/R_n. In the former case, the product is held constant at $40\,\text{nW} \times 200\,\Omega$, and in the latter the quotient is held constant at $40\,\text{nW} \div 200\,\Omega$.

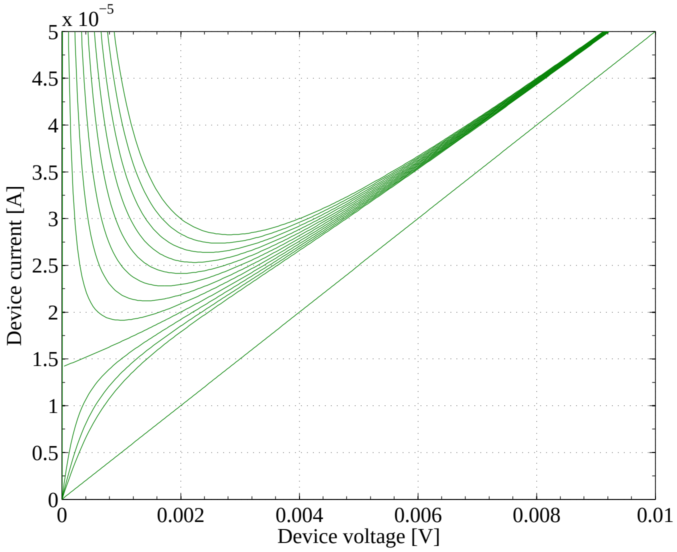

Figure 2.11: Theoretical cryogenic I–V curve varying P_{rf} from $5\,\mathrm{nW}$ to $55\,\mathrm{nW}$, for $R_n = 200\,\Omega$ and $P_{sat} = 40\,\mathrm{nW}$. The curve passing through the origin is for $P_{rf} = 1\,\mathrm{mW}$.

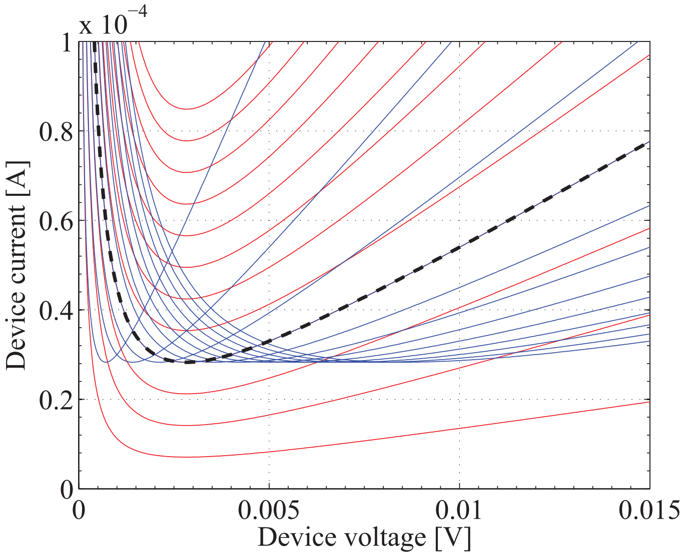

Figure 2.12: Theoretical cryogenic I–V curves, varying both P_{sat} and R_n simultaneously. In the red curves, $40\,\mathrm{nW} \times 200\,\Omega$ is held constant, and in the blue curves, $40\,\mathrm{nW} \div 200\,\Omega$ is held constant.

2.4 RESULTS

The devices are fabricated on several wafers. The wafers with Nb devices on them are referred to as “SC4” and “SC5,” and on each $5\,\mathrm{mm}$ square chip there are three devices, denoted $(-1,-1)$, $(0,0)$, and $(1,1)$. Additionally, there are several chips per wafer, and in this case they are given numeric identifiers. The NbN wafer is denoted “PC05,” and the combination of the antenna and bridge design is given by either “D1” or “D3,” and each chip has a third marker, a letter between A and F, combined with a number between 1 and 12. Combining the three designators for either Nb or NbN ACMBs, each individual device has a unique identifier. Certain devices were not tested on the 5 mm square chips, but rather on 1 × 8 array modules; these devices are noted accordingly.

2.4.1 ROOM-TEMPERATURE I–V MEASUREMENTS

Table 2.1 summarizes results of five Nb devices tested at 300 K. The mean zero-bias resistance, R_0, of the $l = 24\,\mu\mathrm{m}$ bridges is $483\,\Omega$, while the single tested Nb bridge with $l = 12\,\mu\mathrm{m}$ was fitted to $R_0 = 211\,\Omega$. Specific responsivities for $l = 24\,\mu\mathrm{m}$ devices on wafer “SC4” are on average $244\,\mathrm{V}\cdot\mathrm{W}^{-1}\cdot\mathrm{mA}^{-1}$, while for wafer “SC5”, $\beta = 123\,\mathrm{V}\cdot\mathrm{W}^{-1}\cdot\mathrm{mA}^{-1}$, nearly a factor of two lower than on “SC4”, even though the device geometries are nominally identical. A possible explanation is that film thickness is slightly lower on “SC5” than on “SC4” (with a slight difference in width so as to maintain R_0 constant), since dR/dT is a strong function of film thickness at 20 nm, where the Drude mean free path is comparable to thickness.

Table 2.1: Room-temperature parameters for Nb devices, extracted from measured I–V curves fitted to (2.22).

unique identifier	bridge length [µm]	R_0 [Ω]	$\beta\,[\mathrm{V}\cdot\mathrm{W}^{-1}\cdot\mathrm{mA}^{-1}]$
“SC4” NW #1 cent	12	211.3	80.5
“SC4” NE #1 cent	24.5	500.5	266.1
“SC4” NE #2 cent	24.5	481.3	221.1
“SC5” NE #1 cent	24.5	482.8	465.6
“SC5” NE #3 cent	24.5	465.6	123.6

Table 2.2 summarizes the results of ten NbN devices tested at room temperature. Two values of bridge length were tested, $l = 8\,\mu\mathrm{m}$ and $l = 19\,\mu\mathrm{m}$. The mean zero-bias resistance, R_0, for the shorter bridges is $185\,\Omega$, and for the longer bridges $R_0 = 439\,\Omega$. The difference in resistance corresponds exactly to the factor of 2.375 between the two bridge lengths. The responsivity is negative, due to the negative TCR of NbN.

Table 2.2: Room-temperature extracted parameters for measured NbN devices.

unique identifier	bridge length [µm]	R_0 [Ω]	$\beta\,[\mathrm{V \cdot W^{-1} \cdot mA^{-1}}]$
"PC05" D1 F12 cent	8	198.3	−53.3
"PC05" D1 F12 cor1	8	183.1	−49.7
"PC05" D1 F12 cor2	8	183.3	−60.5
"PC05" D1 D8 cent	8	191.6	−56.5
"PC05" D1 F10 cent	8	179.8	−49.8
"PC05" D1 E7 cent	8	184.8	−55.9
"PC05" D3 C8 cent	18.8	409.9	−157.0
"PC05" D3 C8 cor1	18.8	447.9	−183.5
"PC05" D3 C8 cor2	18.8	434.7	−178.4
"PC05" D3 C6 cent	18.8	460.8	−203.8

The mean specific responsivity for bridges of length $l = 8\,\mu\mathrm{m}$ is $\beta = -54\,\mathrm{V \cdot W^{-1} \cdot mA^{-1}}$, while for bridges of length $l = 19\,\mu\mathrm{m}$, the mean responsivity is $\beta = -181\,\mathrm{V \cdot W^{-1} \cdot mA^{-1}}$. The specific responsivity for NbN devices thus lies approximately midway between the values seen for the Nb devices from the two separate, nominally identical wafers. It is noted that NbN bridges can be biased at higher currents, therefore achieving greater effective responsivity, and that the TCR for these devices was not optimized for operation at room temperature.

2.4.2 Cryogenic I–V measurements

Table 2.3 summarizes the fitted parameters R_n, P_{sat}, and P_{rf} (if rf power was incident on the detector) for Nb bridge I–V curves measured at 4.2 K. The Nb devices tested at superconducting temperatures are connected to the feedpoints of antennas with high-frequency cutoffs of $f_c =$ 1.8 THz or 3.6 THz, corresponding to bridge lengths of either $l = 24\,\mu\mathrm{m}$ or $l = 12\,\mu\mathrm{m}$, respectively. The nominal antenna low-frequency cutoff is 200 GHz, although operation below 200 GHz occurs due to bias traces on the Si substrate extending from the arms of the spiral in a dipole-like manner. The mean normal-state resistance, R_n, of the superconducting $l = 24\,\mu\mathrm{m}$ Nb bridges is 217 Ω. Superconducting Nb bridges of length $l = 12\,\mu\mathrm{m}$ have normal-state resistances on average of $R_n = 113\,\Omega$. Bridges of that length that did not superconduct had normal-state resistances on average of 348 Ω. The mean saturation power for $l = 24\,\mu\mathrm{m}$ bridges is $P_{sat} = 16.9\,\mathrm{nW}$, ignoring the outlier "SC4" 1 × 8 1.8 THz SW (2), and for $l = 12\,\mu\mathrm{m}$ bridges is $P_{sat} = 37.4\,\mathrm{nW}$.

Table 2.3: Fitted parameters for Nb devices at $T = 4.2\,\mathrm{K}$. Fits including rf power (P_{rf}) are used when the detector is purposefully exposed to incident radiation from outside the cryostat.

unique identifier	fit parameters			R_n [Ω] lin. fit
	R_n [Ω]	P_{sat} [nW]	P_{rf} [nW]	($T < T_c$)
"SC4" 1×8 1.8 THz SW (2)	226	6.3	n/a	n/a
"SC4" 1×8 1.8 THz SW (3)	242	16.5	n/a	n/a
"SC4" 1×8 1.8 THz SW (5)	199	18.9	n/a	n/a
"SC4" 1×8 1.8 THz SW (6)	190	13.4	n/a	n/a
"SC4" 3.6 THz #1 (0,0) light	113	37.7	9.6	114
"SC4" 3.6 THz #1 (0,0) dark	115	34.4	3.3	118
"SC4" 3.6 THz #4 (0,0) light	112	39.1	4.2	115
"SC4" 3.6 THz #4 (0,0) dark	112	38.5	2.1	115
"SC4" 1.8 THz #2 (1,1) light	227	18.9	5.5	254
"SC5" 1.8 THz #2 (0,0)	n/a	n/a	n/a	380
"SC5" 1.8 THz #3 (1,1)	n/a	n/a	n/a	315

Table 2.4 summarizes four measured superconducting NbN bridges. All superconducting tests were performed on NbN devices of bridge length $l = 8\,\mu\mathrm{m}$. As these devices were tested in a closed-cycle cryorefrigerator enabling control of detector temperature, R_n values were also obtained by increasing T_0 to greater than $T_c \approx 12\,\mathrm{K}$, and measuring I–V curves. Finding R_n in this method is generally more reliable than performing linear fits to the normal region of an I–V curve when $T < T_c$. The mean normal-state resistance of these bridges at approximately $T_0 = 3.8\,\mathrm{K}$ is $283\,\Omega$, extracted from the superconducting fit. A linear fit to the normal region of the I–V curve produces an average R_n—with the single outlier (D8(−1,−1)) ignored—of $293\,\Omega$, while the R_n measured from I–V curves when ($T > T_c$) is on average $290\,\Omega$. The mean saturation power of the NbN devices is $P_{sat} = 113\,\mathrm{nW}$, ignoring the same outlier.

Table 2.4: Fitted parameters for measured NbN devices. In addition to the R_n fits from I–V curves measured at $T_0 = 3.8\,\mathrm{K}$, R_n was measured above T_c.

unique identifier	fit parameters			R_n [Ω] lin. fit	
	R_n [Ω]	P_{sat} [nW]	P_{rf} [nW]	($T < T_c$)	($T > T_c$)
"PC05" D1 F8 $(0, 0)$	234	123	26	282	275
"PC05" D1 F8 $(-1, -1)$	265	111	21	299	n/a
"PC05" D1 D8 $(0, 0)$	283	112	−1.2	304	309
"PC05" D1 D8 $(-1, -1)$	383	80	n/a	389	n/a

Examples of typical measured I–V curves for Nb and NbN devices are shown in Figure 2.13. A clear difference exists between the Nb and NbN devices in saturation power, with the Nb devices exhibiting values a factor of ≈ 5 lower than those of NbN devices whose bridge dimensions have been adjusted to give approximately equal normal-state resistance.

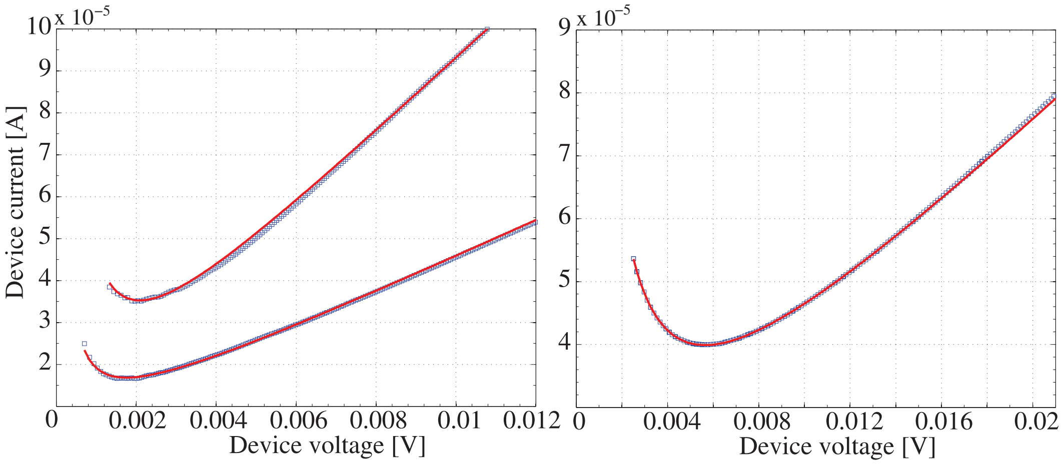

Figure 2.13: Examples of typical superconducting Nb I–V curves for bridge lengths of $l = 12\,\mu\text{m}$ and $l = 24\,\mu\text{m}$ (left). V_{min} is approximately (1.5–2.0) mV for both devices, while the normal-state resistance R_n is a function of bridge length. Saturation power for the shorter bridge is higher than the longer bridge by a factor of 1.6. (right) A typical NbN I–V curve with bridge length $l = 8\,\mu\text{m}$. Saturation power is approximately 115 nW, in the normal range for measured NbN devices; V_{min} is approximately 5.5 mV.

2.4.3 Antenna patterns

Due to the low transmit power—one or two hundred microwatts—of the BWO providing irradiance on the order of several microwatts per square millimeter at the plane of the detector, the dynamic range in the measurements at $f = 650$ GHz is not greater than 22 dB. The BWO beam is formed by a non-standard, smooth-walled conical horn, fed by an overmoded waveguide with dimensions similar to WR-10 (W-band). Measured patterns produced similar results in terms of full-width half-maximum (FWHM) beamwidths and sidelobe levels. Examples of typical antenna patterns taken at $f \approx 650$ GHz are shown in Figure 2.14.

The one-dimensional cuts shown in Figure 2.15 demonstrate decreasing beamwidth with increasing frequency. As expected, the FWHM beamwidths decrease nearly monotonically as a function of frequency, narrowing from (mean of all polarizations) 25° at $f = 95$ GHz to 7°

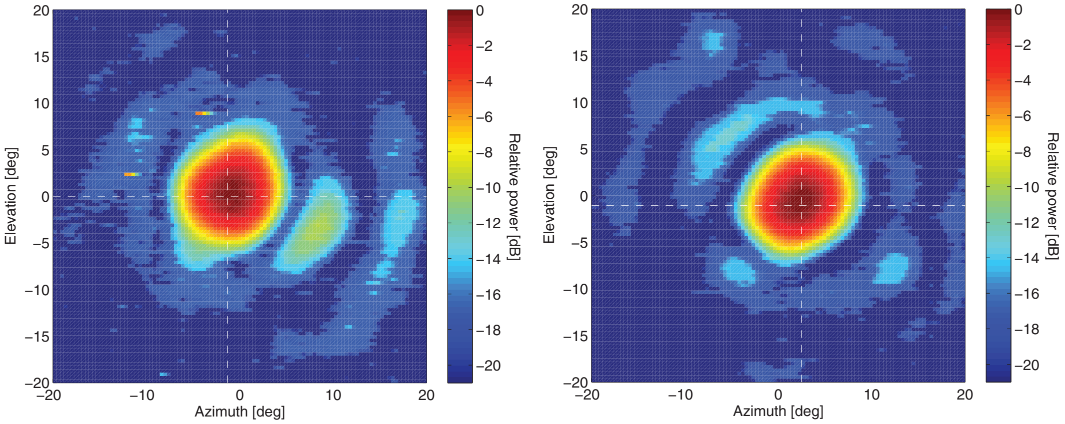

Figure 2.14: Antenna patterns of Nb (left) and NbN (right) devices at $f \approx 650\,\text{GHz}$. The incident field is linearly polarized with the electric field vector in the elevation plane. The bolometer axis is in the azimuth direction. The FWHM beamwidths for the Nb device are $\theta_{az} = 6.7°$ in and $\theta_{el} = 6.6°$, and for the NbN device, $\theta_{az} = 6.7°$ and $\theta_{el} = 6.8°$. The first sidelobe levels are $\approx -10\,\text{dB}$.

approaching the center of the design bandwidth of the spiral antenna, $f = 650\,\text{GHz}$. In-band radiation at angles greater than 48° off broadside, as well as low-frequency radiation, is blocked by the lens mount. In these cases, the measured radiation pattern is no longer a function of only the antenna, but of the entire fixture. It should be noted that $f = 95\,\text{GHz}$ is well below the designed system operating frequency. Cross-polarized radiation at or near the low edge of the operating band will not encounter any significant radiating structures of the antenna or DC traces. On the other hand, co-polarized radiation below the nominal antenna bandwidth will encounter the DC bias traces, which tend to act as a loaded dipole.

A summary of the co- and cross-polarized 2D pattern data from $f = 95\,\text{GHz}$ to $f = 650\,\text{GHz}$ is provided in Table 2.5. The $-3\,\text{dB}$ and $-10\,\text{dB}$ beamwidths for both E- and H-plane cuts are shown. Denoted with (§) are two results at $f = 95\,\text{GHz}$ in which an anomalous reflection affected a portion of the measured data for positive elevation scan angles (seen in Figure 2.15). Adjusting for the reflection, the E-plane co-polarized $-10\,\text{dB}$ beamwidth is reduced to 64.2°; the H-plane cross-polarized $-10\,\text{dB}$ beamwidth becomes 75.8°.

2.4.4 GAUSSICITY

The overall coupling of an antenna to a Gaussian beam can be expressed as

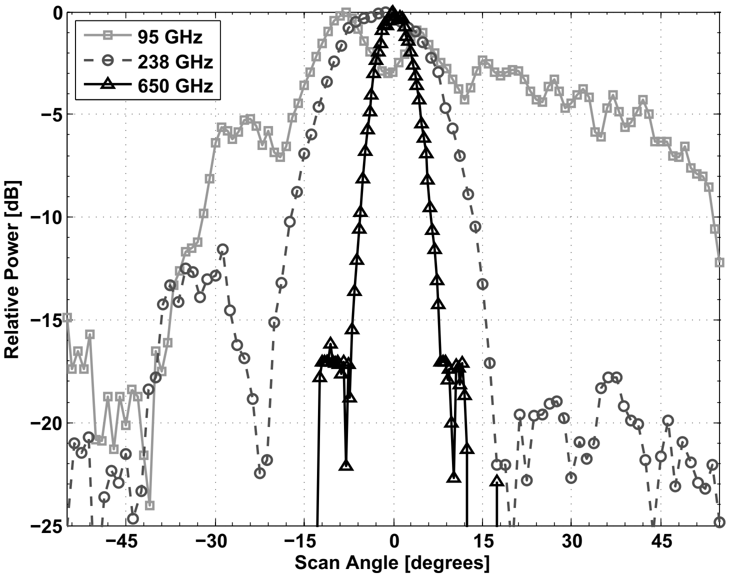

Figure 2.15: One-dimensional E-plane cuts at $f = 650\,\text{GHz}$, $f = 238\,\text{GHz}$, and $f = 95\,\text{GHz}$. The electric field is parallel to the bolometer axis, and the azimuth scan is in the same plane.

$$G = \frac{\int_S E_M E_G^* dS}{\sqrt{\int_S (E_M)^2 dS \int_S (E_G^*)^2 dS}}, \tag{2.25}$$

where the surface integrals are over the 2π steradian half-space, E_M is the measured radiation pattern and E_G is the fundamental mode Gaussian beam [65]. For simplification, we assume that the beam has constant phase, reducing (2.25) to

$$G = \frac{\int_S |E_M(x,y)|\,|E_G(x,y)|\,dS}{\sqrt{\int_S |E_M(x,y)|^2\,dS \int_S |E_G(x,y)|^2\,dS}} \tag{2.26}$$

for $G \in (0,1)$. A two-dimensional Gaussian fit $E_G(x,y)$ is estimated based on the measured radiation pattern. The optimal fit was found by minimizing the sum of square errors between a theoretical Gaussian beam and the measured data. The mean Gaussicity of the two detector orientations at $f = 238\,\text{GHz}$ is $G = 82.8\,\%$, and at $f = 650\,\text{GHz}$, $G = 86.0\,\%$.

2.5 DISCUSSION

Room-temperature testing revealed that although differences in zero-bias resistance and responsivity are found between Nb and NbN devices, the measurement spread of Nb responsivity between

Table 2.5: Summary of measured beamwidths. Polarization and cut are referenced to the incident linearly polarized field as defined in the caption of Figure 2.7.

frequency f	95 GHz		238 GHz		650 GHz	
polarization	cross	co	cross	co	cross	co
−3 dB E-plane	24.7	23.7	21.1	17.5	6.9	6.7
−10 dB E-plane	65.4	85.7§	38.2	29.7	11.1	11.5
−3 dB H-plane	23.0	29.8	18.3	16.6	7.5	7.5
−10 dB H-plane	77.4§	54.3	32.3	26.7	12.1	10.4

wafers is greater than any systematic difference in performance between the materials. Thus a definitive conclusion regarding performance at 300 K of the different materials is not reached. Antenna patterns are, as expected, not functions of bolometer material but of the antenna and substrate lens. Earlier work [66, 67, 63, 68] was verified, and the important design parameter for the optics of imaging systems was confirmed: a FWHM of 4.5 [THz · degrees/f]. This corresponds to an effective antenna area of $A_{eff} = (\pi/4) \cdot (3.9\,\mathrm{mm}^2)$, the size of a diffraction limited aperture equal to the substrate lens size. This result is obtained by using the common approximation for directivity of $D \approx (40\,000)/\mathrm{FWHM}^2$, and $A_e = D\lambda^2/(4\pi)$.

Table 2.6 provides typical parameters of the measured devices at $T_0 = 4.2\,\mathrm{K}$. The measured thermal conductance is obtained by dividing the saturation power by the difference in superconducting transition temperature and base temperature. Though T_c is not routinely measured for either set of devices, spot measurements indicate $T_c \approx 6.5\,\mathrm{K}$ for the Nb devices and $T_c \approx 11.5\,\mathrm{K}$ for the NbN devices. The reliability of T_c values is questionable, but the fact that $(T_c - T_0)$ is several degrees larger for NbN than for Nb is certain.

The discrepancy between the measured thermal conductance G and the value obtained by the Wiedemann-Franz relation

$$\frac{\kappa}{\sigma} = L_0 T \tag{2.27}$$

where L_0 is the Lorenz number ($2.44 \times 10^{-8}\,\mathrm{W} \cdot \Omega \cdot \mathrm{K}^{-2}$), can be explained by introducing a parallel G. In both the Nb and NbN devices, the additive G stems from both phonon conduction

Table 2.6: Comparison of relevant superconducting Nb and NbN parameters. For the Wiedemann-Franz value of thermal conductance G_{w-f}, L_0 is the Lorenz number, G_{elec} is the electrical conductivity ($1/R_n$), and T is the mean bridge temperature.

	Nb	Nb
R_n [Ω]	220 ($l = 24\,\mu\text{m}$)	295 ($l = 8\,\mu\text{m}$)
P_{sat} [nW]	17	120
$(T_c - T_0)$ [K]	$\approx 3^{\dagger}$	$\approx 8.5^{\dagger}$
$G_{meas} = P_{sat}/\left(T_c - T_0\right)$ [$\text{nW} \cdot \text{K}^{-1}$]	5.7	14.1
$G_{w-f} = 4L_0 T G_{elec}$ [$\text{nW} \cdot \text{K}^{-1}$]	2.5	2.6

† Measurement of T_c was not systematic, and is less accurate than the other measured parameters in this table.

in the metal and thermal conduction through the SiO_2, either encapsulating the bridge (Nb) or lying under it (NbN). While the ratio of these contributions is not known, the encapsulating SiO_2 is likely the dominant parallel G for the 20 nm thin-film Nb bridges, while phonon conduction most likely dominates the parallel G for the NbN devices with cross-sectional area a factor of 25 higher than Nb.

In conclusion, it is found that at room temperature, the data do not provide a definitive answer regarding superiority of one material over the other, due to the spread of Nb responsivity between devices from the two wafers tested. At superconducting temperatures, Nb devices are more sensitive, following from their lower saturation power. However, we realize that this performance difference is not significant in most systems, where many other factors play greater roles in overall system performance.

CHAPTER 3

METROLOGY

Metrology is about as sexy as reliability, but just as important.

—H. Bruce Wallace

I promise that Roger [Appleby] and I will make sure metrology talks are, in the future, not saved for the very end of the day.

—D. Wikner, co-chair of *Passive Millimeter-Wave Imaging Technology X*, after the first "ABC Source" presentation

CONTENTS

3.1 INTRODUCTION

The techniques and infrastructure available for the metrology of radiometric power and related quantities in the millimeter-wave and terahertz frequency ranges are far less advanced than at optical and infrared frequencies. However, applications in this frequency range are rapidly emerging [69, 70, 71], and a metrological infrastructure in the form of standardized techniques and hardware would significantly benefit progress in many applications. One example is millimeter-wave remote sensing for atmospheric science, where the importance of accurate calibration and the shortcomings of present calibration targets are widely appreciated [72, 73]. Another example is millimeter-wave/terahertz detector arrays for security applications, in which accurate measurement of noise-equivalent power (NEP) and noise-equivalent temperature difference (NETD) is essential in evaluating device performance. NETD (often seen as NEΔT) is related to the NEP of the detector by

$$\mathrm{NETD} = \frac{\mathrm{NEP}}{\eta k_B \Delta f \sqrt{2\tau_{int}}}, \tag{3.1}$$

where NEP is the noise equivalent power of the detector, η is the overall efficiency of the optical or quasi-optical system (accounting for losses in lenses, filters, pattern matching, etc.), Δf is the rf bandwidth of the detector, and τ_{int} is the post-detection integration time. In most cases, NEP or NETD is the most important factor in determining the overall effectiveness of a security system. The blackbody calibration source described in this chapter has been developed to solve this problem for a particular passive millimeter-wave detector program [7], but the resulting standard is generally applicable for calibration and measurement needs from $f = 100\,\mathrm{GHz}$ to

$f = 1\,\mathrm{THz}$.

In addition to numerous application-specific calibration sources and techniques for infrared radiometers such as in [74, 75], the existing metrology infrastructure for optical and infrared radiometry is comprehensive, rigorous, and widely accepted [76, 77, 78, 79]. Portions of it can be directly adapted to the millimeter-wave/terahertz frequency regime; e.g., high-temperature infrared blackbodies are key components in the traceability chain for infrared power measurements. The Aqueous Blackbody Calibration source presented in this work, hereafter referred to as the "ABC source", represents an effort to bring similarly systematic and traceable measurement techniques to the millimeter-wave/terahertz frequency range.

The purpose of the ABC source is to emit into free space an absolutely calibrated power spectral density (radiometric temperature) in the millimeter-wave to terahertz frequency regime. More specifically, the source enables:

(1) Accurate measurement of the responsivity and NETD of detectors and detector arrays;

(2) An absolutely calibrated source of power, when combined with an appropriate band-pass filter [80, 81, 82];

(3) A scene simulator that generates an accurate radiometric temperature spatial profile when combined with an appropriate mask;

(4) Ultra-wideband frequency response device measurements, since the ABC source emissivity has a well known frequency dependence.

A blackbody source must be highly absorptive and its physical temperature must be accurately known. The Rayleigh-Jeans approximation to Planck's law of blackbody radiation is utilized in this frequency range throughout this chapter, that is, spectral radiance is proportional to temperature—see Equation (1.4).

The most common blackbody source for this frequency range is millimeter-wave anechoic foam soaked in liquid nitrogen ($T = 77\,\mathrm{K}$). Although such foams are relatively good absorbers, and more sophisticated anechoic materials with even lower reflectance exist [83], the foam rarely remains at $T = 77\,\mathrm{K}$ longer than one minute when held in air. Even if left floating in the liquid (constraining the geometry to vertical beams), its radiometric temperature varies unpredictably. Formation of ice on the foam surface increases its reflectance, and moisture increases in the intervening atmosphere and condenses on all exposed surfaces. Heating such anechoic materials is an inadequate alternative because they are poor thermal conductors and therefore do not remain isothermal [73, 84, 85]. Infrared photographs of pyramidal foam panels show the tips of the pyramids closer to ambient temperature than are the pits between pyramids [86]. On the other hand, a well-mixed and easily heated fluid such as water provides an accurate physical temperature (one example that takes advantage of this is an infrared blackbody source utilizing water for temperature control [87]). Moreover, water is extremely lossy at these frequencies, implying high emissivity. Unfortunately, the high dielectric constant of water dictates a high reflectance at a water-air interface, $R_w \approx 30\,\%$ in W-band at normal incidence. This makes the radiometric temperature of a simple water bath highly dependent on the uncontrolled temperature of the ambient surroundings.

The novelty of the ABC source is its operating frequency range. In the visible and infrared spectral bands, many blackbody cavities contain deep grooves or pits with internal corners. The radius of curvature of these corners, and the characteristic size of surface roughness and other manufacturing features is usually comparable to or greater than the wavelength. In the terahertz range, however, the ratio of wavelength to radius of curvature is much larger, and the capabilities and tolerances available from molded expanded polystyrene are completely different than for optical blackbody materials, demanding a new set of cavity geometry constraints. Additionally, material properties in this frequency range are much less well known than at either microwave or infrared/optical frequencies. Given the variety of corrections and uncertainties that must be considered in design of an *absolutely calibrated* source, we chose to adopt a geometry in which all radiometrically active surfaces are planar—a geometry that lends itself to straightforward analysis.

The chapter is organized as follows: Section 3.2 describes the optical trap principle of operation and nominal operating ranges, Section 3.3 presents the uncertainty analysis, Section 3.4 summarizes measurement results, and the Appendix contains the details of the uncertainty analysis. Important symbols are as follows: R (reflectance), T (temperature), and A (absorbance). The subscripts w, e, and m correspond to water, expanded polystyrene (EPS) foam, and mirror, respectively. Additionally, the subscripts r and 0 are used to denote radiometric and ambient temperatures.

3.2 Principle of operation

3.2.1 Optical trap design

An "optical trap" is a component designed in such a way that the power from consecutive specular reflections of incident light is collected and measured, with very little power evading measurement. The initial optical traps were developed by Fox [88] and Gardner [89] and advanced by Lehman and Cromer [90, 91] in the design of absolute power meters for fiber optics. The ABC source geometry can be viewed as a "terahertz trap", with the detector surfaces replaced by water. By reciprocity, it can be considered as either an emitter or an absorber of millimeter-wave/terahertz radiation. In the absorber modality, the surfaces that reflect and detect radiation in the optical trap geometry are replaced in the ABC source by highly absorbing water surfaces, defined by the shape of the "transparent" EPS foam container. Given the reflectance of water (R_w) at an incidence angle of 45° of $R_w \approx 40\,\%$ at $f = 100\,\mathrm{GHz}$ [4], we impose the requirement of at least four reflections from water surfaces at this angle. This rough calculation provides the basis for the design, such that the effective emissivity at the aperture is $\epsilon = \left(1 - R_w^4\right)$ with ideal materials, or $\epsilon = 97.4\,\%$ at $f = 100\,\mathrm{GHz}$, and increases with frequency. Furthermore, the geometry is specified such that the ABC source is polarization-insensitive; i.e., the number of water reflections is divided equally between TE and TM polarizations.

Initially, a simple geometry with two water surfaces and an ideal mirror, shown in Figure 3.1, was simulated using geometric optics. Rays initiating from the 20 cm square entrance aperture in the x-y plane are first incident on a water surface in the $\langle 1, 0, -1\rangle$ plane. Upon specular reflection from the first water surface, a second water surface in the $\langle -1, -1, 0\rangle$ plane is encountered and a second reflection occurs. The third reflection is from an ideal mirror in the $\langle 0, 1, 0\rangle$ plane, after which the geometric optics path is reversed and the rays exit the geometry in the opposite order.

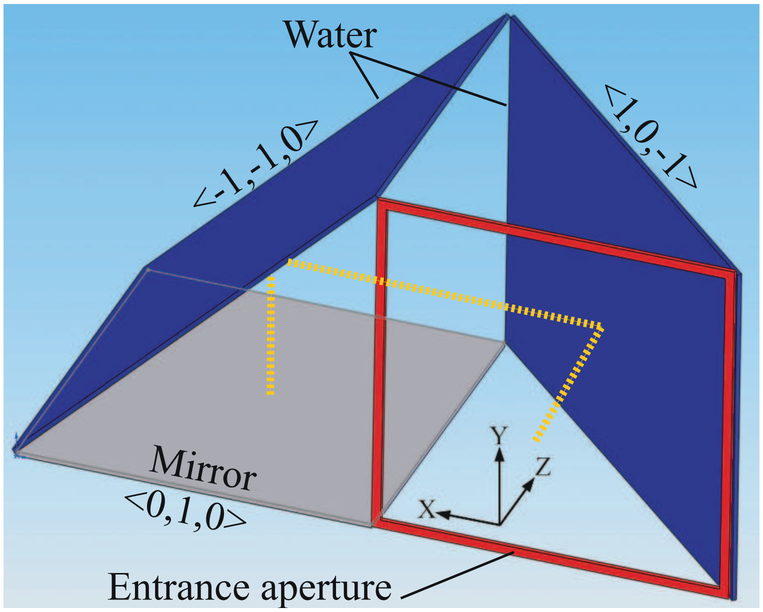

Figure 3.1: A trimetric view of the simplified ABC source geometry. The entrance aperture is defined by the square annulus in the $\langle 0, 0, 1\rangle$ plane; the darker planes ($\langle -1, -1, 0\rangle$ and $\langle 1, 0, -1\rangle$) represent water surfaces; and the light grey plane ($\langle 0, 1, 0\rangle$) corresponds to the ideal mirror. The ray indicated by the thick dashed line enters the center of the aperture normally, and is incident on the center of each water surface and the mirror. Omitted for clarity is the return path following the same ray path, providing two more reflections from water surfaces before exiting the aperture.

An improved design, obtained by extending the two planes in $+z$ until converged, is shown in Figure 3.2 as realized in a fully manufacturable EPS foam geometry. Two cavities in the EPS foam can be defined: one that contains the water, and one in which the entrance aperture is located. Beyond the EPS foam-water interfaces, the shape of the water cavity is irrelevant, other than that its thickness must be great enough that transmittance through the water is negligible, and that the water remains isothermal. In geometric terms, the cavity in which the entrance aperture is located is a prismatoidal pentahedron, created by truncating an apex of a right isosceles tetrahedron; the parallel planes of the remaining pyramidal frustum form similar right isosceles triangles. These parallel planes form the top and bottom of the cavity. Two of the remaining lateral trapezoidal walls are the water surfaces. The remaining plane contains the aperture of the ABC source, defined by a square subtending the acute angle of the trapezoid. Due to manufacturing constraints, an additional 2.5 cm of distance separates the bottom of the cavity from the mirror; this does not adversely affect simulation or test results.

The thickness of the radiometrically relevant EPS foam-water interface walls of the ABC source is 1 cm. Excluding these two 45° walls, all other walls are drafted by 1° to enable removal of the during the fabrication process, and are 2.5 cm thick for structural stability. The overall footprint of the ABC source is 53 cm × 27 cm × 50 cm, and the water volume is about 21 L when filled to within 2 cm of the top.

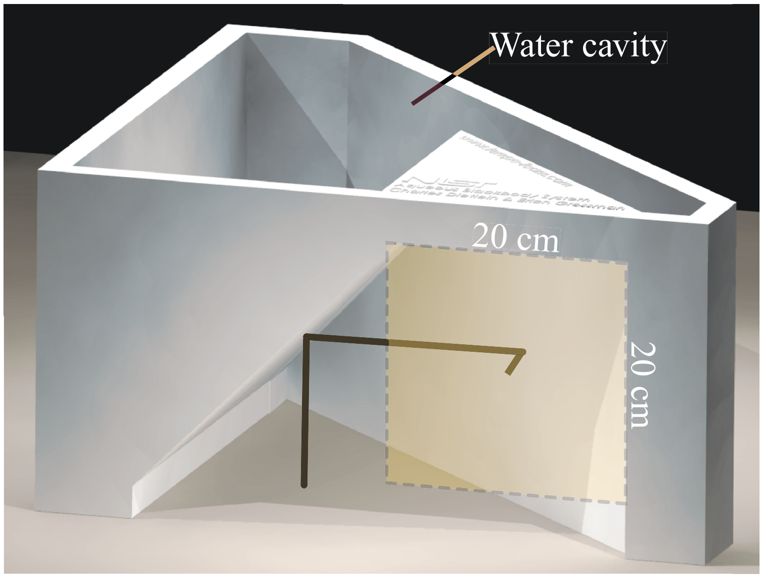

Figure 3.2: A trimetric rendering of the manufactured ABC source. The 20 cm × 20 cm entrance aperture is highlighted by the dashed square and translucent overlay, and the geometric path is indicated by the heavy solid lines. The mirror is omitted for clarity.

3.2.2 Nominal operating ranges

Actual radiometric temperature is a function of position in the plane of the entrance aperture, incidence angle, and frequency. Geometric optics is used to simulate the manufactured geometry described in the previous section. In general, highest performance is found in the center of the entrance aperture for rays that are normal to the entrance aperture. In this context, performance is defined by the fraction of incident rays that are absorbed by a water surface; one minus this quantity is return loss. Figure 3.3 shows the results of geometric optics simulations, varying position and angle of the source in the entrance aperture. The frequency-dependent complex index of refraction, $\hat{n}(f) = n(f) - \jmath k(f)$, from experimental data in [4] is applied to the water surfaces in the ray-tracing simulations, at $f = 200\,\text{GHz}$. It is noted that the exact value of $\hat{n}(f)$ is model dependent, so there is a range of values for $\hat{n}$ at a specific frequency, especially in the range of $f = (50\text{–}200)\,\text{GHz}$, where $\hat{n}$ changes rapidly. The simulation is performed by moving a small bundle of many rays along x and y in the entrance aperture, and at each xy position, varying θ_x or θ_y, and tracing all rays originating from the specific combination of position and orientation. Every ray path is recorded, and at each position and orientation, the total percentage of incident rays that terminate in a water surface is summed. It is seen that when incident ray orientation orthogonal to scan position (abscissae in Figure 3.3) is varied, peak performance—represented by the shaded "sweet spot" in Figure 3.3—is always maintained for $\theta \leq \pm 6^\circ$ and position $\leq \pm 10\,\text{cm}$. When varying orientation coplanar with scan position, performance degrades primarily when the detector is oriented in the same direction as the offset, that is, when it is pointed away from the center of the first water surface. At center, return loss remains at its best value over an angular range of $-6^\circ < \theta < 6^\circ$ for both θ_x and θ_y. At normal incidence, return loss remains at its best value over a spatial range of $-10\,\text{cm} < x < 10\,\text{cm}$ or $-10\,\text{cm} < y < 10\,\text{cm}$. When both position and orientation vary from centered and normal, respectively, incident rays no longer encounter four reflections from water at the desired incidence angle of 45°, and performance falls off, as shown in Figure 3.3.

3.3 RADIOMETRIC TEMPERATURE ACCURACY ANALYSIS

Ideally, the actual radiometric temperature (T_r) of the ABC source is equal to the physical temperature of the water (T_w). In reality, the two differ slightly because of residual dependencies in T_r on ambient temperature (T_0), water temperature spatial nonuniformity, EPS foam loss (A_e), water reflectance (R_w), mirror absorbance (A_m), scattering, stray radiation, diffraction, deformation of the EPS foam walls, and atmospheric attenuation. All of these are frequency dependent, and in this section and the appendix, we discuss these differences quantitatively. Measurement of

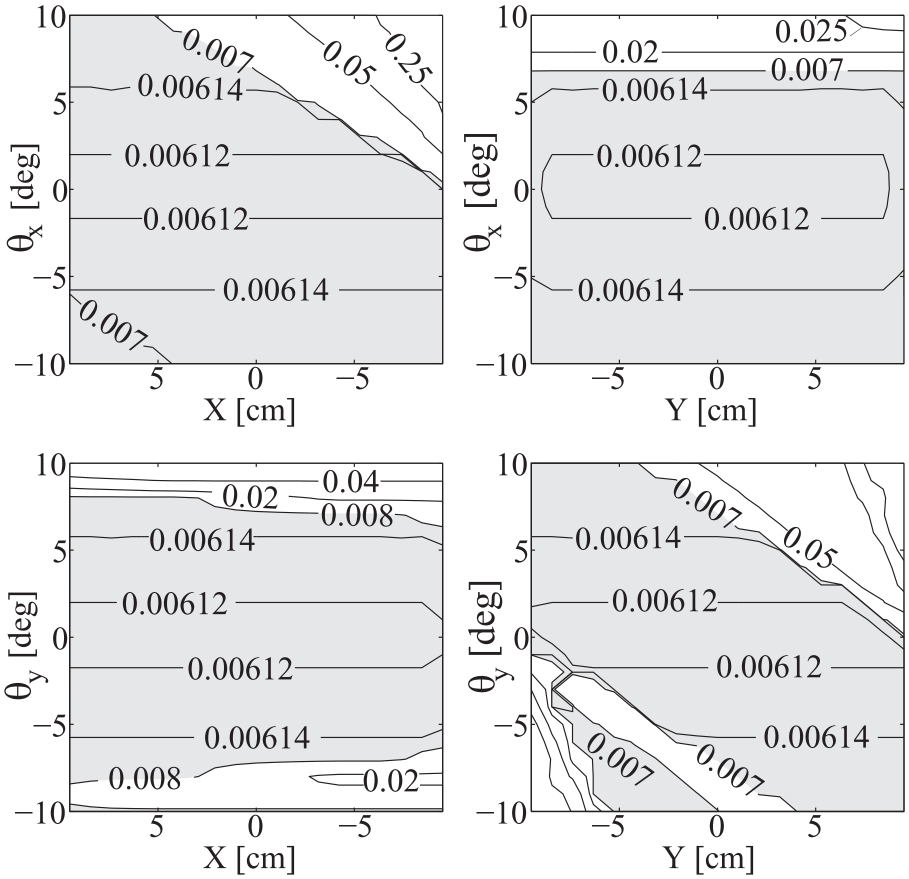

Figure 3.3: Contour plots of performance for the manufactured geometry. Contour values are linear return loss, for $f = 200\,\text{GHz}$, using the model parameters for water from [4]. Note that for the plots on the left, the abscissae coordinates are reversed from standard, to match the notation shown in Figure 3.1. Both plots on the right, where Y is the abscissa, can be rotated 90° counterclockwise to match Figure 3.1. The contour values are *not* evenly spaced, due to rapidly-changing values near the plot edges; additionally, the central region in each plot is shaded to illustrate locations and orientations of high performance, the "sweet spot."

T_r will have errors that can be classified as either correctable biases or uncertainties; furthermore, uncertainties in the corrections can be classified as either Type A or Type B [92]. Some of the above effects result in uncertainties in radiometric temperature that can be summarized in a conventional uncertainty budget, which is presented in Table 3.2 below. The others do not affect the accuracy of T_r, but instead restrict the range of frequency, area, or solid angle over which the uncertainty estimates remain accurate. They do not belong in a conventional uncertainty budget, but they are for completeness summarized in Table 3.3.

3.3.1 WATER TEMPERATURE MEASUREMENT UNCERTAINTY

The most straightforward component of the uncertainty budget is the uncertainty in the measurement of T_w. In the particular implementation of the ABC source used for the measurements described in Section 3.4, a commercial immersion circulator was used to simultaneously mix and heat the water, and six platinum resistance thermometers were placed throughout the volume of the water to measure T_w. The maximum water temperature available from our circulator, which has a maximum power rating of 1100 W, is hot but not scalding, $T_w \approx 65°$ C (333 K). The accuracy of the thermometers is described by DIN IEC 751, which specifies a Type B uncertainty of ±0.24 K for this temperature range [93]. This uncertainty is independent of water temperature and frequency.

3.3.2 WATER TEMPERATURE NONUNIFORMITY

Spatial nonuniformity of the water temperature throughout the water bath could increase the measurement uncertainty of the water temperature, despite use of the circulator. Therefore, the nonuniformity was measured for three cases with water circulated: while ramping up the water temperature at full heater power, while holding the water temperature constant, and while allowing the water to naturally cool to ambient temperature. In both latter cases, the nonuniformity throughout the water volume, as indicated by the readings of the six thermometers, was less than their Type B uncertainty. In the first case, the water was isothermal to within the thermometer uncertainty, except for the water immediately behind the first/fourth water surface, where circulation was poorer. Under full heater power, the temperature lag for this region was approximately $T = 1\,\mathrm{K}$, and the time lag approximately one minute. Therefore, as long as the ABC source is allowed to stabilize for at least one minute before radiometric measurements are begun, the nonuniformity can be neglected and the total uncertainty due to water temperature measurement remains at the ±0.24 K Type B uncertainty of the thermometers.

3.3.3 EPS foam loss

Since EPS foam is the lowest-loss solid material in the frequency range of interest, it has been the object of considerable previous study [5]. For $f > 500\,\mathrm{GHz}$, its transmission properties depend on the specific sample under test. The parameters that affect EPS foam transmission are the initial (pre-expansion) polystyrene bead size, the final density of the expanded material, and thickness; these parameters *also* directly affect its mechanical strength. Transmittance is a stronger function of density than of bead size, but bead size greatly influences the seepage of water into the EPS foam. We chose the smallest commercially available polystyrene bead size ($d < 0.5\,\mathrm{mm}$) in order to minimize water leakage and reduce scattering loss (at a density of 96 g/L, this is the EPS foam used in everyday hot beverage containers). To maintain both structural integrity and high transmittance, a tradeoff in density is made. For a thickness of 1 cm, 100 g/L EPS foam is opaque above $f = (500\text{–}1000)\,\mathrm{GHz}$, but mechanically sturdy. On the other hand, 25 g/L EPS foam has greater than 50 % transmission at $f = 2\,\mathrm{THz}$, but the wall is flexible and permeable to water. Thus, 55 g/L was chosen as a compromise.

The electromagnetic properties—transmittance, absorbance, and scattering—of EPS foam dominate the performance of the ABC source at high frequencies. That is, at high frequencies, the incident radiation not absorbed in water is primarily absorbed in or scattered by the EPS foam walls, which lie at a lower temperature than the water. Because of the sample dependence of EPS foam transmission/scattering properties, our strategy was to measure the loss of the EPS foam actually used in the construction of the ABC source to estimate the EPS foam absorbance A_e. In our measurement, the one-way transmittance of EPS foam with the same density, bead size, and thickness as the manufactured ABC source was measured between $f = 75\,\mathrm{GHz}$ and $f = 200\,\mathrm{GHz}$ by use of a tunable Gunn oscillator and a commercial power meter. In this range, transmission loss for a 1 cm thick EPS foam sample is smaller than the upper limit of $A_e \approx 0.005$, which is set by the stability of the source, and is therefore a Type A uncertainty. An FT-IR spectrometer is utilized at the low end of its operating range for measurements up to $f = 6\,\mathrm{THz}$; combined results from both measurements between $f = 75\,\mathrm{GHz}$ and $f = 1.1\,\mathrm{THz}$ are shown in

Figure 3.4 (transmittance drops to zero by $f = 3\,\mathrm{THz}$ for the specific EPS foam utilized in the ABC source).

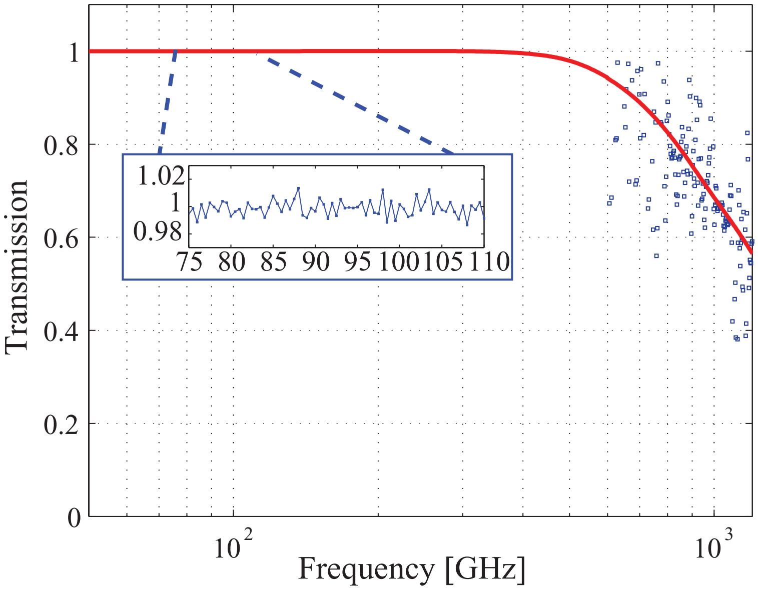

Figure 3.4: Transmission through 1 cm thick EPS foam at normal incidence. $f > 600\,\mathrm{GHz}$ measured with an FT-IR spectrometer, and from $f = 75\,\mathrm{GHz}$ to $f = 200\,\mathrm{GHz}$ measured with a tunable Gunn diode and commercial power meter. Combined data are smoothed by a moving-average filter with a 10 % span and fit to $y = 1/2\{1 + \mathrm{erf}\left[(x-\mu)/(\sigma\sqrt{2})\right]\}$. The inset shows measured data in W-band.

The temperature profile of an EPS foam wall with T_w on one side and T_0 on the other side is a linear ramp from T_0 to T_w, so that the effective temperature T_e of the EPS foam is the mean temperature of the two. Thus, in passing through a single wall of EPS foam whose absorbance is A_e, the radiometric temperature T_r of the blackbody emission from the water is reduced by $\Delta T_r = A_e(T_0 + T_w)/2$ for $A_e \ll 1$. In the Appendix, this basic radiative transfer result is applied to the full ABC source geometry to obtain the effect of a nonzero A_e on the ABC source radiometric temperature.

However, in our transmission measurements, as in those of Zhao et al. [5], true absorption in the EPS foam is not distinguished from scattering. The measured quantity is simply the reduction in power coupled from source to detector. In fact, scattering is thought to be the dominant loss mechanism. To the extent that our measurement of A_e reflects scattering and not absorption, the analysis in the Appendix will overestimate its impact on T_r. This is easily seen in the case of absorption (rather than emission) through a single EPS foam wall: incident radiation that is scattered in the EPS foam will still be absorbed in the water, just not in water directly behind the incident spot on the EPS foam surface. For the full ABC source, this implies that EPS foam scattering would not necessarily reduce the radiometric temperature below T_w within the specified $A\Omega$ of the source. However, the size of the "sweet spot" in position and orientation would diminish somewhat. If the balance between absorption and scattering were known, then the reduction in T_r due to absorption would be a calculable correction with Type A uncertainty, but because the balance is not known, we consider A_e to be a Type B uncertainty when it is greater than the Type A uncertainty from measurements below $f = 200\,\mathrm{GHz}$. In short, the effect of EPS foam loss is that above $f = 200\,\mathrm{GHz}$ the radiometric temperature of the ABC source is not the water temperature, but rather a lower temperature, where the *worst-case* result (i.e., measured transmission loss is treated entirely as absorption) is calculable.

3.3.4 WATER REFLECTANCE

To obtain nonzero reflectance from a water boundary is the reason for adopting an optical trap geometry for a millimeter-wave/terahertz blackbody in the first place. The dielectric constant of liquid water follows a double-Debye model [4] in the millimeter-wave/terahertz frequency regime. By use of this model, the Fresnel coefficients can be obtained for reflectance at 45° incidence from a water and EPS foam interface (assuming an EPS foam refractive index of $n_{EPS} \approx 1$ in W-band). Impurities in water could decrease the performance of the ABC source, but the effect is thought to be very small [94]; all our tests have utilized plain tap water. The temperature of liquid water in this frequency range also modifies its dielectric constant [95]; when four water reflections are encountered, the resulting performance variation is minimal but existent. The result for water reflectance, R_w, at 45° is shown in Figure 3.5 for both polarized and unpolarized radiation at two water temperatures. High reflectance increases radiometric error at low frequencies, but is correctable; the total, four-bounce reflectance of the ABC source is a calculable correction. At $f = 100\,\mathrm{GHz}$, for example, and as demonstrated in the Appendix, the total reflectance is $\approx 0.7\,\%$ (return loss of $-21\,\mathrm{dB}$). The Type B uncertainty in this correction can be deduced from the uncertainty reported in four of the double-Debye model parameters by both [4] and [95], which we have propagated through (3.4) for calculation of the radiometric error (including both corrections and uncertainties).

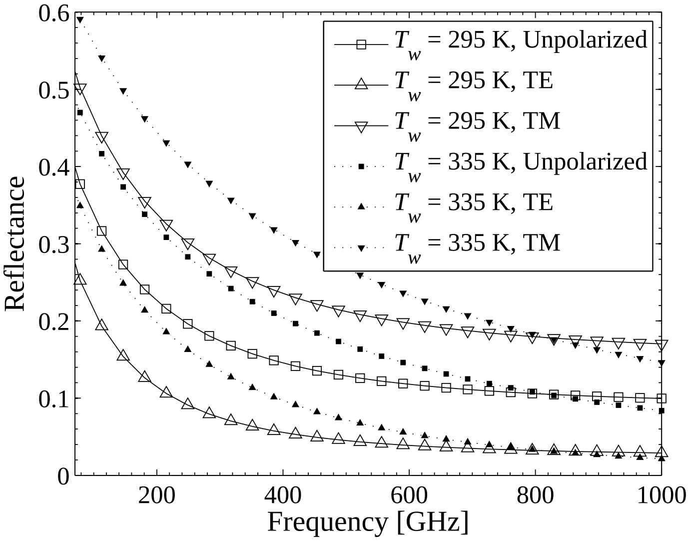

Figure 3.5: Calculated water reflectance R_w at an incidence angle of 45° plotted through the frequency range of interest for polarized and unpolarized radiation, at two physical temperatures.

3.3.5 Mirror reflectance

At millimeter-wave and terahertz frequencies, unpolished metal sheets are not perfect mirrors due to surface roughness and skin effect losses. Reflectivity from a nonmagnetic imperfect conductor can be derived as

$$R_m \approx 1 - 2\sqrt{\frac{4\pi f \epsilon_0}{\sigma}}, \tag{3.2}$$

where σ is conductivity. This approximation is valid for a good conductor, that is, when $(\sigma/\omega\epsilon)^2 \gg 1$. For the case of Al and normal incidence at $f = 100\,\mathrm{GHz}$, $R_m = 0.9989$. Realistic metal mirrors with finite roughness display lower reflectance, though when the rms roughness is small compared to λ, the primary effect is not absorption but low-angle scattering. Ohmic loss in the mirror, A_m, reduces the radiometric temperature of the source, since the physical temperature of the mirror is T_0, but low-angle scattering has much less effect since most of the light scattered into the $A\Omega$ described in Figure 3.3 would come from water at T_w anyway. Because of the difficulty of knowing the true surface roughness of the mirror in the ABC source, and more importantly, the difficulty of estimating the relevant radiometric loss from the surface roughness, we simply assume a large worst-case loss—a Type B uncertainty—of $A_m = 0.05$ for purposes of estimating the uncertainty in T_r. In the Appendix, the effect of non-zero A_m on the radiometric temperature is calculated (3.7).

3.3.6 Other nonidealities

The primary effect of the remaining nonidealities is to reduce the area, solid angle, and/or frequency over which the ABC source maintains its desired radiometric temperature, that is, they do not affect T_r for normal-incidence measurements centered in the entrance aperture. These nonidealities include scattering from the surface of the water, diffraction at the entrance aperture, EPS foam wall deformation, and atmospheric attenuation.

The diameter of the polystyrene beads, post-expansion, is $d = (0.6\text{–}0.7)\,\text{mm}$, but at the nominally flat surface of the EPS foam, the average feature size is approximately 0.1 mm. This corresponds to water surface features ranging in size from $\lambda/30$ to $\lambda/3$, implying that scattering needs to be considered. Scattering manifests itself as decreased specular reflectance and increased diffuse reflectance, gradually reducing the validity of the geometric optics simulations. Rays of unknown origin (i.e., temperature) and incidence angle outside the cone of acceptance are brought into the cone of acceptance via diffuse reflection, and can thus be radiated out of the entrance aperture to a detector. The classic Rayleigh criterion describes the distinction between rough and smooth surfaces as far as phase coherence across a reflected wavefront is concerned. The boundary between "rough" and "smooth" is frequently described as an rms surface roughness of $\xi = \lambda/8$. A more rigorous treatment leads to the result that the ratio of specularly reflected radiation to total reflected radiation is

$$\Upsilon = \exp\left[-\left(\frac{4\pi\xi\cos\theta_i}{\lambda}\right)^2\right], \tag{3.3}$$

where θ is the incidence angle [96]. Using a value for rms roughness of $15\,\mu\text{m}$ based on the measured correlation length (expanded bead size) and peak roughness height (indentation between cells) of the EPS foam, Υ varies from 0.998 at $f = 100\,\mathrm{GHz}$ to 0.969 at $f = 400\,\mathrm{GHz}$. Thus at $f = 400\,\mathrm{GHz}$, approximately 3 % of the total reflected radiation is diffusely reflected from the water according to a distribution function that is dependent upon its statistical surface profile. At this time, the reflectance distribution function is not known, absent a correct model of the water surface profile.

Due to the large bandwidth and electrical size of the ABC source, diffraction should be considered in a complete analysis. If a limiting aperture or defining baffle is introduced at the entrance aperture, diffraction loss will increase, and should be calculated according to the exact geometry implemented. However, in most operating conditions, the emission from the ABC source will overfill the solid angle of the detector, with no limiting or defining aperture. The power lost to diffraction in the nonlimiting aperture case, assuming the detector is at the optimum position and orientation in the aperture, is calculated for the ABC source to be $0 \pm 0.2\,\%$ at W-band, depending on the solid angle subtended by the detector and the formalism used [97, 98]. When the detector is at a nonstandard position or orientation in the entrance aperture, or at a greater distance from the ABC source, diffraction loss must be recalculated accordingly.

Another nonideal condition stems from the compromise of choosing relatively thin and moderate-density EPS foam to enhance transmittance at the expense of mechanical strength. Because of the weight of the water on the second EPS foam-water interface, which is at a 45° angle from vertical, the surface deflects (becomes convex). A two-dimensional sketch of the resulting unfolded optical diagram is shown to scale in Figure 3.6, where the deflection distance at the center of the surface is 4 mm. This deformation restricts the aperture diameter in which four water reflections are encountered. For off-normal or off-center rays, deflection of the second surface can direct rays entirely out of the desired path. If the off-normal rays were incident at an angle larger than 6° as shown in Figure 3.6, the fourth reflection would not occur, or the rays would not exit the entrance aperture despite encountering four water reflections. This can significantly hinder reflectivity measurements, as a slight misalignment (in either angle or position) of the source leads to a displaced reflection. Additionally, the ray triplets are diffused by an amount based on the curvature of the deflected surface; for example, for 4 mm deflection, the off-normal rays exit the aperture at twice their initial separation distance.

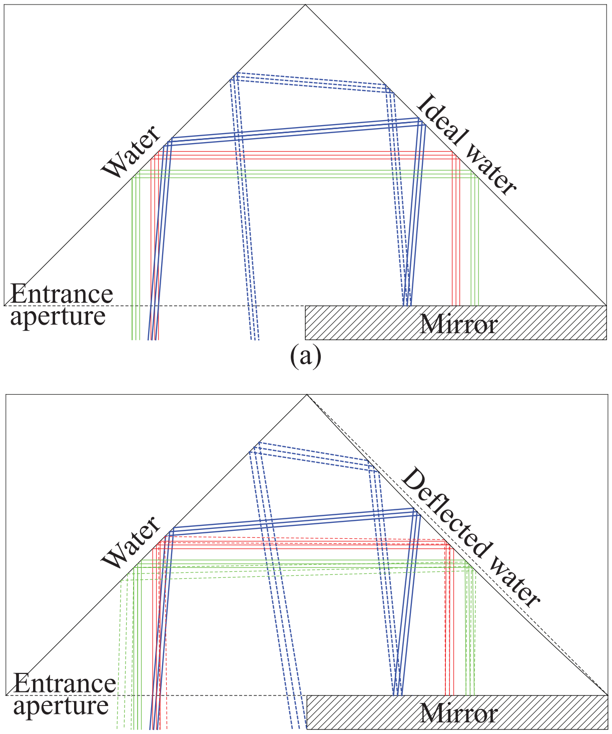

(a)

(b)

Figure 3.6: Sketches (to scale) of ideal unfolded geometry (a) and non-ideal geometry with convex second reflection surface (b). The red rays are the central rays, the blue rays are centered in the entrance aperture but rotated 5° from normal, and the green rays are normal to the aperture but offset from the center by 2.5 cm. The deflection at the center of the non-ideal curved surface is 4 mm from the ideal flat surface. It is clear that the rays entering the aperture at the off-normal angle are affected the most by the deflected water surface. Note that besides the obvious translation for the off-center and off-normal incident rays, the ray triplets upon exiting are twice their initial separation.

One last effect must be considered: in the millimeter-wave/terahertz frequency range, atmospheric attenuation at sea level with 100 % humidity increases from 0.002 dB/m at $f = 100$ GHz to 0.2 dB/m just above $f = 1$ THz [2]. Table 3.1 shows the frequency ranges where the attenuation through the effective path length in the ABC source (0.5 m) is greater than 2 % at sea level, with 50 % relative humidity, at 295 K. We emphasize that the ABC source is intended for indoor laboratory use, where 50 % relative humidity is a reasonable upper limit. If a broadband detector is used, its frequency response needs to be calibrated to account for the absorption bands provided in Table 3.1. Pressure and humidity should be estimated for the specific location where the ABC source is used, and radiometric temperature corrected for the environment.

Table 3.1: Atmospheric bands below 1 THz where attenuation exceeds 2 %[†]

f_{start} [GHz]	f_{peak} [GHz]	f_{end} [GHz]	peak attenuation [dB]
376.8	380.2	383.7	0.1856
444.0	448.0	451.8	0.2211
520.6	557.0	600.1	10.45
615.5	620.7	624.9	0.1957
720.3	752.0	787.0	7.245
909.5	916.2	923.2	0.3717
955.4	—	—	—

[†] Calculated for atmospheric conditions of $T = 295\,\mathrm{K}$, 101.325 kPa (mean sea-level pressure), and 50 % relative humidity. Distance is 0.5 m, the mean path length in the ABC source. For the band beginning at $f = 955.4\,\mathrm{GHz}$, attenuation does not drop below 2 % before $f = 1\,\mathrm{THz}$, indicated by the "—" dashes.

The nonidealities discussed in this subsection are included for completeness, but do not appear in the uncertainty budget because they do not affect T_r under normal operating conditions.

3.3.7 SUMMARY OF RADIOMETRIC ACCURACY

The radiometric temperature T_r at the entrance aperture of the ABC source can be calculated, under certain assumptions, from radiative transfer as described in the Appendix. The radiometric temperature error is plotted vs. frequency in in Figure 3.7, where T_r is obtained from (3.4). As mentioned above, performance at low frequencies is reduced primarily by R_w and is a calculable correction, and at high frequencies primarily by A_e, and is an uncertainty. To generate Figure 3.7, the frequency dependence of R_w was taken from the calculations based on Kindt and Schmuttenmaer [4] and Rønne et al. [95] (displayed in Figure 3.5), and the error bars below $f = 250\,\mathrm{GHz}$ are deduced from their uncertainty reported in the double-Debye model parameters. The frequency dependence of A_e was obtained by fitting the measurements described in Section 3.3.3 and Figure 3.4 to the form $y = 1/2\{1 + \mathrm{erf}\left[(x - \mu)/(\sigma\sqrt{2})\right]\}$—a low-pass filter form—and is responsible for the error bars above $f = 300\,\mathrm{GHz}$. Mirror absorbance as a function of frequency was set to (3.2). The uncertainty in T_w is not shown in this plot in order to emphasize the roles of uncertainty from R_w and A_e. The plotted quantity is $T_r - T_w$, the error in the measured quantity. For example, if a measurement is performed at 200 GHz with a desired signal of $T_w - T_0 = 40\,\mathrm{K}$, a calibrated radiometer will measure a signal of 39.6 K. Adding the correction of 0.4 K (as per (3.4) and Figure 3.7) eliminates the measurement error; the combined uncertainty at $f = 200\,\mathrm{GHz}$ in the parameters of (3.4) is approximately ±0.40 K, using the root-sum-square (RSS) method.

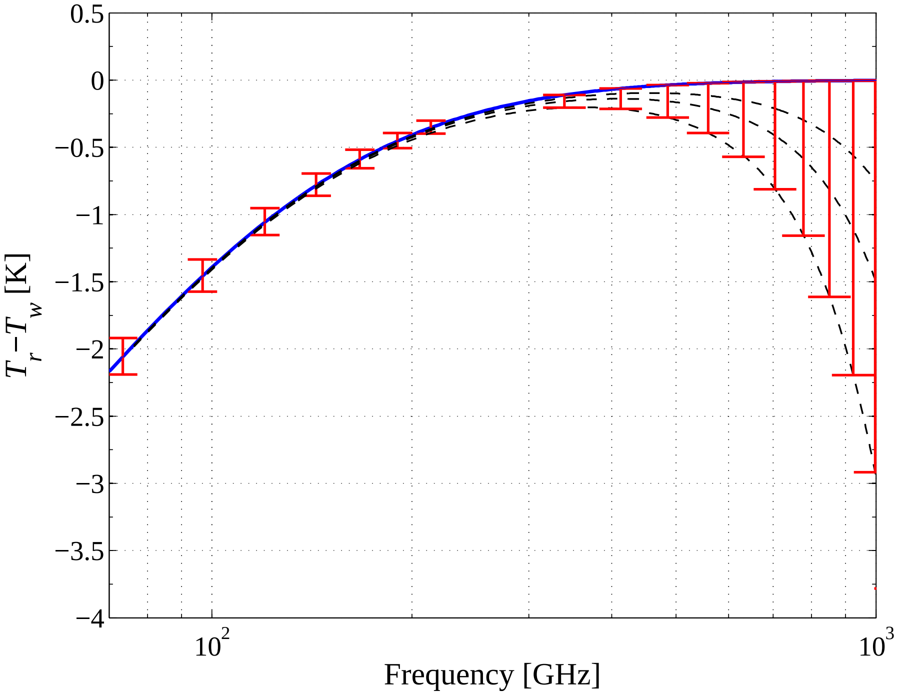

Figure 3.7: Radiometric temperature *correction* (thick solid line) as a function of frequency, for a typical signal strength of $T_w - T_0 = 40\,\mathrm{K}$, where $T_w = 333\,\mathrm{K}$. The error bars below $f = 250\,\mathrm{GHz}$ are obtained from the reported uncertainty in the double-Debye water model fit parameters from[4] and [95], and the error bars above $f = 300\,\mathrm{GHz}$ are due to the unknown balance between absorption and scattering in the EPS foam. The dashed lines indicate the corrections that would occur, rather than uncertainty, if A_e were known to be 25 %, 50 %, or 100 % absorption, from top to bottom.

Table 3.2 summarizes the uncertainty analysis at two frequencies, $f = 100\,\mathrm{GHz}$ and $f = 500\,\mathrm{GHz}$. At W-band, the radiometric temperature correction for the ABC source is +1.5 K for a 40 K signal ($T_w = 333\,\mathrm{K}$), and the combined uncertainty (RSS method) is ±0.40 K. The thermometry uncertainty accounts for ±0.23 K, and uncertainties in R_w—shown in Figure 3.7—A_e, and A_m, account for the remainder. At $f = 500\,\mathrm{GHz}$, the correction is +30 mK, and the combined uncertainty is ±0.37 K.

Table 3.2: Uncertainty budget: uncertainty in T_r due to uncertainties in parameters of (3.4) for $T_w = 333\,\mathrm{K}$ and $T_0 = 293\,\mathrm{K}$.

	$f = 100\,\mathrm{GHz}$		$f = 500\,\mathrm{GHz}$	
	value	result [K]	value	result [K]
water temperature T_w [K]	333.0 ± 0.24	±0.23	333.0 ± 0.24	±0.24
EPS foam absorbance A_e	0 ± 0.007	±0.27	$0 + 0.02$	±0.28
mirror absorbance A_m	$0 + 0.05$	±0.15	$0 + 0.05$	±0.03
water reflectance R_w	0.432 ± 0.009	±0.12	0.167 ± 0.011	±0.01
combined uncertainty [K]		±0.40		±0.37

The effects of scattering, roughness, EPS foam deflection, diffraction, and atmospheric absorption are shown in Table 3.3. Rather than adding uncertainty or an additional correction, they limit the range over which the radiometric temperature accuracy is valid. Based on the previous discussion, scattering and roughness are negligible at lower frequencies. Correction due to atmospheric attenuation contributes only in the noted frequency ranges (Table 3.1), where its value is significantly comparable to the other uncertainties. Scattering at high frequencies and EPS foam deflection limit the area and solid angle to a smaller range in area and solid angle than the nominal range indicated in Figure 3.3. Reduction of radiative transfer and/or $A\Omega$ due to diffraction is calculable [97, 98], or avoidable with use of the proper measurement geometry.

Table 3.3: Other effects

Category	Effect	Remedy
atmospheric transmission	radiative transfer reduction	calculate; see Table 3.1
EPS foam deflection	reduction of $A\Omega$	ensure $\theta_{x,y} < 6^\circ$
spatial non-uniformity of T_w	introduces a minimum time between ΔT_w and radiometric measurement	wait 1 minute
water surface scattering	reduction of $A\Omega$	calculate; see [96]
diffraction	geometry-dependent reduction of $A\Omega$	calculate; see [97, 98]

3.4 REFLECTIVITY MEASUREMENTS

An estimate of the effective emissivity of the ABC source can be obtained by measuring the reflected power of a source that is directed into the entrance aperture. Because of the absorbance of liquid water, the effective emissivity will equal (1 − reflectance) when all reflected power is measured. This reflectance is measured by spatially integrating the reflected power when the container is filled with water, and then dividing by the integrated reflected power when mirrors replace the water surfaces. This is a valid approach as long as the entire reflected beam is contained in the mapped region. Integrated reflected power measured with mirrors in place of water is corrected for imperfect mirror reflectance.

To validate the ABC source design, a set of reflectance measurements was performed between $f = (80\text{–}260)\,\mathrm{GHz}$, where sources and detectors were readily available. Although limited, these measurements verify predicted water reflectance at the measured frequencies, justifying confidence throughout the band. For reflectance measurements, the incident beam from a corrugated conical horn antenna ($w_0 = 7\,\mathrm{mm}$) located in one half of the entrance aperture is directed such that the reflection is in the other half of the entrance aperture. In some cases, polytetrafluoroethylene (PTFE) lenses (focal length $\approx 21\,\mathrm{cm}$) are used to collimate the incident beam in a standard manner described in [99], such that the collimated beam waist lies in the plane of the mapping ($d_1 = 21\,\mathrm{cm}$ and $d_2 = 89\,\mathrm{cm}$, where d_1 is the distance from the horn aperture to the lens, and d_2 is the distance from the lens to the beam waist). Figure 3.8 contains examples of measured reflectance maps with mirrors (left) and water (right), for a collimated $f = 105\,\mathrm{GHz}$ incident beam. The reflection from the water surfaces is spatially shifted *and* diffused, corresponding to the geometry illustrated by Figure 3.6 due to the curvature of the second EPS foam-water interface. Table 3.4 summarizes the measured reflectance at several frequencies in W-band and at $f = 260\,\mathrm{GHz}$. All measurements all lie within the corrections predicted from the Appendix.

Radiometric accuracy implied by these measurements is within the uncertainty of the value $(1 - R_w^4)$. This is not surprising, given that the uncertainty in the lower half of the frequency range is not dominated by the uncertainty from the EPS foam. These results provide confidence in the correction for the residual reflectance due to water, Equation (3.8).

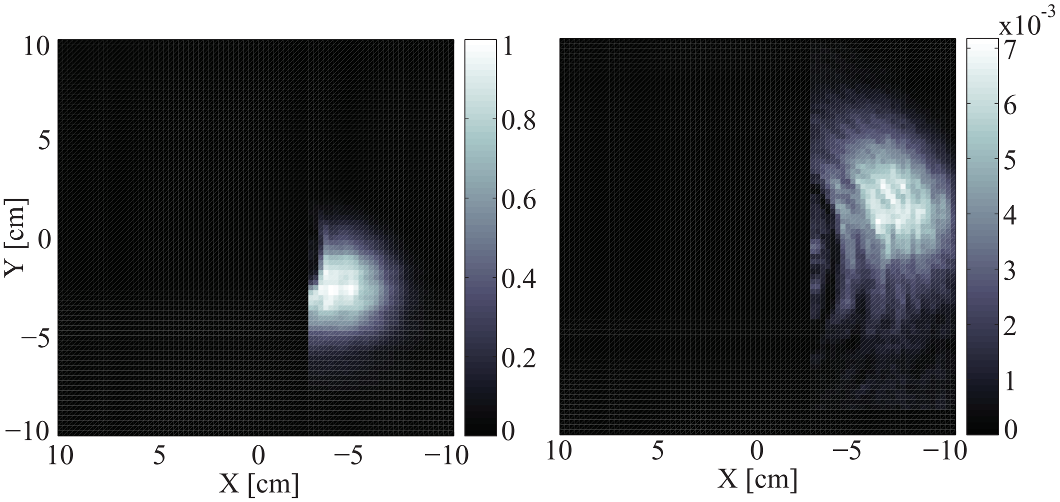

Figure 3.8: Measured reflectance maps for mirror surfaces (left) and water surface (right). The maps match the size of the entrance aperture; the focusing lens blocks the leftmost 12 cm of the entrance aperture from being scanned by the detector; the nominal specular reflection is in the rightmost 8 cm (the mappable region). The PTFE lens shadow can be seen (left), as well as the distorted and displaced beam (right) due to the curved water surface (Figure 3.6).

Table 3.4: Summary of reflectance measurements

Frequency [GHz]	Reflected power [%]
83	1.21
105	0.75
105 (w/lens)	1.45
260	$< 0.15^{\dagger}$

† At $f = 260$ GHz, measured reflection maps from water surfaces were indistinguishable (within 95 % confidence intervals, when fitted to a Rayleigh or Gaussian distribution) from reflection maps taken with the source blocked; 0.15 % is a statistical upper bound.

3.5 CONCLUSION

We have presented the first calibrated broadband blackbody source developed as part of a new metrology infrastructure for the millimeter-wave/terahertz frequency range. The ABC source is easy to fabricate, inexpensive to manufacture and operate, reproducible, scalable, and easily adaptable to a variety of measurement scenarios. Uncertainty from W-band to $f = 300$ GHz is no less than ±0.24 K, due to the accuracy of the thermometry, and also depends on the published uncertainty in the complex refractive index of water. Above $f = 350\,\mathrm{GHz}$, uncertainty is dominated by the unknown balance between absorption and scattering in the EPS foam. If the balance were better known, a correction would be applied, and uncertainty would be reduced. The measured reflectance results agree with the predicted values up to the highest measured frequency, $f = 260\,\mathrm{GHz}$. In the future, validation will be extended to higher frequencies with a new set of sources and detectors, and in the following chapter, the balance between transmission and scattering in EPS foam will be examined.

APPENDIX

In contrast to many infrared blackbodies, the geometry of the ABC source is simple enough that the effects of the secondary dependencies of T_r on other parameters—for example, EPS foam loss—can be analytically calculated. These calculations are outlined here. The assumptions made are as follows:

(1) Transmission through the water behind each EPS foam-water interface is zero. Therefore, $R_w + A_w = 1$.

(2) Transmission through the mirror is zero. Therefore, $R_m + A_m = 1$.

(3) Reflectance off each air-EPS interface is zero. Therefore, $\tau_e + A_e = 1$. This is valid because the EPS foam refractive index, n_{EPS}, is close to unity [5]. We further assume that the single-pass EPS foam absorbance is small ($A_e \ll 1$) so that for a multi-pass situation, $(1 - A_e)^p = (1 - pA_e)$, where p is the number of passes.

(4) Volume scattering within the EPS foam is negligible, and surface scattering (diffuse reflection) at the EPS foam-water interfaces is also negligible. This is discussed in the main text.

(5) Coherent effects, particularly coherent interference between multiple reflections, can be neglected. This is reasonable given that the ABC source is intended as an emitter of *broadband* radiation; over a sufficiently broad bandwidth, coherent interference (standing

waves) is blurred beyond discrimination. This minimum bandwidth is the free spectral range (FSR) of the shortest cavity formed within the system. The smallest dimension is the wall thickness, $t = 1\,\mathrm{cm}$; this yields an FSR of $c/2n_{EPS}t = 15\,\mathrm{GHz}$.

Neglecting coherence, the analysis of radiative transfer through the ABC source is greatly simplified. The radiometric temperature at plane $(i-1)$, $T_r^{(i-1)}$, is transformed into a radiometric temperature at plane (i), $T_r^{(i)}$, according to

$$\begin{aligned}
T_r^{(i)} &= (1-A_e)T_r^{(i-1)} + A_e T_e \quad \text{transmission through an EPS foam layer at temperature } T_e,\\
T_r^{(i)} &= R_w T_r^{(i-1)} + (1-R_w)T_w \quad \text{reflection off an EPS foam-water interface, and}\\
T_r^{(i)} &= R_m T_r^{(i-1)} + (1-R_m)T_m \quad \text{reflection off an imperfect mirror at temperature } T_m.
\end{aligned}$$

Based on the above assumptions, the radiometric temperature at the entrance aperture is given in terms of the water, EPS foam, mirror, and ambient temperatures by

$$\begin{aligned}
T_r = T_w&(1-A_e)(1-R_w)\Big[1 + R_w(1-A_e)^2 + R_w^2(1-A_e)^4(1-A_m)\\
&\qquad + R_w^3(1-A_e)^6(1-A_m)\Big]\\
&+ T_e A_e\Big\{1 + R_w\left(A_e^2 - 3A_e + 2\right) + R_w^2(1-A_e)^3\left[A_e(A_m-1) - A_m + 2\right]\\
&\qquad + R_w^3(2-A_e)(1-A_e)^5(1-A_m) + R_w^4(1-A_e)^7(1-A_m)\Big\}\\
&+ T_m A_m R_w^2(1-A_e)^4\\
&+ T_0 R_w^4(1-A_e)^8(1-A_m).
\end{aligned} \tag{3.4}$$

This expression enables us to estimate the systematic uncertainties or corrections in radiometric temperature due to non-ideal materials. A known deviation of A_e, A_m, or R_w from zero produces a calculable correction in T_r, and an uncertainty in A_e, A_m, or R_w produces an uncertainty in T_r that is calculable through the law of propagation of uncertainty [92]. We evaluate these uncertainties quantitatively, using our best estimates for A_e, A_m, and R_w, and their frequency dependence. The general formulae are given below, while the numerical values for various uncertainties at two particular frequencies ($f = 100\,\mathrm{GHz}$ and $f = 500\,\mathrm{GHz}$) at a signal strength of ($T_w - T_0 = 40\,\mathrm{K}$) are summarized in Table 3.2. We use the facts that the mirror temperature is ambient and the effective EPS foam temperature is the mean between the water and ambient temperatures, that is, $T_m = T_0$ and $T_e = (T_w + T_0)/2$, and $(1 - A_e)^p = (1 - pA_e)$ to simplify (3.4), yielding

$$\begin{aligned}
T_r = {} & T_w(1 - A_e)(1 - R_w)\Big[1 + R_w(1 - 2A_e) + R_w^2(1 - 4A_e)(1 - A_m) \\
& \qquad + R_w^3(1 - 6A_e)(1 - A_m)\Big] \\
& + \left(\frac{T_w + T_0}{2}\right) A_e \Big[1 + R_w(1 - A_e) + R_w(1 - 2A_e) + R_w^2(1 - 3A_e) + R_w^2(1 - 4A_e)(1 - A_m) \\
& \qquad + R_w^3(1 - 5A_e)(1 - A_m) + R_w^3(1 - 6A_e)(1 - A_m) + R_w^4(1 - 7A_e)(1 - A_m)\Big] \\
& + T_0 A_m R_w^2(1 - 4A_e) \\
& + T_0 R_w^4(1 - 8A_e)(1 - A_m).
\end{aligned} \tag{3.5}$$

The idea is to expand the radiometric error in T_r from (3.5) by a Taylor expansion about the nominal values of A_e, R_w, A_m, and T_w. The corrections and uncertainties due to A_e, A_m, and R_w are all proportional to signal strength in an actual measurement, because the difference between T_r and T_0 is the measured quantity. The uncertainty in T_r due to the unknown balance between EPS foam scattering and absorption, embodied by the term A_e, is given by

$$\begin{aligned}
\left|\frac{\partial T_r}{\partial A_e}\right| \Delta A_e = \Delta A_e \big[& (T_0 - T_w)\left(1/2 + R_w + R_w^2 + R_w^3 - 15/2R_w^4\right) \\
& + T_0\left(-3A_eR_w - 7A_eR_w^2 - 11A_eR_w^3 - 7A_eR_w^4\right) \\
& + T_w\left(A_eR_w - 3A_eR_w^2 - 7A_eR_w - 14A_eR_w^4\right)\big],
\end{aligned} \tag{3.6}$$

where ΔA_e is the uncertainty in A_e. At $f = 100\,\mathrm{GHz}$, $\Delta A_e < 0.005 \times \sqrt{2} = 0.0071$, and at high frequencies from the measurements shown in Figure 3.4. If $A_e = 0$, we are assigning all loss to scattering, rather than absorption. The correction in T_r due to the calculable mirror absorption A_m is obtained by setting A_m equal to (3.2). This is negligible compared to other corrections and uncertainties. The uncertainty is given by

$$\left|\frac{\partial T_r}{\partial A_m}\right| \Delta A_m = -\Delta A_m \left(T_0 - T_w\right)\left(R_w^2 - R_w^4\right) \tag{3.7}$$

At both $f = 100\,\mathrm{GHz}$ and $f = 500\,\mathrm{GHz}$ we set A_m to 0.05, as mentioned in the prior discussions. Next, we address the finite reflectance of water. The value

$$T_r - T_w = -R_w^4 \left(T_w - T_0\right) \tag{3.8}$$

is a calculable correction for the finite return loss of the ABC source, due to the non-zero reflectivity of water. The uncertainty in this correction is determined by the uncertainty in R_w, which results from the uncertainty in the complex refractive index measurements of water by Kindt and Schmuttenmaer [4] and Rønne et al. [95]. The uncertainty in (3.4) due to the uncertainty in R_w is therefore given by

$$\left|\frac{\partial T_r}{\partial R_w}\right| \Delta R_w = \Delta R_w \left(T_0 - T_w\right) 4R_w^3. \tag{3.9}$$

Finally, we examine the effect of uncertainty in T_w, given by

$$\left|\frac{\partial T_r}{\partial T_w}\right| \Delta T_w = \Delta T_w \left(1 - R_w^4\right), \tag{3.10}$$

which shows that for an uncertainty in T_w (the Type B uncertainty in the thermometry), the resulting uncertainty in T_r is essentially the same.

CHAPTER 4

EXPANDED POLYSTYRENE FOAM SCATTERING

Intellect takes you to the door, but it doesn't take you into the house.

—Shams-e-Tabrizi

CONTENTS

4.1 INTRODUCTION

Conventional measurements of millimeter-wave and terahertz material loss measure only the difference in power coupled from source to detector when a sample is introduced. They therefore do not distinguish between absorption and scattering; effects such as grating lobes due to periodic structure are neglected, and beam broadening in reflectivity measurements due to diffuse reflectance from, for example, surface roughness, is not measured. The distinction between scattering and true absorption is an issue in both active and passive millimeter-wave/terahertz imaging. Clothing can be strongly absorptive, transmissive, and specularly or diffusely reflective or scattering; each attribute contributes in some manner to the final image that is observed in the millimeter-wave/terahertz frequency range. If periodic structure is present in the clothing, for example with corduroy, low-level grating lobes would appear in images acquired with narrowband imaging systems. These grating lobes have the possibility of obscuring concealed objects. Similarly, diffusely and specularly reflecting objects appear quite different in active and passive modalities. Objects with flat surfaces or corners produce "glint" in active images, greatly hindering their identification. To a passive system, however, the objects appear quite normal because the thermal radiation incident upon them does not originate from a single point.

Previous work has measured transmission through clothing samples in the millimeter-wave and infrared regimes [100] and building materials [35], but did not specifically consider scattering. The precise distinction between scattering and absorption plays an important role in radiometric scene simulation [101, 102], as well as the scattering/reflectance balance of building materials. A reflectometer has been built to measure broadening of specularly-reflected radiation for the latter purpose [103], and is essentially a predecessor to the system described in this chapter.

Besides imaging applications, components and systems in this frequency range often require extremely low-loss materials. One pertinent example of such a system requiring a low-loss structural material is the Aqueous Blackbody Calibration (ABC) source, discussed in Chapter 3. Its radiometric uncertainty at high frequencies (above $f = 450\,\mathrm{GHz}$) is determined by the nature of the balance between scattering and absorption in the expanded polystyrene (EPS) foam container that holds the water in its specific geometry. The effect is as follows: instead of the physical temperature of the water being equal to the radiometric temperature (as desired), the latter is decreased due to a finite amount of loss in the EPS foam. If all measured loss is considered to be absorption and the reflected radiation from the EPS foam is negligible, then the radiometric temperature of a bath of water behind an EPS foam wall is reduced by an amount equal to the fractional absorption multiplied by the mean of the ambient and water temperatures. On the other hand, if the loss is not absorption, but rather scattering, the radiometric temperature will be much closer to that of the physical water temperature. Previous measurements of polystyrene foam focused on determination of the dielectric constant, but were not sensitive to scattering, though scattering was suggested as a probable loss mechanism [5]. Scattering in the case of the EPS foam in the ABC source is looked at as a favorable alternative to absorption, and indeed the expected extinction mechanism. The goal in this chapter is to measure the balance between transmission, scattering, and reflection in EPS foam, and from these measurements, determine the percentage of absorbed power.

4.2 Experimental setup

4.2.1 Hardware

A superconducting ($T = 4.2\,\mathrm{K}$) antenna-coupled microbolometer [49] (see Chapter 2) is located in a liquid helium-cooled cryostat on a platform approximately 0.5 m above an optics table. The self-complementary spiral antenna has a design frequency range of $f = 0.1\,\mathrm{THz}$ to $f = 1.8\,\mathrm{THz}$ and is circularly polarized. The microbolometer is voltage biased and operated with room-temperature electronics [60] providing negative electrothermal feedback [104]. Cooled filters at each of the two radiation shields—$T = 77\,\mathrm{K}$ and $T = 4.2\,\mathrm{K}$—prevent infrared radiation from saturating the detector, and a 4 mm diameter hemispherical substrate lens (Figure 2.7) is located above the antenna to prevent substrate modes, reduce the silicon-vacuum interface reflection at normal incidence, and increase antenna directivity (discussed in Section 2.4.3 of this thesis) [66, 67, 63, 68]. A three-way reflecting periscope is affixed to an arm mounted on a rotation stage, with the center of rotation collinear with the vertical axis of the sample under test. The arm length is 33 cm from the rotation axis to the center of the first periscope mirror, and the total length of the periscope path from the sample rotation axis to the detector is 122.5 cm. Due to mechanical limitations (the walls of anechoic material and the cryostat platform legs) the arm is able to revolve from approximately $\theta_A = -20°$ to $\theta_A = 160°$, where $\theta_A = 0°$ is the intended location of the transmitted source beam. In reflectance measurements, arm angle θ_A is related to beam incidence angle by $\theta_i = (180 - \theta_A)/2$. The source is a backward wave oscillator (BWO) operated between $f = 800$ GHz and $f = 900$ GHz and linearly polarized. The electric field of the BWO is oriented 8° from parallel to the optics table, which is also the plane of incidence in the reflectance measurements described later in Section 4.3.2. This angle was separately measured by rotating a wire grid polarizer through the beam. Because the polarization is neither purely parallel nor perpendicular to the plane of incidence, a vector superposition of the Fresnel formulae for reflectance is required, and as discussed in Section 4.3.2, the extraction of material parameters can be quite sensitive to the electric field orientation. The incident BWO beam is baffled by a circular aperture 19.1 mm in diameter at the entrance of the scattering measurement experiment, 17.8 cm from the sample. The power vs. angle measurement with no sample present is defined primarily by the baffling; measured beamwidth and sidelobe spacing agree with the predicted Airy pattern from a circular aperture. Walls of radar-absorbing material are placed between the setup and the BWO source to block stray radiation. The incident beam is mechanically chopped at the circular aperture, and a lock-in amplifier is used to measure the detected signal via the electronics. Phase that is shown on the y-axis of plots in this chapter is referenced to the lock-in amplifier; constant phase is indicative that the power being detected is signal, rather than noise.

To validate the setup, a small ribbon cable with wire pitch $p = 0.5$ mm was placed in the sample position, normal to the incident beam. The first grating lobe peak should appear at $\arcsin(\lambda/p) = 43.6°$ for $f = 877$ GHz, and it was observed at 43.8°, 14.7 dB down from the peak power of the transmitted beam with no sample present (Figure 4.3). The transmitted beam maximum is at $\theta_A = 0.25°$, so the grating lobe is just 0.05° from the expected location. The arm

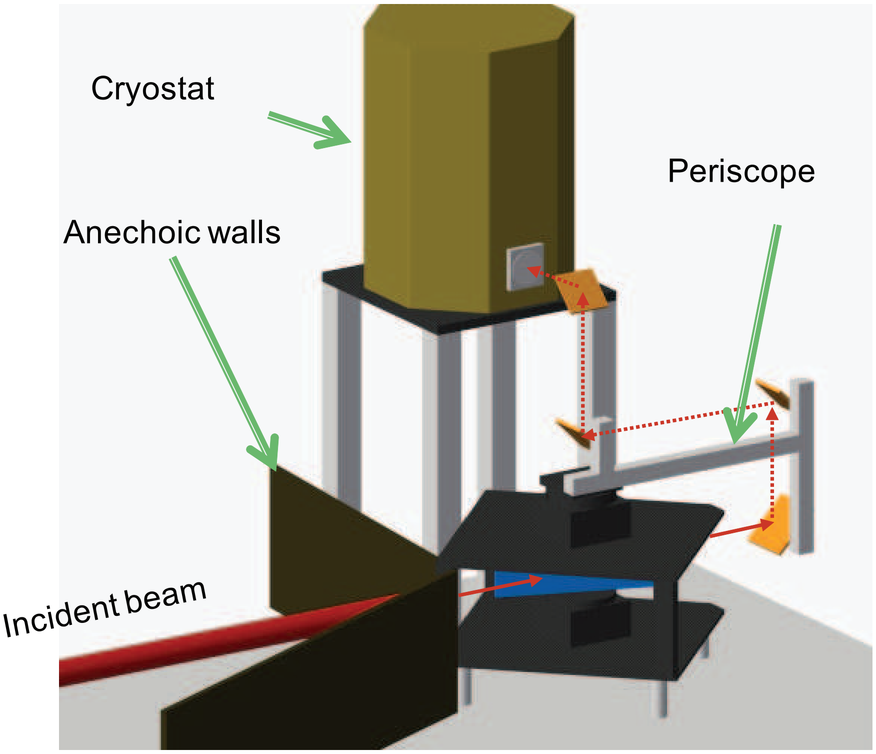

Figure 4.1: 3D rendering showing the geometry of the incident beam, baffling, rotation-arm-mounted periscope, and cryostat. The dotted line indicates a beam path that is out of the plane of the sample and BWO beam.

is operated by a stepper motor with absolute positioning accuracy of 0.01°.

4.2.2 PROCEDURE

Two experiments were performed to gather information about the EPS foam samples. First, transmission measurements for samples at normal and $\theta_i \approx 45°$ incidence angles were completed. In these measurements, the periscope arm was rotated $\theta_A = \pm 20°$ to detect any steering of the transmitted beam and/or beam broadening, deformation, or grating lobes. Second, specular reflectance from EPS foam samples was examined. Due to the large dynamic range between the transmitted beam and the specular reflected signal, the beam was attenuated by approximately 20 dB so that the transmitted beam and specular reflection could be obtained with the same lock-in amplifier sensitivity settings in a single arm sweep, for an accurate comparison of transmitted and reflected power levels. For some low-density samples, the attenuation had to be removed to accurately measure the specularly reflected beam shape, due to the extremely low level of

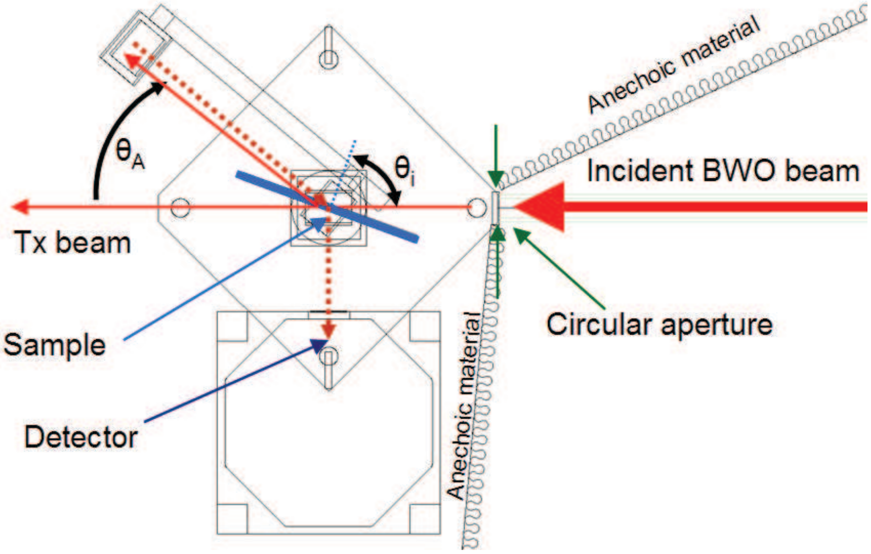

Figure 4.2: 2D top view of the scattering measurement setup. The backward-wave oscillator (BWO) beam enters the measurement setup from the right side of this view. A sample under test is drawn at an angle of approximately $\theta_i = 70°$. Arm angle is referenced from the BWO beam at $\theta_A = 0°$. For clarity, the beam paths from the sample to the bottom periscope mirror and from the top periscope mirror to the bending mirror at the arm axis of rotation are offset. The dotted line indicates a beam path that is out of the plane of the sample and BWO beam.

reflected power.

4.2.3 EPS FOAM MATERIAL PROPERTIES

Commercial EPS foam is characterized by two parameters: pre-expansion bead diameter d, and final target EPS foam density. The three commonly available pre-expansion bead diameters are: $d < 0.5\,\mathrm{mm}$; $0.5\,\mathrm{mm} < d < 0.7\,\mathrm{mm}$; and $0.7\,\mathrm{mm} < d < 1.0\,\mathrm{mm}$. The diameter distributions within each bead size category are approximately Gaussian due to the nature of the sorting process [105]. More specific bead diameters can be attained with additional sorting meshes, if desired. Final EPS foam densities between 15 g/L and 130 g/L are easily manufactured. This density is a combination of the raw polystyrene density and the density of air and blowing agent that remains in the EPS foam once the expansion process is complete. For comparison, most standard hot beverage containers are made from the smallest bead size, with a density of approximately 90 g/L. We measured four different variations of EPS foam: $d < 0.5\,\mathrm{mm}$, 35 g/L; $d < 0.5\,\mathrm{mm}$, 120 g/L; $0.5\,\mathrm{mm} < d < 0.7\,\mathrm{mm}$, 35 g/L; and $0.5\,\mathrm{mm} < d < 0.7\,\mathrm{mm}$, 54 g/L. The samples were provided

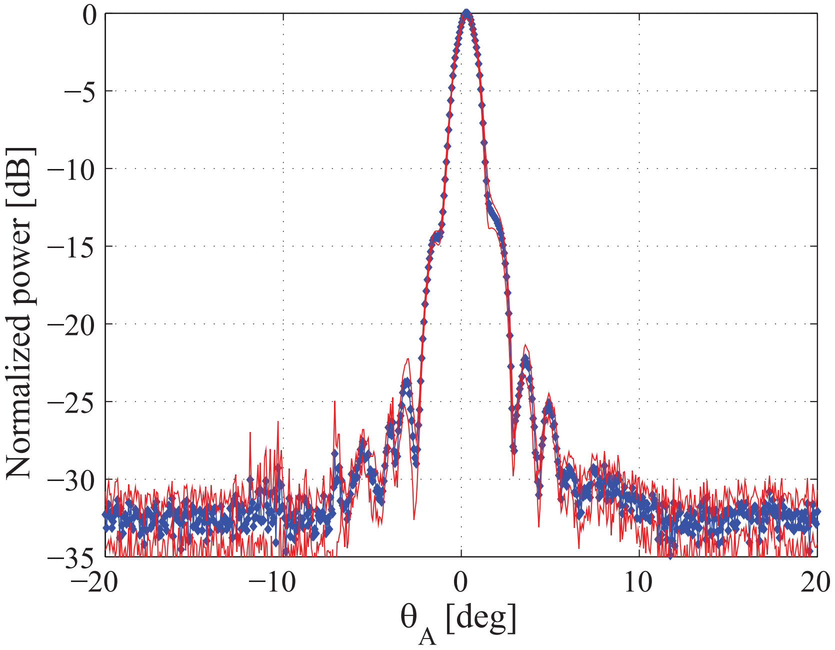

Figure 4.3: Mean of ten scans of the beam, with no sample installed, normalized to the maximum and shown in dB. The outline indicates ±1 standard deviation from the mean. The noise floor is typically 33 dB below the main beam maximum with a lock-in amplifier time constant of $\tau = 100\,\mathrm{ms}$. The full-width half-maximum (FWHM) beamwidth is approximately 1.3°, with peak beam power stability ±0.05 dB.

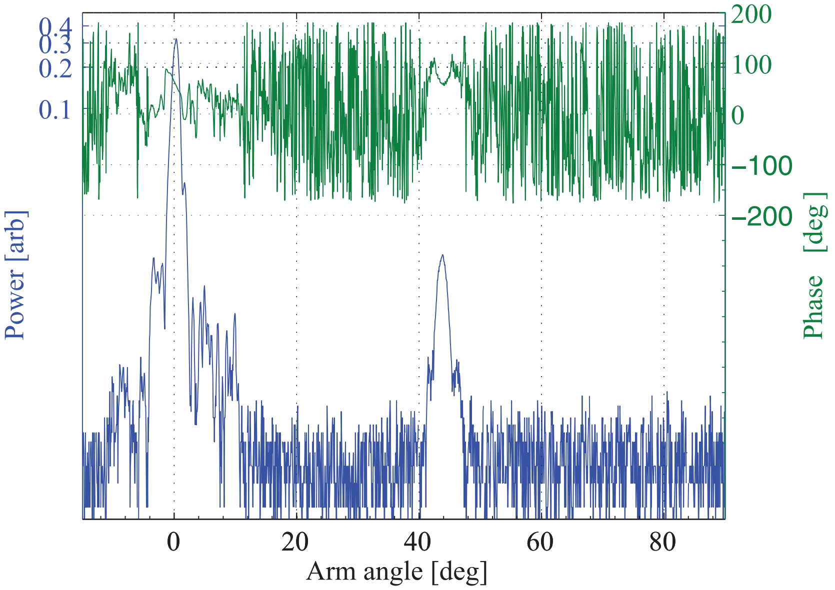

Figure 4.4: Measurement of the first grating lobe from a ribbon cable with wire spacing $p = 0.5\,\mathrm{mm}$ at a BWO frequency of $f = 877\,\mathrm{GHz}$.

in sheet format and were each 1 cm thick. Bulk polystyrene has a refractive index of $n = 1.6$ between $f = 200\,\text{GHz}$ and $f = 1\,\text{THz}$ [35] and a density of 1050 g/L, so based on EPS foam density, the "effective" refractive indices of our samples should be 1.02 (35 g/L), 1.03 (54 g/L), and 1.07 (120 g/L). In other work, measurements of three samples of polystyrene foam with densities between 30 g/L and 40 g/L produced refractive indices between 1.017 and 1.022 in the $f = (0.2\text{–}4)\,\text{THz}$ frequency range [5].

4.3 Results

4.3.1 Peak transmitted beam attenuation

The peak transmitted beam power attenuations are given in Table 4.1. In previous measurements with a Fourier-transform infrared spectrometer (FTIR), EPS foam with $0.5\,\text{mm} < d < 0.7\,\text{mm}$, and density of 54 g/L had a transmittance $T = -0.7\,\text{dB}$, and for the 35 g/L sample $T = -0.4\,\text{dB}$, all at the same frequency as in the current experiment, 877 GHz. A $d < 0.5\,\text{mm}$, 35 g/L sample had $T = -0.4\,\text{dB}$ as well, and for a 96 g/L sample of the same bead size (not available for these measurements), T was measured to be approximately $-3.5\,\text{dB}$. The FTIR data follow the same trend as the newly-acquired data. Based on the results here, with transmittance measured at two separate angles, as well as the effects found in Section 4.3.3, it is plausible that the differences in actual measured transmittance values could be due to slight misalignment of the sample in the FTIR. Additionally, we note that the SNR in the FTIR is orders of magnitude lower than the SNR utilizing the BWO and cryogenic microbolometer, and the actual FTIR data below $f = 1\,\text{THz}$ is the result of a fit due to low SNR. Thus, the trend found with the FTIR matches the trend here, in terms of bead diameter and density, but the exact attenuation values found in both experiments are subject to the specific sample, exact orientation, and other environmental variables. Excess loss in EPS foam with density above 35 g/L can be attributed to the trapping of water inside the polystyrene bead matrix during the expansion process, when high temperatures and steam are utilized. In this process, the EPS foam is cooled while steam and blowing agent still reside within the cell matrix, trapping an unknown amount of particulate water between the inner-most cells of the EPS foam sheet. The blowing agent used in the process for this EPS foam is pentane, C_5H_{12}.

The theoretical result for dielectric slab transmittance is [106]:

$$T_{slab} = |t_{slab}|^2 = \frac{(1-R)^2 + 4R\sin^2(\Psi)}{R^2 e^{-\alpha h} + e^{\alpha h} - 2R\cos(\xi + 2\Psi)}, \tag{4.1}$$

where

$$\Psi = \tan^{-1}\left(\frac{2k}{n^2+k^2}\right), \quad \xi = \frac{4\pi n h}{\lambda}, \quad \alpha = \frac{4\pi k}{\lambda}, \quad R = \left|\frac{1-\hat{n}}{1+\hat{n}}\right|^2, \quad \hat{n} = n - \jmath k, \tag{4.2}$$

and h is the slab thickness. Equation 4.1 is the exact expression that applies only to a monochromatic field and perfectly smooth dielectric slab walls. In reality, these conditions are closely approximated but never achieved, which leads to an expression in which coherent interference does not appear. In our situation, the EPS foam surface roughness of greater than the Rayleigh criterion of $\lambda/(8\cos\theta_i)$ blurs the coherent effects; additionally, the interior of the EPS foam slab is inhomogeneous compared to an ideal dielectric slab. Thus, the transmittance approximation neglecting coherence, in the limit of transparency $\left(R^2 e^{-2\alpha h} \ll 1\right)$ is:

$$T_{slab} = (1-R)^2 e^{-\alpha h} \tag{4.3}$$

Equation 4.3 can be used as a first-order approximation to the transmission and reflection, by using the material properties for bulk polystyrene and calculating an "effective" complex refractive index based on EPS foam density and loss coefficient [35]. This is the limiting case in which scattering is not considered, and even for the most dense EPS foam sample, only 1.11 dB of transmission loss is calculated at normal incidence for density-adjusted $k = 6 \times 10^{-4}$ (from bulk polystyrene measurements of k in [35]) and $n = 1.07$.

4.3.2 SPECULAR REFLECTANCE

In measurements of specular reflectance, both the front and back surfaces of the EPS foam sample were distinguished due to the finite thickness of the samples. An example of raw data is shown in

Table 4.1: Peak measured transmitted beam attenuation at $f = 877\,\text{GHz}$. The asterisk indicates a measurement where the actual loss was less than the noise or stability of the measurement.

EPS foam parameters	θ_i [deg]	attenuation [dB]	attenuation (FTIR) [dB]
$d < 0.5\,\text{mm}$, $35\,\text{g/L}$	0 45	0.24 0.64	0.4
$d < 0.5\,\text{mm}$, $120\,\text{g/L}$	0 45	2.1 5.6	—
$0.5\,\text{mm} < d < 0.7\,\text{mm}$, $35\,\text{g/L}$	0 45	0* 0.3	0.4
$0.5\,\text{mm} < d < 0.7\,\text{mm}$, $54\,\text{g/L}$	0 45	0.8 0.7	0.7

Figure 4.7. As expected, the received power reflected from the front surface of the EPS foam is slightly greater than that received from the back surface reflection by approximately 0.8 dB. The refractive index of the sample can be calculated based on the Fresnel equations and measured reflectance values (R),

$$\sqrt{R_\parallel} = r_\parallel = \frac{\cos\theta_t - n\cos\theta_i}{\cos\theta_t + n\cos\theta_i} \tag{4.4}$$

and

$$\sqrt{R_\perp} = r_\perp = \frac{\cos\theta_i - n\cos\theta_t}{\cos\theta_i + n\cos\theta_t}. \tag{4.5}$$

The reflectance results are compiled in Table 4.2. It is important to be aware that the accuracy of the polarization of the incident beam and θ_i are key in extracting n from measured reflectance, in the limit of ($n \longrightarrow 1$). The angle θ_i is known extremely accurately due to measurement of the angle between the transmitted and specular reflected beams, from the stepper motor controlling the arm. The polarization of the incident field was measured and found to be at 8° from parallel to the plane of incidence, ±2°. This corresponds to a worst-case uncertainty in n of ±0.02. Solving the Snell and Fresnel equations to provide reflectance as a function of incidence angle and polarization is a useful exercise, in order to understand the dependence of R on the measurement geometry. Graphically, this is shown in Figure 4.5 and Figure 4.6, and essentially shows two things. First, that as $n \longrightarrow 1$, R becomes increasingly hard to measure accurately. Second, polarization plays a significant role in the exact value of R when near the Brewster angle.

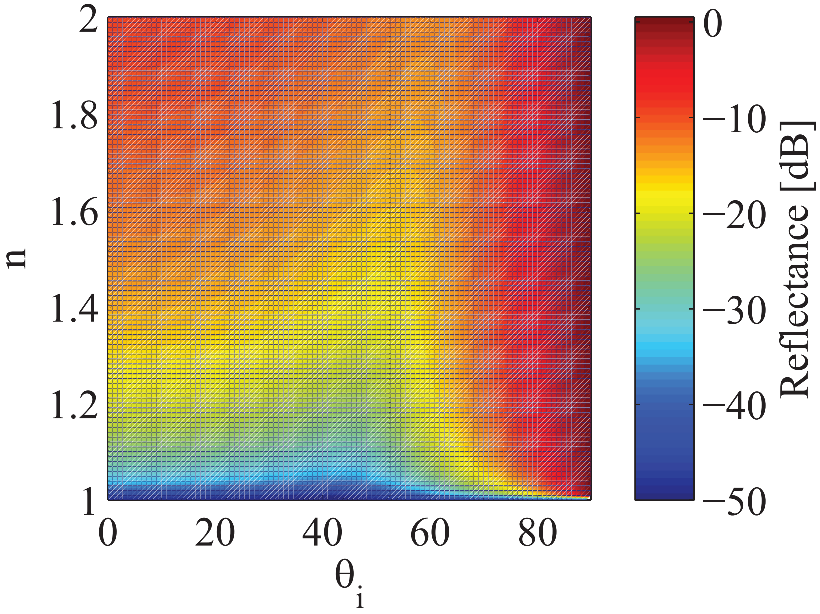

Figure 4.5: Calculated reflectance as a function of refractive index and incidence angle.

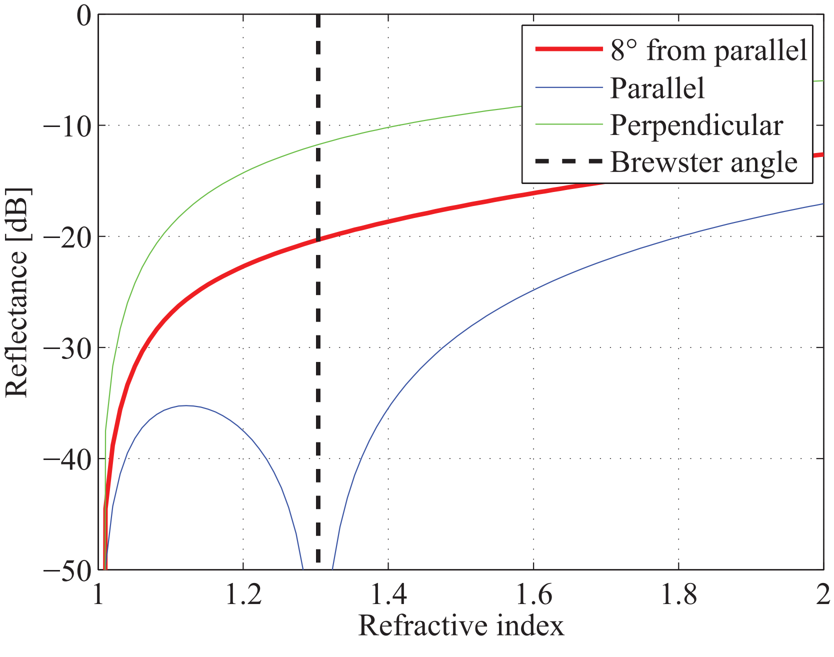

Figure 4.6: Calculated reflectance as a function of refractive index, for $\theta_i = 52.5°$. This (the solid red line) is basically a vertical cut from Figure 4.5. Reflectance is shown for parallel and perpendicular polarization, as well as the case of the BWO in the experimental setup: 8° from parallel.

The resulting extracted refractive indices from measured data in Table 4.2 are as follows: for the 35 g/L, $0.5\,\text{mm} < d < 0.7\,\text{mm}$ sample, $n = 1.035$, similar to the results with the 35 g/L polystyrene foam in [5]. For the 54 g/L sample, $n = 1.067$, and for the 120 g/L sample with the smallest beads, $n = 1.15$. All values are higher than expected, but are explained; due to the nature of the molding process, there exists a thin layer of expanded polystyrene that has a refractive index closer to the bulk value ($n = 1.6$) than the average that is due simply to density. It is known that the refractive index of expanded polystyrene beads varies as a function of bead radius [107], with $n = 1.6$ being the maximum value, naturally found at the outermost "shell" of the bead. In the molding process, this layer of shells ends up aligned at the edge of the molded structure, that is, against the mold wall. Adding to this is the rms roughness of the EPS foam surface, typically several hundred micrometers. Projected at the incidence angles at which the specular reflectance was measured, the thickness of the outer shell layer with $n = 1.6$ is comparable to a wavelength or more. Thus the reflectance from the EPS foam surface at these incidence angles is higher, being weighted towards that of a material with $n = 1.6$ to a greater extent than if only examining the density-based effective refractive index of expanded polystyrene beads.

Table 4.2: Specular reflectances. For each EPS foam measured, the incidence angle is given, and the peak of the measured specular reflectance relative to the beam transmitted through the EPS foam. Also provided are the inferred index from the measurement and the expected index based on equivalent density.

EPS foam parameters	θ_i [deg]	reflectance [dB]	inferred index	expected effective index
$d < 0.5\,\text{mm}$, 120 g/L	52.5	−23.5	1.151	1.07
$0.5\,\text{mm} < d < 0.7\,\text{mm}$, 35 g/L	57.1	−31.1	1.035	1.02
$0.5\,\text{mm} < d < 0.7\,\text{mm}$, 54 g/L	57.5	−26.2	1.067	1.03

4.3.3 EPS FOAM FORWARD SCATTERING EFFECTS

An interesting result was observed for most EPS foam samples measured while acquiring data for Sections 4.3.1 and 4.3.2. In addition to the slight attenuation of the transmitted beam,

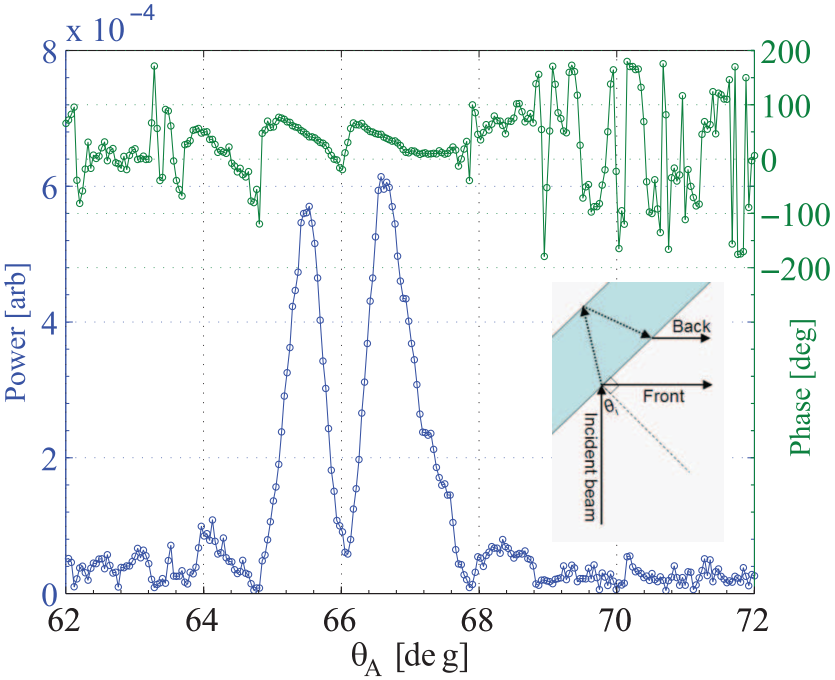

Figure 4.7: Example of specular reflectance measurement, for $0.5\,\mathrm{mm} < d < 0.7\,\mathrm{mm}$, 54 g/L EPS foam, and $\theta_i = 57.5°$. Arm angle θ_A is related to BWO beam incidence angle by $\theta_i = (180 - \theta_A)/2$. Reflection peaks are separated by 1°, corresponding to the reflections due to the front and back surfaces of the EPS foam thickness projected by the incidence angle (1.89 cm), viewed by a detector at the end of the periscope arm at θ_A. A schematic of the reflectance measurement geometry from an EPS foam sample is inset.

coherent forward scattering was found. Essentially, the EPS foam exhibits grating lobes with peaks typically greater than those of the specular reflections, at seemingly arbitrary locations. The locations of the lobes are based on the quasi-periodicity of the EPS foam, which is at some level a random medium, but is essentially comprised of a matrix of spheres expanded within a mold. In the ideal case of all spheres being identically sized, the spheres become rhombic dodecahedra—the most efficient use of space in the classic sphere-packing problem. Although neither the initial sphere diameters nor the final expanded bead sizes are uniform (the condition required for an analytic close-packing solution), it is clear that the EPS foam is periodic enough at certain positions and incidence angles to create grating lobes. Data from two EPS foam samples are shown in Figure 4.8. A 120 g/L, $d < 0.5\,\mathrm{mm}$ sample at $\theta_i \approx 45°$ is on the left; due to this particular EPS foam being relatively dense, this example demonstrates two effects simultaneously: extinction of the main beam and the forward-scattering grating lobes. Extinction of the main beam is due to scattering, absorption, and reflection of the incident beam out of the measurement region. The extinction relative to the no-sample beam is 5.6 dB. On the right is a 54 g/L, $0.5\,\mathrm{mm} < d < 0.7\,\mathrm{mm}$ sample at normal incidence. The scattering features are mostly symmetric.

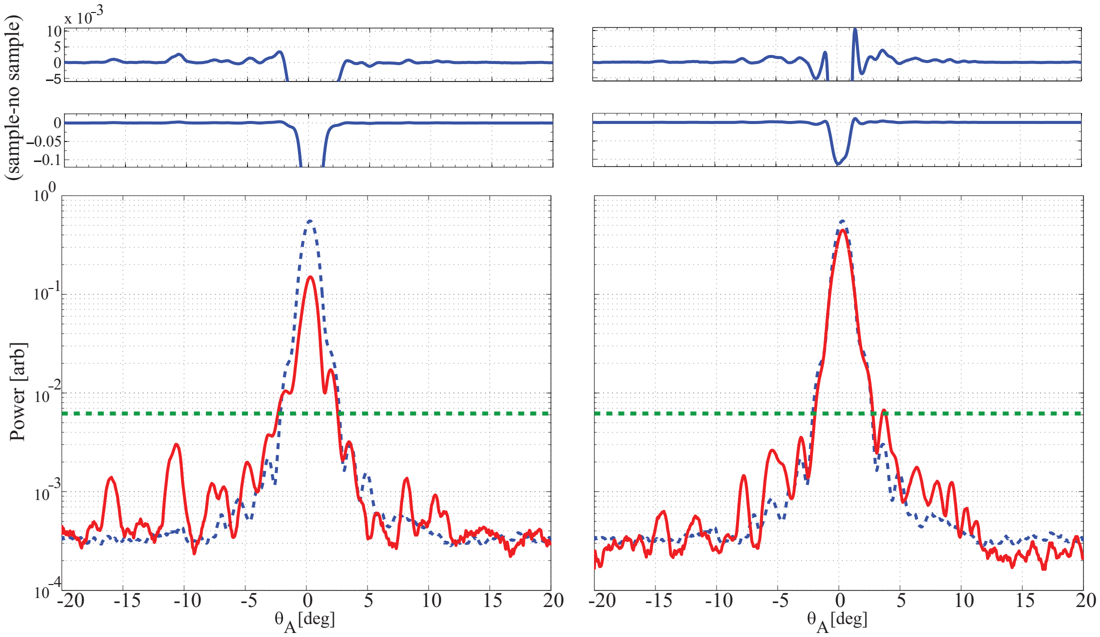

Figure 4.8: (bottom left) Solid line: transmitted beam, through a $d < 0.5\,\mathrm{mm}$, 120 g/L EPS foam sample, at $\theta_i = 45°$. Dashed line: beam with no sample (ensemble mean, same as Figure 4.3). The primary forward scattering features are seen at $-16°$ and $-10.5°$. The main beam is attenuated due to a combination of reflection and true absorption. The thick dashed horizontal line indicates the "main beam" cutoff level, for purposes of calculating scattered radiation out of the main beam (Table 4.3). (top left) Difference between measurement of EPS foam (sample) and power-vs.-angle pattern with no EPS foam (no sample). Note that two linear scales are required to capture the dynamic range of the difference. (right) $0.5\,\mathrm{mm} < d < 0.7\,\mathrm{mm}$, 54 g/L EPS foam sample measured at $\theta_i = 0°$.

Table 4.3 summarizes the percentages of scattered power found outside the main beam, in the plane of the measurement, for all EPS foam samples measured. Because the experimental setup does not allow two-dimensional measurements, we make the assumption that the incident beam is circular, as expected from the pattern given by a circular aperture, and also that the scattering features—grating lobes—are also circular. We note that the FWHMs of the scattering features are approximately the same as of the main beam, so percentages in Table 4.3 are calculated by subtracting the measured pattern with the sample out from the measured pattern with the sample in, and dividing the difference by the power summed in the main beam (denoted by the horizontal dashed line in Figure 4.8). The main beam is defined by the crossover point between the sample-in and sample-out power vs. angle measurements. In this situation, this crossover point is a more convenient definition of the "main beam" than the typical FWHM definition.

Table 4.3: EPS foam sample description, BWO beam incidence angle and percentage of power scattered relative to the BWO beam with no sample, and percentage of power scattered relative to the measured transmitted beam. The thick dashed horizontal line in Figure 4.8 represents the cutoff point for the "main beam," both for the actual BWO pattern as well as the pattern measured with an EPS foam sample in place.

EPS foam parameters	θ_i [deg]	Power scattered relative to no-sample beam [%]	Power scattered relative to transmitted (sample) beam [%]
$d < 0.5\,\mathrm{mm}$, $35\,\mathrm{g/L}$	0	0.009	0.0015
	45	0.009	0.0011
$d < 0.5\,\mathrm{mm}$, $120\,\mathrm{g/L}$	0	1.02	1.72
	45	1.09	4.07
$0.5\,\mathrm{mm} < d < 0.7\,\mathrm{mm}$, $35\,\mathrm{g/L}$	0	0.035	0.035
	45	0.026	0.033
$0.5\,\mathrm{mm} < d < 0.7\,\mathrm{mm}$, $54\,\mathrm{g/L}$	0	0.98	1.21
	45	1.12	1.25

Though not shown graphically here, we found that nearly all forward scattered radiation lies within ±15° of the transmitted beam. As a common "transparent" structural material in the millimeter-wave/terahertz frequency range, this is of great use to know. Additionally, the magnitude of the scattered lobes is on the order of 1 % for the most dense EPS foam, and decreases to 0.1 % for the least dense samples. It is necessary to explicitly note that our measurements were performed in a single plane, and that generalization to the full hemisphere beyond the EPS foam plane requires an explanation. It is possible that in every measurement, either the sample or the periscope was slightly misaligned such that the axis of strong scattering (the plane of the incident beam) was not properly sampled. However, eight independent measurements of four samples were made without extensive care to ensure exact angular positioning of the sample, and because we can clearly see that scattered power is proportional to density, it is highly likely that the conclusions drawn from these 1D measurements are extensible to the half space. Furthermore, the location and angular orientation of the EPS foam sample is no more accurate than the feature sizes of the sample itself, implying that the orientation and position of the semi-infinite matrix of expanded polystyrene beads is essentially random, relative to the incident beam.

4.4 Discussion

In Table 4.4, we have attempted to make a budget for radiation transmitted through EPS foam, separating the total incident power into reflected, transmitted, and scattered components. For reflected power, it is required to examine the inhomogeneity of the EPS foam, specifically the first millimeter of the slab surface, to account for the refractive index being greater than expected due simply to density alone. The measurements of transmitted beam attenuation indicate greater attenuation than due to simply absorption and reflection from a slab of reduced-density polystyrene. Forward scattering at the 0.1–2.0 % level is observed at normal incidence, and in combination with the reflected power, the measured attenuated power is not completely accounted for. The difference is attributed to one or both of two reasons: first, it is likely, especially in the more dense samples, that water is trapped inside the matrix of EPS beads; second, it is possible that the k of bulk polystyrene measured in [35] is slightly different than that of the polystyrene used in fabrication of the EPS beads.

Table 4.4: EPS foam budget.

EPS foam parameters	% attenuated Table 4.1	% reflected[†] Table 4.2	% scattered Table 4.3	% missing %A-(%R+%S)
$d < 0.5\,\mathrm{mm}$, $35\,\mathrm{g/L}$	5.38	—	0.1	—
$d < 0.5\,\mathrm{mm}$, $120\,\mathrm{g/L}$	38.34	23.2	1.72	13.42
$0.5\,\mathrm{mm} < d < 0.7\,\mathrm{mm}$, $35\,\mathrm{g/L}$	5 ± 1[‡]	6.1	0.035	-1.14 ± 1
$0.5\,\mathrm{mm} < d < 0.7\,\mathrm{mm}$, $54\,\mathrm{g/L}$	16.82	11.0	1.21	4.61

[†] Percent reflected at normal incidence is calculated from the extracted n from reflectance measurements in Table 4.2.

[‡] Due to the extremely low attenuation of this sample, uncertainty is increased.

In conclusion, a basic experimental setup was described for measurement of angular distribution of power in one plane. Measurement of coherent forward scattering—grating lobes—from EPS foam was observed for the first time, and the scattered power in the plane of the measurement was found to be between 0.01 % and 1.1 % dependent on EPS foam density. We found that nearly all forward scattered radiation lies within ±15° of the transmitted beam. As a common “transparent” structural material in the millimeter-wave/terahertz frequency range, this is of great practical knowledge. Refractive index was determined by measurement of specular reflectance and found to agree with other work in the 35 g/L EPS foam sample ($n = 1.035$), but was calculated to be $n = (1.14\text{–}1.15)$ for the highest density EPS foam sample, rather than the 1.06–1.07 predicted by polystyrene density alone. This is attributed to the non-uniform density profile of the expanded polystyrene beads, affecting the apparent refractive index at incidence angles close to glancing.

CHAPTER 5

W-BAND POLARIZER & ISOLATOR

Beware of any enterprise that requires new clothes.

— Henry David Thoreau

CONTENTS

5.1 INTRODUCTION

Since the late 1980s, both passive and active millimeter-wave and terahertz imaging have gained attention for applications such as concealed weapons detection (CWD) [62], remote sensing [108], inclement-weather navigation, large-scale fire detection, material measurements, spectroscopy, radio astronomy, and plasma diagnostics [99, pp. 342–536]. Many of the systems contain various passive quasi-optical components described in [99, pp. 71–229], such as lens systems with Gaussian beams, dielectric lenses, anti-reflection coatings, metallic lenses, reflective focusing elements, delay lines, polarization processing, wave plates, absorbers and calibration loads, and a variety of frequency-selective surfaces and gratings. This chapter describes a low-loss, high-scan-angle, low-cost W-band linear-to-circular polarizer (quarter-wave plate) designed for an active CWD system [23].

Active millimeter-wave/terahertz imaging systems are essentially radar, and can therefore be classified as either monostatic or bistatic, depending whether or not the transmit and receive arrays are co-located. All monostatic radars require a diplexer of some sort to separate the transmit and receive beams. These can be made from non-reciprocal materials, such as the Faraday rotator in [109]. When combined with a polarization-sensitive mirror, the linear polarization-rotation approach works well for reducing the imaging system footprint [33]. An alternate approach, which we have taken with this system, is to exploit the isolation properties of right-hand and left-hand circularly polarized waves.

A simplified block diagram of the system is shown in Figure 5.1. The target is illuminated by a $400\,\lambda_0$-long 1D antenna phased array ($f_0 = 95\,\text{GHz}$). The linearly-polarized (LP) illumination beam is focused by a cylindrical lens, reflected from a polarizing beamsplitter and circularly polarized (CP) by the $\lambda/4$ plate; the resulting CP wave focuses to a linear image of the transmit array in the target plane, which is scanned over the target area by the video-rate scanning mirror. The resulting reflected radiation is orthogonally circularly polarized, and thus upon passing through the $\lambda/4$ plate becomes orthogonally linearly polarized to the illuminating wave. The wave then passes through the polarizing beam splitter and is sampled by a 1×128 room-temperature antenna-coupled microbolometer array [22]. Therefore, in this configuration—a common quasi-optical setup in active imagers—the $\lambda/4$ plate is critical not only to produce circular polarization, but also to ensure isolation between the input and image-forming waves. The 2:1 field of view required by the system, explained in [23], is $0.9\,\mathrm{m} \times 1.8\,\mathrm{m}$ at a distance from the entrance aperture of 1.5 m. This corresponds to an opening angle of approximately $\pm 31°$.

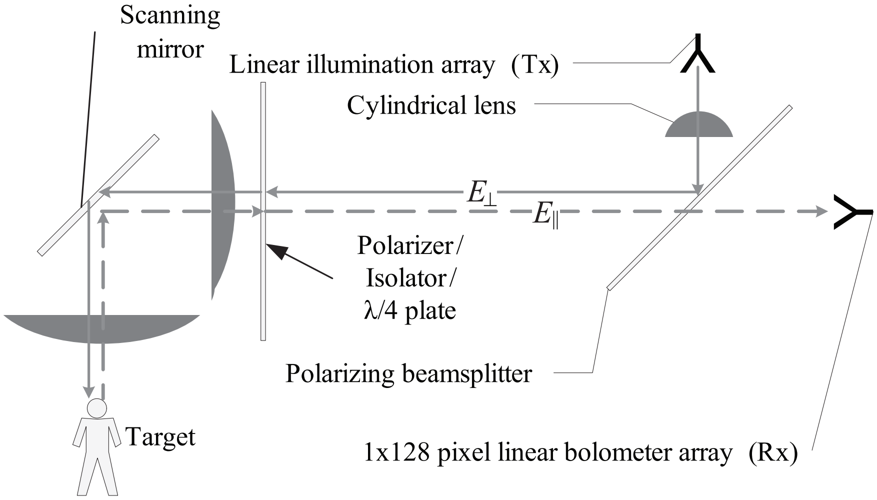

Figure 5.1: Top view of simplified block diagram for the active CWD system. Shown is a cross-section; the 1D arrays, lenses, mirror, and polarizing beamsplitter are perpendicular to the plane of the paper. To the right of the $\lambda/4$ plate, $E_{||}$ and $E_{\perp}$ are the two orthogonal linear polarizations, one parallel and one perpendicular to the plane of the paper.

A number of linear-to-circular polarizers have been demonstrated in the literature: single- and multiple-layer dipole arrays [110, 111, 112], layered dielectric frequency-selective surfaces [113, 114], metallic meander-lines [115, 116, 117], and finally, designs using combinations of capacitive and inductive grids [118, 119]. The last was chosen due to the advantages that it is quick to simulate, simple to fabricate (especially given the large aperture required), and performs reasonably well for this application.

5.2 Design and simulation

This section describes the design of a unit cell of the polarizer, utilizing a combination of method-of-moments (MoM) and transmission-line analysis.

5.2.1 Basic principle of operation

It is well known that metal strips present an equivalent inductance to an incoming co-polarized wave, while perpendicular metal strips present a capacitance to an incoming plane wave: these inductances and capacitances can be calculated from the quasi-static approximation [120], and measurements have been shown to agree very well with calculation.

In order to achieve circular polarization, a 90° phase shift is required between two equal-magnitude orthogonal vector components of the electric field. This usually requires several grids with a more complex unit cell. The unit cell in this work is shown in Figure 5.2 for two orthogonal electric field vector components. For normal incidence and an infinite 2D grid surface in the x-y plane, symmetry defines electric and magnetic wall boundary conditions extending in the $\pm z$ direction. The magnetic walls are the vertical sides of the unit cell and the electric walls are the horizontal sides. This simplification of the geometry allows the polarizer design to be reduced to the design of a single unit cell, decreasing simulation complexity and time. A number of methods can be used to this end, the discussion of which is not the topic of this chapter. The design tool used for this work was an available subdomain Galerkin method-of-moments (MoM) code, described in detail in [121].

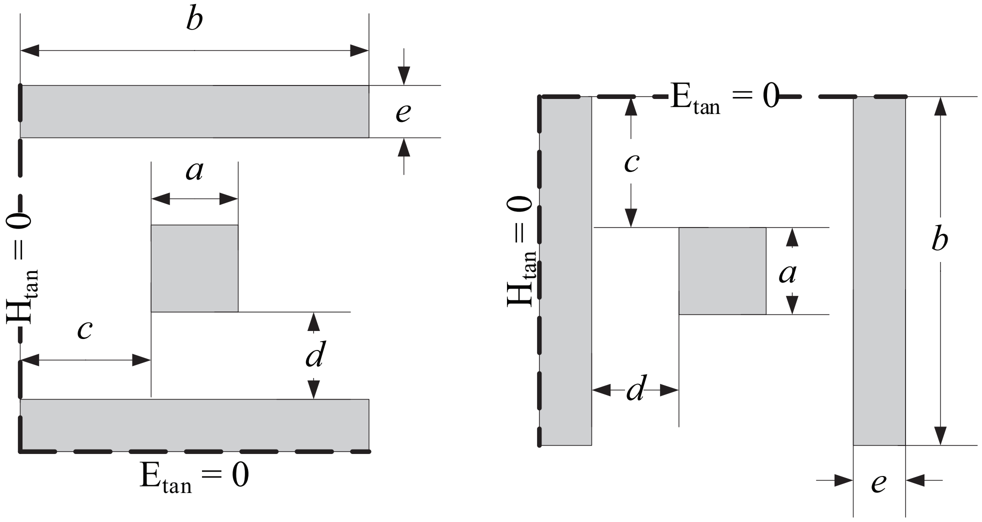

Figure 5.2: (left) Parametrization of polarizer unit cell for E_C vector, with dimensions $a = 0.630\,\text{mm}$, $b = 1.263\,\text{mm}$, $c = 0.500\,\text{mm}$, $d = 0.525\,\text{mm}$, and $e = 0.210\,\text{mm}$. Electric and magnetic walls are indicated by $E_{\text{tan}} = 0$ and $H_{\text{tan}} = 0$, respectively. (right) Unit cell for E_L vector.

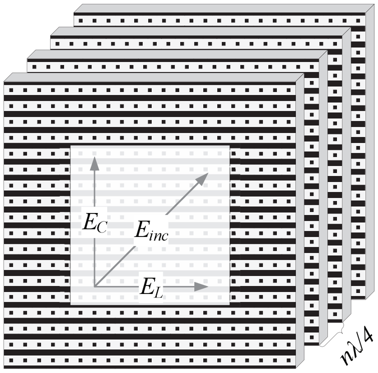

Figure 5.3: Layering of sheets and superpose of electric field vector orientation—Incident electric field E_{inc} is oriented at 45° from the metal strips and decomposed into two orthogonal vectors (E_L and E_C). The spacing between sheets is $n\lambda/4$, with n odd.

Definitions for angular quantities and S-parameter notation are as follows:

- S_{21}^{C}: The transmission coefficient of the E_C component through the polarizer;
- S_{21}^{L}: Similarly, the transmission coefficient of the E_L component through the polarizer;
- ϕ: Phase difference between S_{21}^{C} and S_{21}^{L};
- θ: Off-normal angle of incidence;
- ψ: Polarizer rotation about optical axis z.

5.2.2 SIMULATION

After completion of the MoM simulations for both unit cells, S-parameters were extracted for both polarizations, and imported into Agilent Advanced Design System as S-parameter blocks. Four identical grids are cascaded with sections of $\lambda_0/4$-long sections of air between them, as depicted in Figure 5.3. The equivalent transmission line model for the two polarizations is shown in Figure 5.4; the susceptances, $\jmath B_L$ and $\jmath B_C$, are due to the following: the electric field vector oriented along the strips, E_L, is presented with an inductance due to the strips and a capacitance due to the squares; the electric field vector perpendicular to the strips, E_C, is presented with capacitances due to both the strips and squares, and capacitances due to the strips alone. The metallic grids are printed on a substrate with electrical thickness less than $\lambda_0/60$;

therefore the substrate is ignored in simulation. A standard S-parameter simulation is completed between $f = (90\text{–}100)$ GHz for both orthogonal components of the electric field. Optimization was performed for equal magnitude between S_{21}^{C} and S_{21}^{L}, and $\phi = 90^\circ$. The dimensions of the unit cells were varied in the MoM code to adjust the capacitance and inductance empirically until circular polarization was reached at the center frequency. Comparison of simulation and measurement of the two-port S-parameters for $\jmath B_C$ is shown in Section 5.4.2.

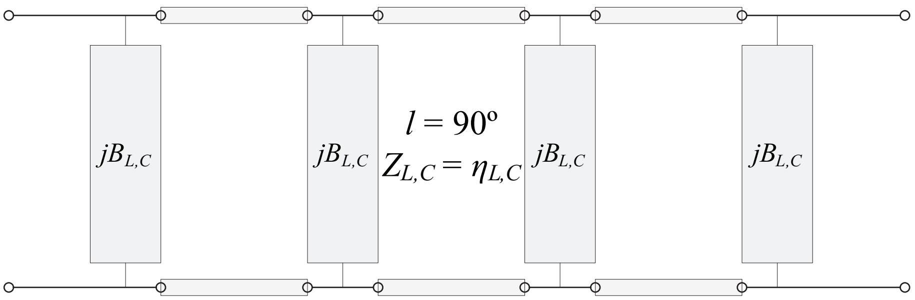

Figure 5.4: Equivalent transmission-line circuit model for E_L and E_C polarizations. The susceptance blocks for each polarization are imported into a transmission-line simulation from the MoM simulation.

Since the unit cell has a rectangular transverse cross-section, the impedances of the transmission lines used in the simulation are $\eta_L = \eta_0 b/(2e + 2d + a) = \eta_0 b/A$ and $\eta_C = \eta_0 A/b$, where b and A are dimensions of the unit cell between electric and magnetic walls, respectively, and η_0 is the impedance of free space [122].

5.3 FABRICATION

A DuPont Pyralux AP8515RA polyimide substrate with thickness $h = 25.4\,\mu\text{m}$ and Cu thickness $t = 18\,\mu\text{m}$ is used; it is electrically thin enough to be ignored, and the refractive index of the substrate is $n = 1.79$. The sheets are fabricated with a standard commercial wet-etch process; each of the four grids is 53.3 cm in diameter. Three sheets of rigid, low-density, $3\lambda/4$-thick, low-n, low-$\tan\delta$ Cuming C-Stock RH-5 (complex refractive index of $\hat{n} = 1.04 - \jmath 0.0002$) foam were sandwiched between the four polarizer sheets, while an extra foam layer was added behind the last polarizer sheet to provide additional rigidity and planarity. The completed polarizer is supported by an aluminum frame, as shown in Figure 5.5.

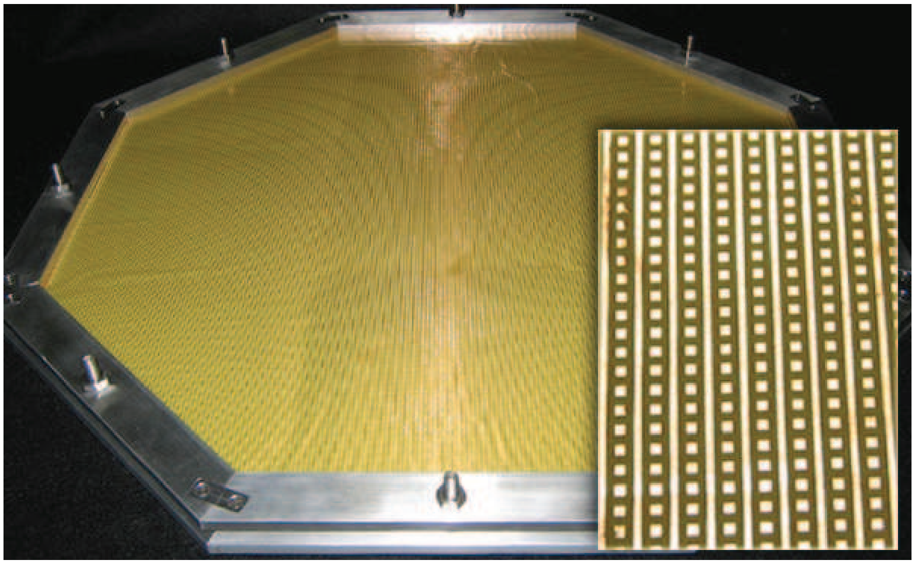

Figure 5.5: Photograph of fabricated and assembled polarizer with octagonal aluminum frame. The aperture is approximately 53 cm in diameter. Inset: a magnification of the photograph to show the pattern detail.

A 53 cm diameter clear aperture is required due to the optics specifications of the imaging system. The corresponding dielectric lenses, mirrors, polarizing beamsplitters, and transmit/receive modules in the system as shown in Figure 5.1 have apertures of similar sizes.

5.4 Testing and Performance

This section details the two testing methods used to measure the performance of the polarizer, and provides comparison between measurement and simulation.

5.4.1 Insertion loss and isolation

A dual-pass reflection power measurement was performed on sample of the completed polarizer to measure polarization rotation and isolation. Due to the physical size of the completed polarizer for installation in the imaging system, a small 10 cm diameter sample was utilized for testing, with an acrylic frame in order to minimize reflections. A Gunn diode oscillator tuned to $f = 95\,\text{GHz}$ feeds a standard-gain horn antenna that transmits a wave at the polarizer backed by a mirror. The incidence angle was set slightly off-normal ($\theta \approx 5^\circ$) to allow measurement of the reflected power. A power meter attached to an identical horn antenna was placed close to the source at the corresponding angle slightly off-normal to measure the reflected power. The two horns are cross-polarized, and the polarizer is rotated 180° about the optical axis on a rotation stage with a 45 mm clear aperture to the polarizer. Standard rf absorber was cut to form the aperture and eliminate stray reflections from the polarizer frame. The measured power as a function of rotation angle is shown in Figure 5.6 and compared to the theoretical $\sin^2(2\psi)$. The measurement is normalized with respect to the received power without the polarizer in the optical path. The measured single-pass insertion loss was 0.3 dB, and the isolation between the two polarizations was 38 dB.

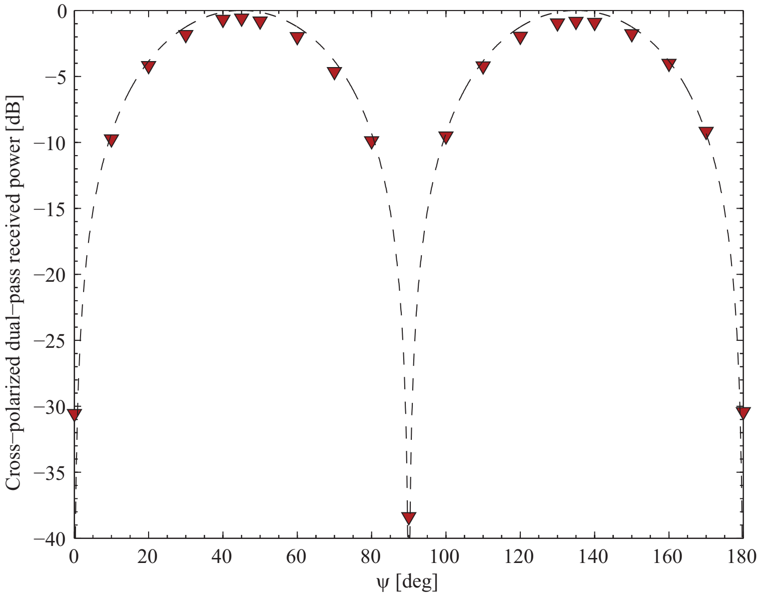

Figure 5.6: Measured cross-polarized received power after two passes through the polarizer, as a function of polarizer rotation angle ψ about the optical axis z. Single-pass insertion loss is 0.3 dB, and polarization isolation is 38 dB. Measured data are denoted by $\triangledown$, while the theoretical $\sin^2(2\psi)$ is represented by a dashed line. Measured data are normalized to the power received without the polarizer in the optical path.

5.4.2 Gaussian beam measurement

An HP 8510C network analyzer is configured with the 85105A millimeter-wave test set and W85104A W-band extension heads. The heads are attached to short W-band waveguide sections, followed by corrugated conical horn antennas with beam waist $w_0 = 7.1\,\mathrm{mm}$ at $f = 95\,\mathrm{GHz}$. Bi-convex dielectric lenses with focal depth $d = 15.2\,\mathrm{cm}$ and $n = 1.76$ were added to form a co-polarized Gaussian beam measurement system. A response-isolation calibration for S_{21} was performed in the range of $f = (90\text{–}100)\,\mathrm{GHz}$, and the optics optimized based on the desired beam radius at the polarizer measurement plane. The system is a standard Gaussian beam configuration, such as in [123, 99]. A translation stage along the optical axis z and a rotation stage for ψ and θ support the polarizer sample. A separate translation stage without ψ rotation supports a single sheet of the fabricated pattern for measurement comparison with the MoM results.

An initial measurement set was taken, and standing waves was found to dominate the signal. Standing waves exist in the system due to two main reasons: lack of anti-reflection coatings on all components, and polarization-dependent reflections. Two standing waves are noticed—one between the apertures of the scalar feeds, and the second between the lenses and polarizer. The rf absorber applied around the aperture edges of the horns reduces the amplitude of the lower-frequency standing wave. An attempt to eliminate the second standing wave was made by performing another measurement set with the polarizer sample rotated to a slight off-normal angle $\theta = 5°$, which reduced the second standing wave slightly. The remaining standing waves were eliminated by smoothing the data with a moving-average algorithm based on the period of the standing waves.

Figure 5.7 shows the simulation results for a single grid in the E_C polarization compared to measured data. It should be noted that the absolute value of the phase is not relevant, but rather the slope of the phase as a function of frequency. The phase of the measured data is shifted slightly to allow easy comparison of the two slopes. The measured data closely match the simulation, with only the transmission loss being slightly higher than simulated.

In Figure 5.8, $|S_{21}|$ through the capacitive and inductive orientations of the polarizer is shown. Ideally, the polarizer would have good off-axis performance, but due to the layered nature of this type of design, it is known that performance suffers at large angles. However, it is noted that the magnitude of the electric field for the two orientations remains constant (and nearly equal) up to $\theta = 25°$. Figure 5.8 also shows the phase difference ϕ between the transmission coefficients

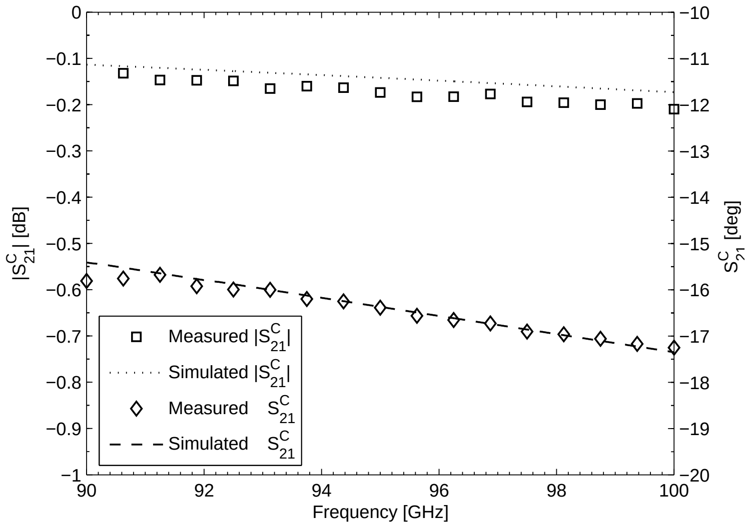

Figure 5.7: Simulated S^C_{21} compared with measured magnitude (□) and phase (◇) of the transmission coefficient for a single sheet of the polarizer. Measured phase was shifted by several degrees to agree with simulation, due to absolute phase not being available in measurement.

S^C_{21} and S^L_{21} of the electric field, as a function of off-normal angle of incidence. For $\theta < 10°$, ϕ remains above 80°.

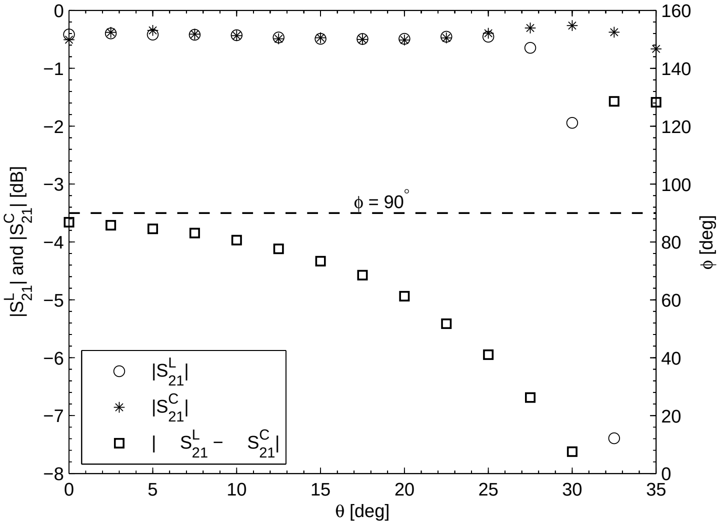

Figure 5.8: Measured magnitude of S^C_{21} (∘) and S^L_{21} (∗) as a function of off-normal rotation angle θ. While S^C_{21} stays relatively flat throughout the θ rotation, S^L_{21} rapidly decreases after $\theta = 25°$. Also shown is the phase difference ϕ between S^C_{21} and S^L_{21} as a function of θ, represented by □. Ideal phase difference $\phi = 90°$ is shown by the dashed line.

Figure 5.9 shows the total co-polarized transmission coefficient as a function of polarizer rotation angle ψ at five frequencies in the range $f = (93.5\text{–}96.5)$ GHz. The polarizer is designed to produce circular polarization when rotated so the metal strips are at $\psi = 45°$ relative to the direction of polarization of an incident electric field, i.e., any linearly-polarized antenna in the circularly-polarized field will exhibit 3 dB loss. At 0° and 90° the co-polarized transmission loss is ideally 0 dB. Figure 5.9 shows that the $\lambda/4$ plate performs as expected over a 5 % bandwidth around 95 GHz, the frequency regime where the IMPATT source utilized by the system is centered.

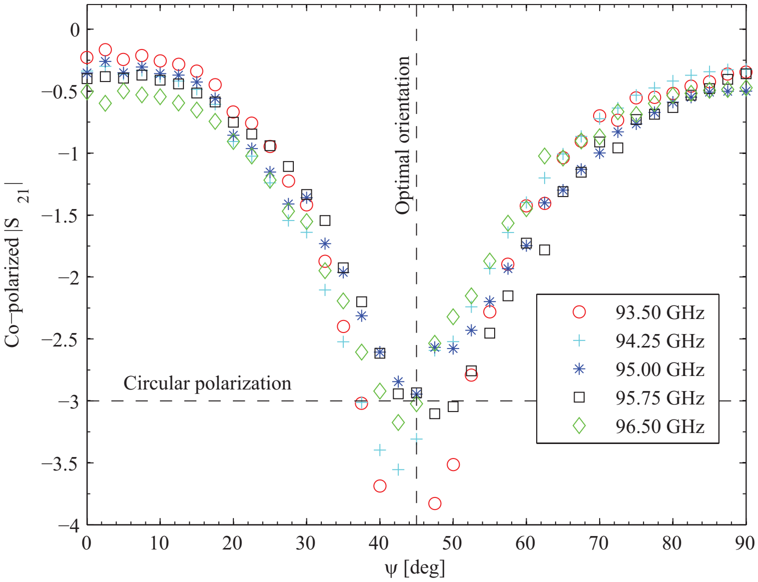

Figure 5.9: Total measured transmission coefficient through the polarizer as a function of polarizer rotation angle ψ for $f = (93.5\text{–}96.5)$ GHz in 750 MHz steps. $\psi = 0°$ and $\psi = 90°$ correspond to the E_L and E_C orientations, respectively.

5.4.3 Axial ratio calculation

Usually the axial ratio is defined as the ellipticity of the polarization ellipse, which is measured by rotating a linearly-polarized horn in a circularly-polarized field and recording the received electric field amplitude. Because it is not possible to rotate one of the horns in the Gaussian beam test, due to the size of the W85104A W-band extension heads, the phase-amplitude method is used for calculation of the axial ratio. In this method, phase information compensates for antenna rotation. The axial ratio is computed by

$$AR = \left| \frac{\xi + 1}{\xi - 1} \right|, \tag{5.1}$$

with

$$\xi = \sqrt{\frac{1 + a^2 + 2a \sin \phi}{1 + a^2 - 2a \sin \phi}}, \tag{5.2}$$

where a and ϕ are the absolute value and angle of the ratio between two orthogonal components of the electric field, i.e., $E_0^1 / E_0^2 = a \exp(j\phi)$. E_0^1 and E_0^2 should be measured simultaneously with a dual-linear polarized receive antenna for the above method to be exact. To check the validity of the approach, three measurement sets of orthogonal linear polarizations were taken, and the magnitude difference and relative phase between the measurement sets varied less than 1.5 %. This implies that the axial ratio calculation obtained from separate linear polarization measurements can be trusted.

In the Gaussian beam measurement using S_{21}^L and S_{21}^C as the orthogonal component measurements in the above formulas, an axial ratio of 0.23 dB is calculated for normal incidence. As the angle of incidence is changed, the relative magnitudes of S_{21}^L and S_{21}^C remain similar up to $\theta = 25°$ (Figure 5.8), but ϕ changes rapidly. Therefore, an axial ratio below 1 dB is maintained for angles of incidence $\theta < 17.5°$, and remains below 3 dB up to $\theta = 22.5°$.

5.5 DISCUSSION

The concealed weapons detection system described in Section 5.1 is limited by its signal to noise ratio, due to both the lack of transmitted power in this frequency band and decreased sensitivity of room-temperature bolometers. Therefore, it is essential to minimize insertion loss of all components. The (0.3–0.5) dB loss of the polarizer shown here saves 2.5 dB of signal relative to a system with no polarizer. In addition, high polarization isolation between the transmit and receive waves reduces effects of unwanted reflections, and thus improves the SNR of the image. For the configuration shown in Figure 5.1 with the polarizer between the polarizing beamsplitter and the dielectric lens, the required field of view is not greater than 20°. As the axial ratio of the polarizer degrades rapidly after 17°, images will appear “blurred” at the edges, due to non-CP reflections from the extremities of the target field plane. It is also possible to optimize the polarizer for off-axis performance, to achieve optimum axial ratio at, e.g., 15° off broadside. In this case, the *average* performance of the device would be increased, but an interesting and detrimental visual effect would be encountered. An annulus of high-quality imagery would be observed, with performance degrading monotonically both towards the center and the edges of the field of view. We have considered this tradeoff and decided in favor of optimum performance at broadside.

The Faraday rotation scheme utilized in other systems [32, 109, 33] suffers from greater loss at W-band than does the polarizer discussed in this chapter. The reported loss is 2 dB per pass. However, it is utilized in a passive system, where broad bandwidth is important; its bandwidth covers $f = (80\text{–}100)\,\text{GHz}$, while the periodic nature of the polarizer in this chapter limits its bandwidth to several gigahertz around its center frequency of $f_0 = 95\,\text{GHz}$. Additionally, we found isolation to be 38 dB, while the Faraday rotation method achieves only 20 dB of isolation.

CHAPTER 6

PASSIVE MILLIMETER-WAVE/TERAHERTZ IMAGING

The best place to hide anything is in plain view.

—Edgar Allan Poe, in *The Purloined Letter*

CONTENTS

6.1 NETD AND SPATIAL RESOLUTION

This section presents phenomenological analysis of images obtained by mechanically raster-scanning a single superconducting antenna-coupled microbolometer over a scene; the distance from the primary aperture to the object plane is approximately 1 m, and the size of the plane is approximately $1\,\mathrm{m}^2$. The device is a liquid helium-cooled ($T = 4.2\,\mathrm{K}$) vacuum-bridge Nb microbolometer, similar to those described in Chapter 2, coupled to a logarithmic spiral antenna with a bandwidth of $f = (0.1\text{–}1.2)$ THz. A voltage bias is applied to the arms of the spiral antenna, and the resulting current variation through the bolometer upon absorption of incident radiation is sensed by a low-noise room-temperature readout circuit—a version of the electronics described in [60]. This class of detectors features high sensitivity and low noise, that is, noise equivalent power of $\mathrm{NEP} = 25\,\mathrm{fW}/\sqrt{\mathrm{Hz}}$ and temperature resolution of $\mathrm{NETD} = 105\,\mathrm{mK}$ referenced to a lock-in amplifier time constant of $\tau_{int} = 30\,\mathrm{ms}$. To put this in perspective, fluctuations in the images, due to either background clutter, real temperature variations, or both, are greater than the system NETD of this specific configuration; this allows such features to be observed and analyzed directly. The relationship between NEP and NETD in the Rayleigh-Jeans limit is given by

$$\mathrm{NETD} = \frac{\mathrm{NEP}}{2\eta k_B \Delta f \sqrt{\tau_{int}}} \quad [\mathrm{K}], \tag{6.1}$$

where η is the efficiency of the power incident on the cryostat window being detected by the antenna-coupled microbolometer, and Δf is the bandwidth of the radiation (defined by the antenna, in this case). The power in a single spatial mode, in the Rayleigh-Jeans limit, is

$$P_{rf} = 2 k_B T \Delta f \quad [\mathrm{W}], \tag{6.2}$$

although for an antenna-coupled device, the factor of 2 is eliminated since antennas can receive only one polarization.

In an imaging system that utilizes a chopper to modulate P_{rf} incident on the detector, the actual power levels that are observed become much smaller; the temperature T in the above expression becomes ΔT. The detected signal is the difference between the room-temperature chopper and the "pixel" of the scene that is currently being observed by the detector. From this, it is clear that no discernable signal is present when observing objects that are at approximately the same radiometric temperature as the chopper, which is usually slightly colder than the room due to cooling from wind, and at times, from the Narcissus effect[1] . The greatest temperature contrast we typically observe in the lab is that of liquid nitrogen and the room temperature chopper, which gives $\Delta T = 295 - 77 = 218\,\mathrm{K}$. Even with this temperature contrast, the power incident on the cryostat window is 6.8 nW, and assuming 30 % transmission through the lenses and filters of a typical optical configuration (an example is shown in Figure. 6.1), about 2 nW is actually incident on the detector when chopped by a room-temperature chopper.

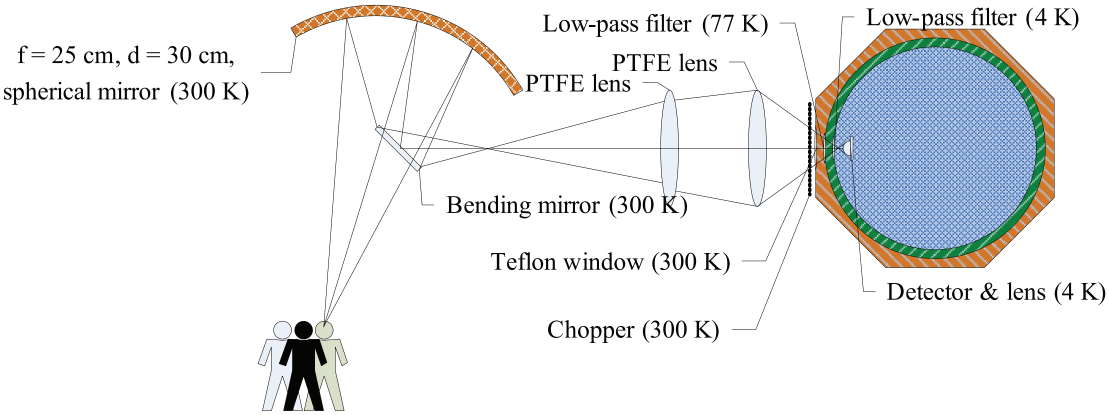

Figure 6.1: Top view of a drawing of the single-pixel raster-scanned optics configuration that acquired many images in this chapter. The spherical mirror is on an azimuth-elevation stage, positioned by stepper motors.

Each image in this section takes approximately 20 minutes to acquire; the actual integration time per pixel is $\tau_{int} = 10\,\mathrm{ms}$, and the number of pixels in each image is approximately (12 000–14 000). The majority of the acquisition time is occupied by the mechanical scanning of the primary collecting aperture, a 30 cm diameter spherical mirror mounted on a two-axis (azimuth-elevation) stepper motor stage. A description of this optics configuration is found in [62], and is shown in Figure 6.1.

---

[1] The Narcissus effect refers to the signal that is observed when the detector "sees" itself due to a reflection. If, for example, a mechanical chopper is at normal incidence in front of the cryostat window, the difference between the cold reflection and the warm room will be observed, rather than the difference between the room-temperature chopper and a warmer pixel.

The images are acquired in an uncontrolled indoor lab scene, with various equipment, lights, windows, and other sources of temperature fluctuation present in the background of the room. Therefore, the focus of this analysis is on the intended subject of the imaging system, that is, a human approximately 1 m from the primary collecting aperture of the system optics. There is a plywood wall covered with millimeter-wave anechoic foam immediately behind the human subject, the edges of which can be seen in most images. All images are unprocessed unless otherwise noted, i.e., each pixel represents incident irradiance, and the displayed images have not been smoothed, filtered, upsampled, or denoised. Because concealed threat detection is one of the possible and most attractive applications of passive terahertz imaging, a concealed object (a ceramic knife or metal gun) is included in each of the images. Objects in a scene, concealed or otherwise, are discriminated by their radiometric temperature contrast with either (1) other objects in, or (2) the background of, the scene. The radiometric temperature, $T_{rad}(f)$, of an object is given by

$$T_{rad}(f) = \epsilon(f) T_{obj} + [1 - \epsilon(f)] T_{bg} \quad [\mathrm{K}], \tag{6.3}$$

where $\epsilon(f)$ is the emissivity of the object, and the *obj* and *bg* subscripts represent the object and the background, respectively. Because $\epsilon(f)$ is a function of frequency, the radiometric temperature of any portion of the scene is equally dependent on frequency. In an indoor scene, the radiometric temperature contrast between objects and the background is extremely low when compared to an outdoor scene. Between a human subject and room temperature, which is generally the largest temperature contrast found indoors (with the exception of hot water-based beverages in expanded polystyrene foam containers), the temperature difference is only $\Delta T \approx 15\,\mathrm{K}$. The radiometric temperature contrast between threat objects and the human concealing them is less than $\Delta T = 10\,\mathrm{K}$, due to the transmissivity of clothing [100] and the fact that normal objects on or near the human body cannot exceed its physical temperature. The actual radiometric temperature of an object in a scene is considerably more complex than what (6.3) implies. Considering a scene one order more complex, in which a concealed object is hidden beneath only one later of clothing, the radiometric temperature of the concealed object is given by

$$
\begin{aligned}
T_{rad} = T_{obj} \cdot \epsilon_{obj} \cdot t_c \\
+ T_{bg} \cdot r_c + T_{bg} \cdot t_c^2 \cdot r_{obj} \\
+ T_c \cdot \epsilon_c + T_c \cdot \epsilon_c \cdot t_c \cdot r_{obj},
\end{aligned}
\tag{6.4}
$$

where r denotes reflectivity, t denotes transmissivity, and the subscript c denotes clothing. The frequency dependence from (6.3) has been omitted for clarity, but the emissivity, transmissivity, and reflectivity are all frequency-dependent.

An example image is shown in Figure 6.2. In this image, a human subject is concealing two objects beneath a cool-weather jacket. The concealed object on the left is a commercial millimeter-wave anechoic foam (the same material that constitutes the wall behind the subject); behind the foam is a ceramic (ZrO_2) knife, as in Figure 1.7, but clearly not seen due to the highly attenuating anechoic foam between it and the imaging system. On the right is a metallic gun. The zipper of the jacket is clearly seen, as are folds in the clothing. The circular hot spot in the background is a elementary calibration source, an expanded polystyrene foam cup of hot water that is visible through a small hole in the anechoic foam-covered plywood wall. This image, and the others that contain a temperature scale, are temperature calibrated by mapping the recorded electronics output (voltage) levels throughout the image to a scale containing two known points—that of the room-temperature background, and that of the hot water. The radiometric temperature of the hot water is not its physical temperature for the reasons discussed in the beginning of Chapter 3, but with knowledge of the properties of water [4] it can be estimated. With this crude calibration, the temperature scales on these images are accurate to within 5 K.

This section is divided into two topics. First, the minimum system NETD for detection of certain features is explored. This is accomplished by systematically adding Gaussian noise to the image until the features of interest are obscured by noise. Adding Gaussian noise to an image with very low noise produces the same resulting image as acquiring an image with a noisy system or detector in the first place, so we can determine the minimum system NETD that is required in order for specific objects or features in an image to be detected. The second topic is the effective

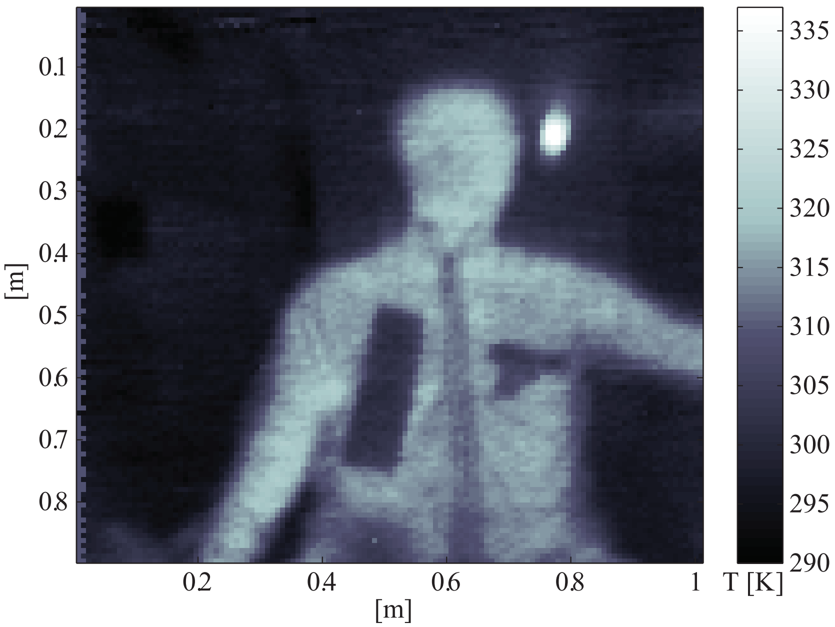

Figure 6.2: Broadband passive terahertz image of a human subject with two concealed objects beneath a jacket. On the left is a commercial millimeter-wave anechoic foam, and on the right is a metallic gun. The zipper is plainly visible, as is the collar, and folds/wrinkles in the jacket. The warm circular region next to the head of the human subject is a temperature calibration target.

frequency of operation. Spatial resolution is proportional to frequency, but in a broadband system the frequency is not well-defined. By applying diffraction theory, the effective frequency and therefore the diffraction-limited resolution is found.

The requirements on system and display parameters are well known in the infrared and visible regions of the spectrum; these imaging systems and their associated image processing algorithms are very mature. Recently, an effort has been made to bring this level of sophistication to active imaging systems at $f = 650\,\mathrm{GHz}$ [124, 125]. For any receiver system where detection or identification of objects is the goal, from radar to visible, the end result of such formalisms is realized in the form of receiver operating characteristics (ROC) curves. ROC curves draw from both empirical and analytic data on target/object properties, human interpretation of displayed images, atmospheric transmission, and system-level parameters such as noise, sensitivity, and resolution. The work in [124, 125] has primarily focused on probability of detection (P_d) as a function of range, while standard ROC curves also include probability of false alarm, P_{fa}. Nonetheless, for active imaging systems, the two parameters that are of greatest importance in maximizing P_d are NEP and spatial resolution. For a fixed target size and range, NEP, in combination with transmitted power and target reflectivity, can provide an effective target visibility. In the passive modality, radiometric temperature resolution (NETD) is a more directly useful figure of merit, and thus our goal in this section is to determine those two fundamental system inputs for the ROC curves: NETD and spatial resolution.

6.1.1 Necessary system NETD

Distinctions need to be made between theoretical device NETD, measured device NETD, and final system NETD. Essentially there are four separate levels of NETD specifications, ranging from the lowest (best) values (theoretical device-only) to the highest (worst) values (actual device implemented in a final system). At the lowest level there is the theoretical noise defined (in a bolometer) by the Johnson and phonon noise sources (Chapter 2), and the responsivity derived from the theoretical I–V curves. The next level can be realized in one of two ways: first, measured noise in combination with theoretical responsivity; second, measured responsivity in combination with theoretical noise. The latter requires that the device be exposed to rf signal power. The next level is that of a complete device measurement, where noise and responsivity are simultaneously measured in a system where the detector is exposed to rf signal power. Typically the detector is exposed, in succession, to chopped signals from large temperature contrasts (liquid nitrogen, for example) and nominally zero temperature contrasts (room-temperature anechoic foam). In this manner, detector noise and responsivity are characterized simply by analyzing a time-trace of this progression; noise on an actual signal is measured, as is the signal power, and also noise when no radiometric signal is present. Finally, measurement of noise and responsivity can be performed in a complete system, for example, by scanning a detector over a scene with a known temperature contrast (the ABC source is an appropriate signal source). By performing a measurement in the final system, the optical or quasi-optical efficiencies are included in the reported NETD. These various methods of specifying NETD are summarized in Table 6.1.

Between levels 1 and $2a$, a lumped efficiency can be deduced. The efficiency, usually denoted η, stems from the difference between the theoretical responsivity and the measured responsivity

Table 6.1: Categorization of NETD specifications

level	description
1	theoretical responsivity, theoretical noise
$2a$	theoretical responsivity, measured noise
$2b$	theoretical noise, measured responsivity
3	measured noise and responsivity
4	measured noise and responsivity in complete system

(e.g., $S_I^{\text{meas}}/S_I^{\text{theory}} = \eta$); measured responsivity always includes non-ideal components such as vacuum windows, infrared filters, and lens reflections, etc., hence the "lumped" designation. η is not dependent on theoretical or realized noise, as it corresponds to signal response measurements only. Measurements of actual noise, vs. theoretical noise, will provide extra information about noise sources not due to the Johnson or phonon contributions, such as amplifier readout noise, or $1/f$ noise.

The background clutter and real temperature variations in the scene can be directly measured in images we acquire since the temperature fluctuations are above the NETD of the device. The measured standard deviation in the images is in the range of (150–300) mK in small regions of interest representing several square meters of quasi-uniform, yet uncontrolled, background. In small regions of the anechoic wall behind the human subject, the standard deviation is (100–120) mK, which is quite close to the measured detector NETD (level 3 in Table 6.1). Also easily measured is the radiometric temperature difference between natural folds or ripples in clothes (corresponding to lying against the human body or several centimeters away from the body), and between human and the concealed threat object. Because the system has a low enough NETD for these observations, the images provide a valuable baseline for understanding the necessary sensitivity requirements for systems or devices. That is to say, with a certain system NETD, a confidence level can be realized for the ability of the system to view varying levels of detail in the images. Figure 6.3 (left) is an image with a measured NETD $\approx 0.2\,\text{K}$ in the background. Figure 6.3 (right) shows the temperature profile along the white line in Figure 6.3 (left); the folds in the clothing (e.g. the sleeve on the left side of the image) create a temperature variation of $\Delta T \approx (1\text{–}3)\,\mathrm{K}$, while the concealed ceramic knife gives $\Delta T \approx 8\,\mathrm{K}$. The feature in the center of the image is due to a thick collar where four layers of material overlap, providing $\Delta T \approx 5\,\mathrm{K}$. Basing image quality on features such as folds in clothes or clothing shadows is subjective, yet there is a standard term applied to these natural attributes which we see everyday with visible light, and that is "scene clutter." When natural scene clutter exists in a terahertz image such as Figure 6.3 (left), it becomes easier for our eyes and associated signal processing to detect objects which are out of place. When the scene clutter is obscured by noise, it becomes more difficult to trust that our eyes are indeed detecting a concealed threat object and not a noisy feature which, in a noise-free image, could be natural clutter which we are used to observing.

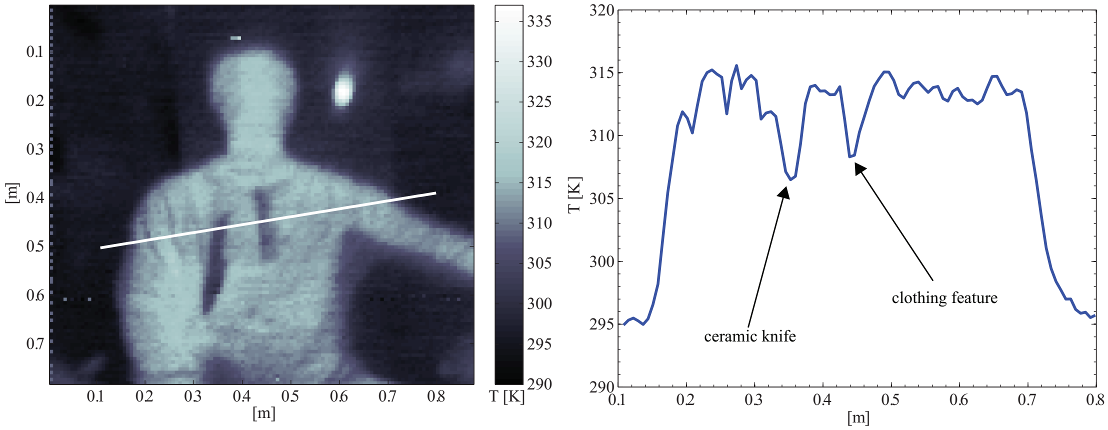

Figure 6.3: (left) Image with measured NETD $= 0.2\,\mathrm{K}$ in the background, and a ZrO_2 knife concealed under two layers of clothing. (right) Cut through image (white line at left) showing temperature variations. Folds in clothing correspond to ΔT between $(1\text{–}3)\,\mathrm{K}$, while the knife shows an $8\,\mathrm{K}$ difference. The clothing feature in the center creates a difference of $5\,\mathrm{K}$.

To determine how a specific increased NETD conceals the features that make this image look qualitatively good, Gaussian white noise is added to the image, where the standard deviation, σ, of the Gaussian function is equal to the NETD of the noise. Additive white Gaussian noise is the correct category of noise to add in this situation, because we are attempting to simulate entire imaging systems with higher noise levels. Specific noise sources could be isolated, however; for example, if actual Gaussian temperature fluctuations were thought to be present in the scene (in the time required for a single image acquisition) and a bolometric detector was the detector of choice, noise with a χ^2 distribution should be added to the final image.

Setting σ in the Gaussian function to values corresponding to features of interest in the image and then viewing the images allows subjective determination of whether or not certain features are concealed by the added noise. Because the noise is uncorrelated with existing noise in the image, the total σ in the same region of the background where the original noise measurement was taken is approximately equal to the added noise. That is to say, when Gaussian noise with $\sigma = 0.5\,\mathrm{K}$ is added to an image with $\sigma = 0.2\,\mathrm{K}$, the total σ in the analyzed area of the image is approximately $0.5\,\mathrm{K}$. Figure 6.4 demonstrates addition of Gaussian white noise to the image of Figure 6.3 (left). It is seen that as Gaussian white noise is added to the images with σ equal to ΔT corresponding to features shown in Figure 6.3 (right), the features themselves become undetectable. The noise in Figure 6.4 (upper left) decreases the visibility of the clothing folds on the left, while any features noticed on the right are obscured completely. Similarly, in Figure 6.4 (upper right), the folds are hard to identify without previous knowledge of their existence. In Figure 6.4 (lower left), it is difficult to differentiate between the concealed weapon and the clothing feature. Finally, without *a priori* information about Figure 6.4(lower right), knowledge of a concealed weapon is non-existent. Although the ceramic knife registers as a cooler region in this image, a definitive statement cannot be made about its identity; it may be incorrectly identified as a clothing feature.

6.1.2 Spatial resolution

Spatial resolution targets, combined with the calibration source discussed in Chapter 3, are currently being developed for systematic measurement of the system (combined optics and detector) modulation transfer function (MTF). The MTF is a standard measurement of spatial resolution [126], and the end product and test methodology will provide important results about passive broadband millimeter-wave/terahertz imaging. A model for concealed weapon identification for active terahertz imaging systems, based on the MTF of each component in the system, has been proposed [124, 125] and a similar performance metric can be implemented for the passive modality. However, there are other methods of determining the spatial resolution capabilities of a system. Because the system bandwidth covers a decade, its spatial resolution is not well-defined. The angular diameter of the Airy disk, θ, to the first null is given by

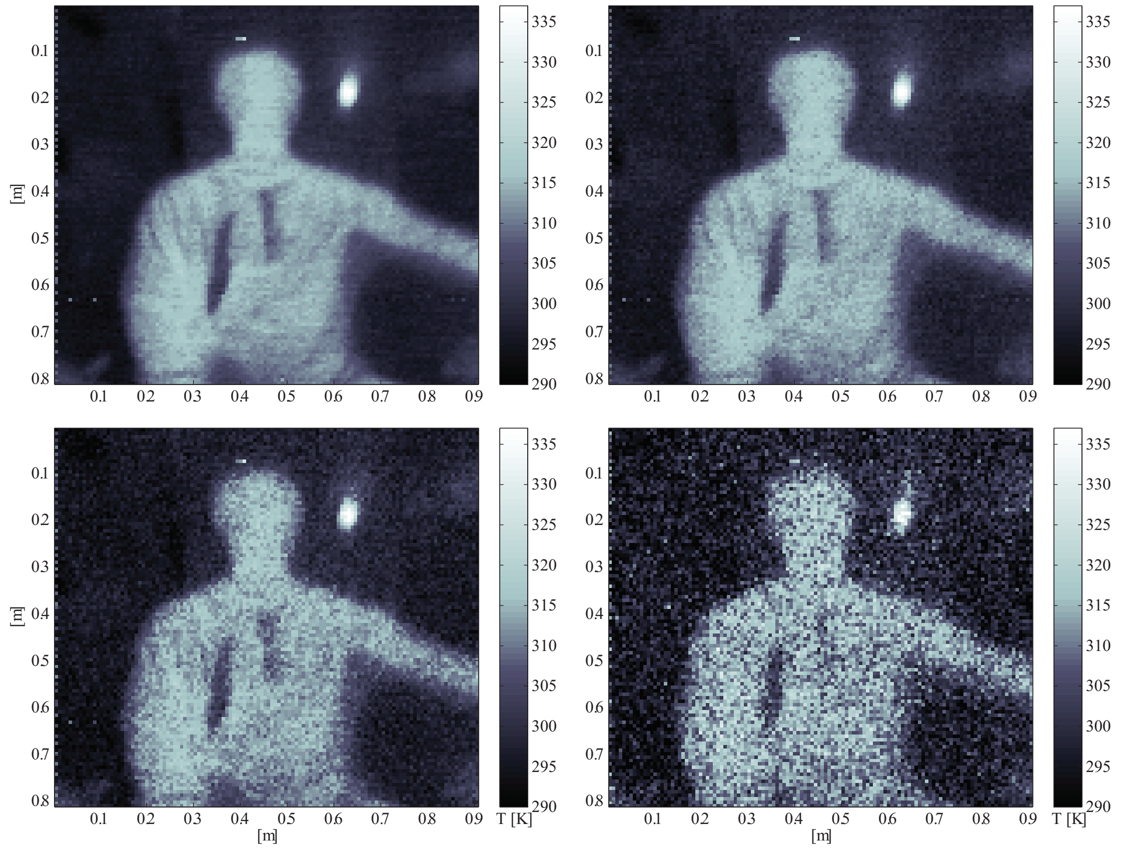

Figure 6.4: Images with added Gaussian white noise, for NETD levels greater than seen in Figure 6.3 (left). (upper left) NETD = 0.5 K; (upper right) NETD = 1 K; (lower left) NETD = 2 K; (lower right) NETD = 5 K.

$$\sin\theta = \frac{2.44\lambda}{d}, \tag{6.5}$$

where d is the diameter of the primary aperture. Clearly, it is desirable to understand the *effective* frequency of operation which determines the resolution in the image, besides the scan-limited performance based on spatial dimensions of a pixel. One method of achieving this goal is to measure the transition between the target and the background along an edge, which is ideally a step function (as in a resolution target), and compare the non-ideal step slope with the slope found in diffraction theory. Due to the raster-scanned nature of the optics configuration, the vertical and horizontal spatial resolution is not the same. The raster scanning in these images is row-based, where completion of a single row scan requires approximately fifteen seconds. The vertical resolution suffers due to small movements of the human subject being imaged, as the time required to scan through a vertical rectangular region along an edge is longer than the time required for a horizontal edge.

The parameters for a horizontal scan include the azimuthal velocity v in units of deg/s or mm/s, the lock-in amplifier time constant (integration time) τ_{int}, and the data acquisition system sampling rate of the amplifier. The latter is less important, because we choose the sampling rate to be $1/\tau_{int}$, such that the data are sampled ideally. Thus the time required for acquisition of a row of pixels is approximately $n\tau_{int}$, where n is the number of pixels in a row. The scan velocity v must be chosen such that $\tau_{int}v$ is less than the diffraction-limited spot size from (6.5), or adjacent samples will not contain independent information (that is, there will be blurring).

To analyze the edge sharpness, several images were considered, and vertical and horizontal edges in each of them were analyzed. A program was developed to select edges that are neither horizontal nor vertical; after selection of the desired edge region area, the data are interpolated with a bicubic spline in order to rotate it into a rectangular matrix for averaging along the length of the rectangle. It is seen in Figure 6.5 that the lower half of the measured edge transition curves indeed match diffraction theory at a frequency of $f = 400\,\text{GHz}$. For the upper half of the measured curve, no decaying ringing is seen as in edge diffraction, but the asymptotic approach to the maximum magnitude occurs at the same rate. A reasonable conclusion can be made, which is that although the system is basically a radiometer, the end data of interest is an image, much like a thermal camera provides. A thermal profile is therefore observed for the upper region of the curve, where the maximum temperature reached is inset from the edge of the body. The decaying ringing is due to the finite and sharp cutoff frequency; as the cutoff frequency is increased, the maximum amplitude decreases, and the ripple period increases. Eventually a step function is realized [127]. Also noted is that the asymptotic approach to the maximum normalized temperature can vary between areas of the image, due to the reflected background temperature varying by several degrees between the ceiling of the lab and the walls. This causes a more rapid increase for the horizontal edge where the majority of the reflected background is the ceiling, while for the vertical edge the walls are the major contributor of reflected background temperature.

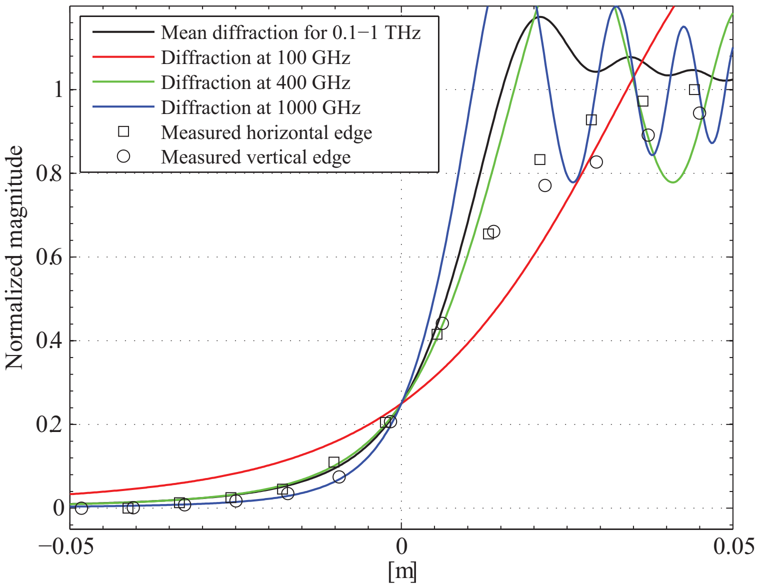

Figure 6.5: Measured average horizontal and vertical edge sharpness, and theoretical diffraction from perfect edges at various frequencies.

6.1.3 DISCUSSION

In this section, phenomenological analysis of passive indoor terahertz imagery has been presented. It has been shown that the minimum NETD for effective concealed object detection is NETD = 0.5 K in unprocessed images. Above NETD = 0.5 K, the noise obscures the scene clutter that allows both humans and signal processing algorithms to adequately process the image for conclusive object detection. This NETD was suggested in [62] and has now been empirically confirmed, due to the availability of a detector with NETD ≈ 100 mK temperature sensitivity. Resolution performance can be reduced to three components. First, the method of scanning and timing of sampling and integrating can cause adjacent pixel blur. In the images shown here, however, the scan velocity was set low enough such that the integration for each pixel is completely distinct, i.e., integration is not overlapping for adjacent pixels. This is non-optimal and adds significant time to the acquisition, but the scanning effect becomes negligible. Second, diffraction theory shows a definite limit, which was identified. The resolution of the system is based on the f-number and effective frequency, which was found to be approximately $f = 400\,\mathrm{GHz}$

based on the compared gradients from diffraction theory and measured edge transitions. This approximate frequency was directly measured by Bjarnason using a photomixer [128], and noted in Grossman et al. [129]. The diffraction-limited resolution at the target distances in the images is thus 2.3 mm at this effective imaging frequency, but the spatial pixel size is greater than that limit. Finally, scene variation is a factor—both thermal drifts and human movement during the duration of the acquisition are parameters for which is it difficult to compensate.

6.2 Image processing

Because the acquired images have several unfavorable attributes for those in the image processing community (low pixel count, low SNR, and low spatial resolution), most well-developed image processing techniques that are common for infrared, visible, and x-ray images are not directly applicable. Several image processing techniques that accommodate these shortcomings have been performed on these images, however. The methods discussed here are completely unsupervised, meaning that no *a priori* information about the image is provided to the algorithm. Pre-processing using a 3×3 neighborhood standard deviation filter in order to enhance temperature contrast on feature edges was performed by Ramírez et al. [14], as shown in Figure 6.6 (compare to the unprocessed version, Figure 6.2). Also in [14], unsupervised classification algorithms were applied to the images shown in this chapter to segment the concealed objects from the surrounding human subject by use of first-order clustering. In Shen et al. [15], the same images are processed using a variety of algorithms; feature extraction using a multilevel thresholding, or histogram-based, algorithm was proven to be the most effective of those attempted.

6.3 Multi-detector imaging

Recently we have begun imaging with eight antenna-coupled microbolometers simultaneously. Besides the increase in the number of detectors, we are utilizing a liquid cryogen-free, closed-cycle cryocooler. This system takes only a few hours to reach cryogenic operation from room temperature, and is painless in operation compared with daily transfers of liquid nitrogen and

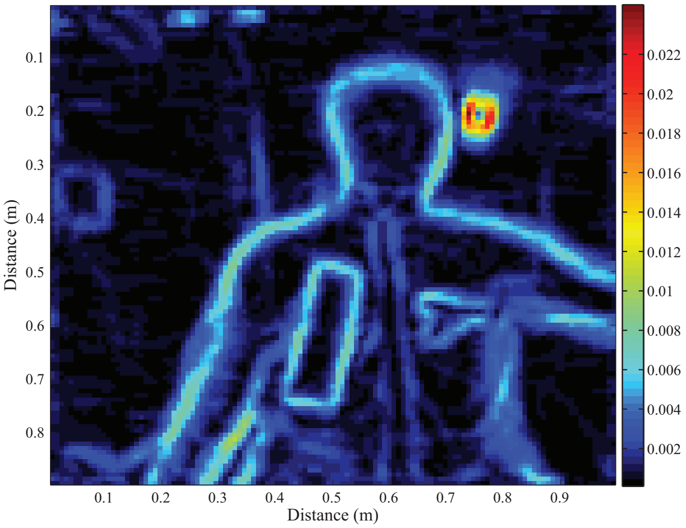

Figure 6.6: Pre-processing of radiometrically calibrated image using a texture analysis deviation filter to reveal small temperature differences across the image, allowing them to become visually obvious. Used with permission from [14]. Compare to the unprocessed version, Figure 6.2.

liquid helium. In the long term, cryocoolers of this sort greatly reduce the operating costs and complexities associated with traditional liquid nitrogen and liquid helium cryostats [130], and imaging systems utilizing them can be operated for years without maintenance by individuals with no formal training in cryogenics. The eight-detector system raster scans the multiple detectors over the scene much like the single-detector system did, but with a slightly different optical configuration that is described in [131], which has an adjustable range to the object plane, set to 2 m for Figure 6.8. The system utilizes a single, eight-detector module, in which a Si chip with a 1×8 array of antenna-coupled microbolometers is located; the hemispherical Si lenses are 2 mm in diameter rather than the 4 mm diameter lenses used in the single-detector systems (Chapter 2 and Chapter 4), doubling the FWHM to $9\,\mathrm{THz} \cdot \mathrm{degrees}/f$. A photograph of an assembled module is shown in Figure 6.7. The antennas that are coupled to the microbolometers are the same as those discussed in Chapter 2 with nominal frequency ranges of either $f = (0.2\text{–}1.8)$ THz or $f = (0.2\text{–}3.6)$ THz, compared to the $f = (100\text{–}1200)$ GHz bandwidth of the detector that was used to acquire the images earlier in this chapter.

This system is able to acquire images at a rate approximately eight times faster than the single-detector system described above, when using the same integration time per pixel (τ_{int}) for

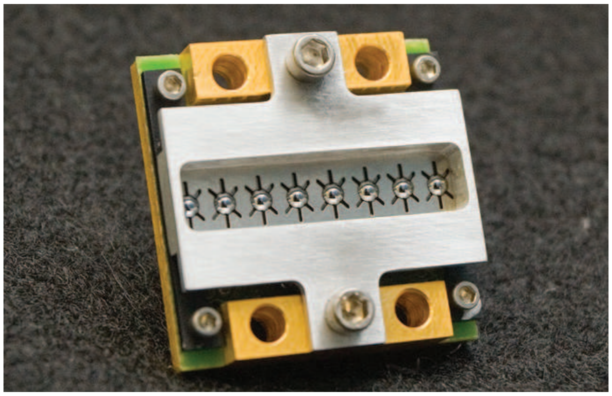

Figure 6.7: Photograph of an assembled 1 × 8 linear array of antenna-coupled microbolometers. The Si lenses are each 2 mm in diameter.

images with the same number of horizontal rows. In row-based raster scanning, a single row with $(2 \cdot m)$ pixels takes less time to acquire than two rows each with m pixels, due to the additional time required to adjust the elevation angle of the mirror for acquisition of a second row. An example image taken with this system is shown in Figure 6.8; at the time of the acquisition, only seven detectors were operable due to a bad electrical contact to the eighth detector. The missing detector was on an end of the 1 × 8 array, so the elevation angle adjustment before each seven-detector row was adjusted accordingly. Because of the variations in responsivity and noise from detector to detector, faint horizontal stripes in the direction of the scan (azimuth) are observed. Elementary *ex post facto* stripe removal was performed by varying the offset and gain of each detector, but the stripes remain visible at a low level.

6.4 CURRENT WORK

A 128-detector system is currently being constructed. It utilizes a compact all-reflective Schmidt telescope optics configuration, and a conical scanner. With 256 discrete scan angles offered by the conical scanner, the resulting images will contain approximately 30 000 pixels per image frame, and frames will be acquired at near-video (20 Hz) rates. The detectors are oriented in a linear array, with sixteen of the 1 × 8 modules shown in Figure 6.7 placed end to end. This line of detectors is then conically scanned over the target plane such that each detector traces a circle; these circles overlap each other in the target plane, and are stacked from one end to the

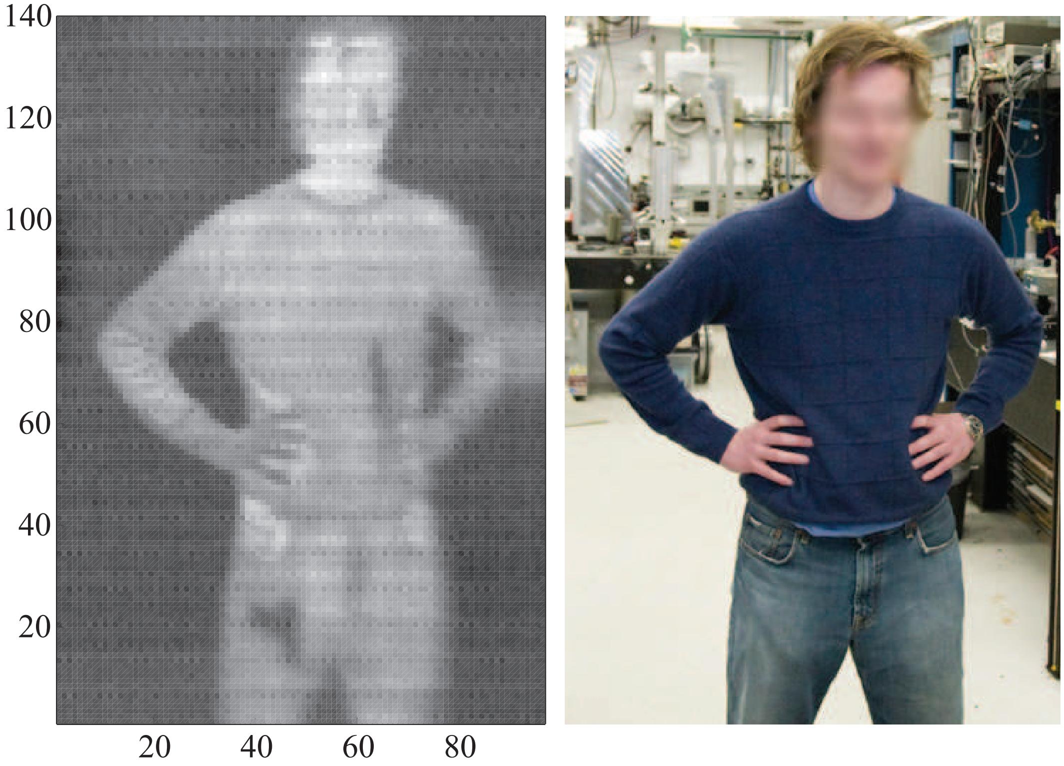

Figure 6.8: Image acquired with an 8-ACMB system. The human subject is standing around 2 m from the primary aperture. The concealed objects include a ceramic knife under the sweater and a metallic gun in the jeans pocket. The increased radiometric temperature due to the hand pushing the sweater against the body can be seen clearly. Clothing features such as a thicker collar and the jeans zipper and pocket outlines are also visible.

other. The resulting field of view is a stadium, that is, a rectangle whose ends are capped by semicircles. The cryostat and optics are shown in Figure 6.9.

Several differences between the images that will be acquired with this system and those that have been acquired in the slower, raster-scanning systems are apparent. First, long-term effects such as temperature fluctuations in the scene or human subject movement, will no longer be present due to the decreased frame acquisition time. Second, the "striping" that is visible in the images acquired by the 1 × 8 module-based (eight simultaneously operating detectors) system due to detector nonuniformity can be eliminated via a procedure known as "dynamic flat-fielding." Essentially, this is a real-time calibration process in which *different* detectors that observe the *same* location in the object plane within a very short time period (due to the conical scanner rapidly scanning the object plane) can be calibrated to each other. This calibration process can

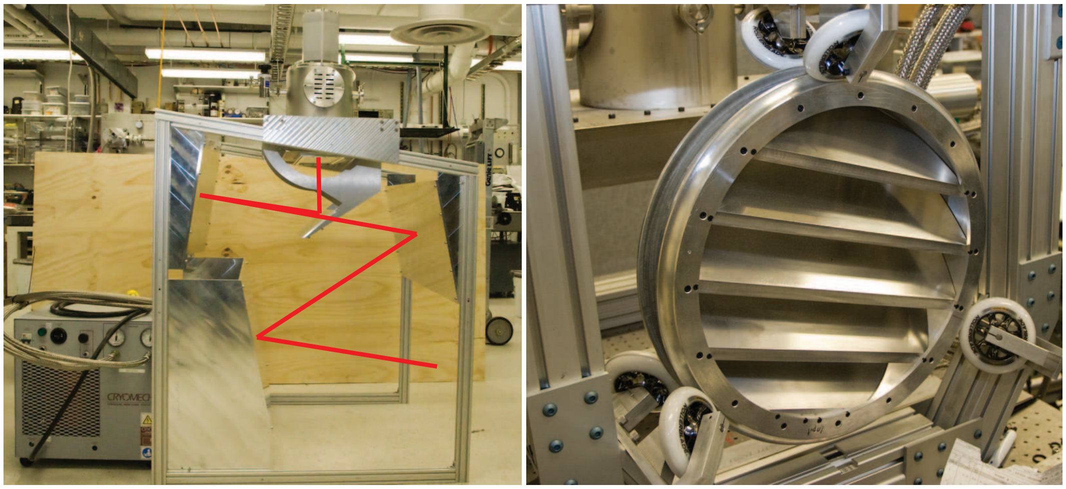

Figure 6.9: Photographs of (left) 128-detector cryostat and Schmidt telescope optics, and (right) conical scanner. In the photograph on the left, the cryostat is directly above the vertical line. The line represents the optical path; the conical scanner will be located at the output of the optics, i.e., at the lower-right corner of the photograph.

be propagated throughout the detector array and object plane, allowing offsets due to detector nonuniformity or electronics gain variation to be reduced or eliminated.

6.5 DISCUSSION

An important attribute of imaging in the broadband passive millimeter-wave/terahertz frequency range is demonstrated by the images in this chapter. Because of the broad frequency range of radiometric temperature information that they contain, it is possible to both observe objects concealed beneath clothing as well as the clothing itself, depending on which is the dominant signal. Room-temperature radiation that is scattered from clothing and clothing-temperature radiation emitted from the clothing contributes to image formation at high frequencies (above 1 THz), due to decreased transmission [100]. These clothing surface features, or any objects not obscured by clothing, benefit from increased spatial resolution due to the shorter wavelength. On the other hand, these short wavelengths are filtered upon transmission through clothing (both reflected room-temperature radiation as well as radiation emitted by the concealed object), so the observed resolution of concealed objects is lower, and is determined by the properties of the specific clothing at lower frequencies [28].

Specific examples include the shadow under the left arm of the subject in Figure 6.2. This shadow is due to the warmer temperature of the sweater which was draped from the body and arm. In the same image, the central clothing feature below the neck could be mistaken for a concealed object, if not compared simultaneously with a visible image. The lower temperature of this clothing feature stems from several effects: the surface of the feature is colder than the rest of the clothing because it is thicker; and because of the thickness, the radiation emitted from the subject immediately behind this feature is attenuated more severely than in the surrounding areas. Examples in a second image, Figure 6.8, are directly observable. Again, clothing features are visible, such as the thicker collar, and the jeans pocket outlines and zipper. More importantly however, the spatial resolution where the right hand is pressed against the sweater is greater than that of the gun in the jeans pocket. This agrees with the earlier theory, that resolution through clothing is degraded due to the filtering of shorter wavelengths.

Because of the frequency-dependent properties of materials including clothing, the concept of multispectral imaging in this frequency range has been considered. By using either multiple narrowband detectors per image pixel (analogous to red, green, and blue in a computer monitor, for example) or a frequency-selective surface [80] that would work with the existing broadband detectors, multiple narrowband images of the same scene can be acquired. Combined with knowledge of material [35] and clothing [100] properties as a function of frequency, computer systems can make accurate estimates about the actual properties of objects that have been detected and segmented from the surrounding body.

Chapter 7

Summary and contributions

Contents

7.1 Summary and conclusions

In summary, the work presented in this thesis contributes to increasing the knowledge base in the field of millimeter-wave and terahertz imaging in the following specific areas: (1) detectors; (2) quasi-optical and other imaging system components; (3) metrology; and (4) phenomenology of passive broadband images. The specific contributions in each area are summarized here:

(1) Direct bolometric detectors were used for the imaging systems presented here. Although there exists a broad existing knowledge base in this field, a systematic comparison of two inexpensive detector technologies has not been done before. The variety of materials that can be used for terahertz detectors is limited, and thus it is felt that the comparison between Nb and NbN microbolometers presented in this thesis is a useful contribution. The detectors which were integrated with the same antenna were compared in terms of

their responsivities, thermal properties, biasing properties, noise properties, sensitivity and ease of fabrication.

(2) The millimeter-wave and terahertz frequency ranges sit between the microwave and optical domains. On one hand, the small wavelength and material losses are too high to make components such as metallic waveguides and coaxial lines practical, and transistors and other active devices do not exist commercially. On the other hand, the wavelength is large for optical components and diffraction plays a major role. Thus, development of quasi-optical components which use both microwave and optical techniques becomes necessary. An example of such a component is a new type of linear-to-circular polarization converter developed in this thesis.

(3) The Aqueous Blackbody Calibration source represents part of the first concerted effort to develop a metrological infrastructure in the millimeter-wave/terahertz frequency regime. In general, the three components required in a traceability chain are: absolutely calibrated sources, filters, and detectors. Absolutely calibrated detectors can be realized via electrical substitution techniques, for example, and with an absolutely calibrated source (the ABC source), filters can be extremely accurately calibrated. An effort at such bandpass filters is underway [80].

(4) As eluded to in Chapter 6, passive millimeter-wave and terahertz imaging has specific advantages over many other types of imaging for security applications, including active millimeter-wave, x-ray backscatter, passive narrowband, and passive and active heterodyne. These advantages include information content, resolution, cost, and simplicity of implementation. Overall, it is felt that passive broadband millimeter-wave/terahertz imaging systems provide the best combination of favorable attributes for security applications.

7.2 FUTURE DIRECTIONS

Each of the topics outlined above contains areas for future research, some of which are listed here.

(1) In terms of basic radiometric sensing devices, there are many areas of improvement that follow from the work in this thesis. One example is an improved design of the antenna element. In the work presented here, spiral antennas with substrate lenses, developed in the 1980s and 1990s were used, and the focus was on the detector. Substrate lenses are inconvenient for a number of reasons, including positioning, fabrication difficulty, and cost. Eliminating the lens while suppressing substrate modes would be a worthwhile future research effort. A possible direction are endfire antennas supported by thin membranes. In addition, multiple polarizations can be explored to acquire additional information content in the image.

(2) The images presented in this thesis are broadband—$f \approx (0.1\text{–}3.6)\,\mathrm{THz}$—and thus contain and integrated response of the materials, objects, and their associated temperatures in the scene. More information can be obtain by using multispectral imaging (i.e., several individual smaller frequency bands), and in a passive imaging system this would be implemented by use of a quasi-optical component designed using similar methods as the polarizer described in Chapter 5. One such type of bandpass filter is presented in [80], and with a simple modification it could be used in any of the imaging systems discussed in Chapter 6.

(3) The ABC source in its current form is an accurate and useful calibrator for the millimeter-wave/terahertz frequency range, but its performance and usability could be increased further by appropriate geometry choices that will decrease the bowing of the water surfaces (depicted in Figure 3.6) and decrease the time required to adjust its radiometric temperature. These include reducing its dimensions and working with the manufacturer to refine the properties of the EPS foam, to increase its strength and watertightness while reducing its rf absorption. Further steps to decrease the undesirable EPS properties could include completely replacing it with “windows” of another material, one that is electrically thin and transparent.

(4) The conically-scanned 128-detector imaging system discussed briefly in Chapter 6 will be

completed within a few months. Its focal plane array (FPA) is linear (1 × 128) and flat, which produces two categories of effects that can be improved. These include improving detector efficiency for the outer-most detectors on the array (possibly by reconfiguring to a 2 × 64 FPA layout), and introduction of curvature to the FPA in order to flatten the focal surface in the object plane. Because the system is entirely modular, these changes will require re-engineering only the components specifically associated with the FPA, that is, the 4 K "cold finger" and the circuit boards that the 1 × 8 modules connect to.

7.3 Conclusion

In conclusion, the field of millimeter-wave and terahertz imaging combines areas of microwave engineering, optics, device physics, and cryogenics, and there is room for a lot of creative solutions to minimize cost, complexity, and increase quality as individual technologies improve. It will be very interesting to see what the progress of the field is in ten years, and whether or not passive millimeter-wave/terahertz imaging has appeared as the dominant technology for security screening of humans. It is hoped that this thesis contributes to the foundations that will enable future exciting developments.

Bibliography

[1] C. H. Townes and A. L. Schawlow, *Microwave Spectroscopy.* New York: McGraw-Hill, second ed., 1955. 2

[2] H. B. Wallace, "AEM software." 2, 64

[3] E. N. Grossman, "Atmospheric Transmission (AT) software." 2

[4] J. T. Kindt and C. A. Schmuttenmaer, "Far-infrared dielectric properties of polar liquids probed by femtosecond terahertz pulse spectroscopy," *Journal of Physical Chemistry*, vol. 100, pp. 10373–10379, June 1996. 2, 14, 52, 55, 56, 60, 61, 65, 66, 73, 108

[5] G. Zhao, M. ter mors, T. Wenckebach, and P. C. M. Planken, "Terahertz dielectric properties of polystyrene foam," *Journal of the Optical Society of America B*, vol. 19, pp. 1476–1479, June 2002. 2, 58, 59, 70, 76, 81, 84

[6] Y. C. Shen, T. Lo, P. F. Taday, B. E. Cole, W. R. Tribe, and M. C. Kemp, "Detection and identification of explosives using terahertz pulsed spectroscopic imaging," *Applied Physics Letters*, vol. 86, no. 24, 2005. 2

[7] C. M. Stickley and M. E. Filipkowski, "MIcroantenna Arrays: Technology and Applications (MIATA)—an overview," in *Passive Millimetre-Wave and Terahertz Imaging and Technology* (R. Appleby, J. M. Chamberlain, and K. A. Krapels, eds.), vol. 5619, pp. 47–58, SPIE, 2004. 3, 12, 14, 49

[8] C. R. Dietlein, A. Luukanen, J. S. Penttilä, H. Sipola, L. Grönberg, H. Seppä, P. Helistö, and E. N. Grossman, "Performance comparison of nb and nbn antenna-coupled microbolometers," in *Terahertz for Military and Security Applications* (J. O. Jensen and H. L. Cui, eds.), vol. 6549, SPIE, 2007. 3

[9] C. R. Dietlein, J. D. Chisum, M. D. Ramírez, A. Luukanen, E. N. Grossman, and Z. Popović, "Integrated microbolometer antenna characterization from 95-650 GHz," in *IEEE/MTT-S International Microwave Symposium*, pp. 1165–1168, 2007. 3

[10] C. R. Dietlein, Z. Popović, and E. N. Grossman, "Broadband THz aqueous blackbody calibration source," in *Passive Millimeter-Wave Imaging Technology* (R. Appleby and D. A. Wikner, eds.), vol. 6548, SPIE, 2007. 3

[11] C. R. Dietlein, Z. Popović, and E. N. Grossman, "Aqueous blackbody calibration source for millimeter-wave/terahertz metrology," *Applied Optics*, 2008. 3

[12] C. R. Dietlein, J. E. Bjarnason, E. N. Grossman, and Z. Popović, "Absorption, transmission, and scattering of expanded polystyrene at millimeter-wave and terahertz frequencies," in *Passive Millimeter-Wave Imaging Technology* (R. Appleby and D. A. Wikner, eds.), vol. 6948, SPIE, 2008. 3

[13] C. R. Dietlein, A. Luukanen, F. Meyer, Z. Popović, and E. N. Grossman, "Phenomenology of passive broadband terahertz images," in *Proc. 4th ESA Workshop on Millimeter-wave Technology and Applications*, 2006. 3

[14] M. D. Ramírez, C. R. Dietlein, E. N. Grossman, and Z. Popović, "Unsupervised image segmentation for passive THz broadband images for concealed weapon detection," in *Terahertz for Military and Security Applications* (J. O. Jensen and H. L. Cui, eds.), vol. 6549 of *Presented at the Society of Photo-Optical Instrumentation Engineers (SPIE) Conference*, May 2007. 3, 117, 118

[15] X. Shen, C. R. Dietlein, E. N. Grossman, Z. Popović, and F. G. Meyer, "Detection and segmentation of concealed objects in terahertz images," *IEEE Transactions on Image Processing*, 2008. 3, 117

[16] C. R. Dietlein, A. Luukanen, Z. Popović, and E. N. Grossman, "A W-band polarization converter and isolator," *IEEE Transactions on Antennas and Propagation*, vol. 55, no. 6, pp. 1804–1809, 2007. 3

[17] T. W. Crowe, T. C. Grein, R. Zimmermann, and P. Zimmermann, "Progress toward solid-state local oscillators at 1 THz," *IEEE Microwave and Guided Wave Letters*, vol. 6, no. 5, pp. 207–208, 1996. 5

[18] R. Kohler, A. Tredicucci, F. Beltram, H. E. Beere, E. H. Linfield, G. A. Davies, D. A. Ritchie, R. C. Iotti, and F. Rossi, "Terahertz semiconductor-heterostructure laser," *Nature*, vol. 417, pp. 156–159, May 2002. 5

[19] J. Tucek, K. Kreischer, D. Gallagher, R. Vogel, and R. Mihailovich, “Development and operation of a 650 GHz folded waveguide source,” in *IEEE International Vacuum Electronics Conference*, pp. 1–2, 2007. 5

[20] N. M. Vaidya and T. Williams, “A novel approach to automatic threat detection in MMW imagery of people scanned in portals,” in *Passive Millimeter-Wave Imaging Technology* (R. Appleby and D. A. Wikner, eds.), vol. 6948, SPIE, 2008. 8

[21] A. Luukanen and J. P. Pekola, “A superconducting antenna-coupled hot-spot microbolometer,” *Applied Physics Letters*, vol. 82, no. 22, pp. 3970–3972, 2003. 9, 30, 31

[22] A. J. Miller, A. Luukanen, and E. N. Grossman, “Micromachined antenna-coupled uncooled microbolometers for terahertz imaging arrays,” in *Terahertz for Military and Security Applications* (R. J. Hwu and D. L. Woolard, eds.), vol. 5411, pp. 18–24, SPIE, 2004. 9, 36, 93

[23] E. N. Grossman, A. Luukanen, and A. J. Miller, “Terahertz active direct detection imagers,” in *Terahertz for Military and Security Applications* (R. J. Hwu and D. L. Woolard, eds.), vol. 5411, pp. 68–77, SPIE, 2004. 9, 92, 93

[24] D. M. Sheen, D. L. Mcmakin, and T. E. Hall, “Cylindrical millimeter-wave imaging technique for concealed weapon detection,” in *26th AIPR Workshop: Exploiting New Image Sources and Sensors* (M. J. Selander, ed.), vol. 3240, pp. 242–250, SPIE, 1998. 10

[25] D. M. Sheen, D. L. Mcmakin, and T. E. Hall, “Three-dimensional millimeter-wave imaging for concealed weapon detection,” *IEEE Transactions on Microwave Theory and Techniques*, vol. 49, no. 9, pp. 1581–1592, 2001. 10

[26] E. Gerecht, D. Gu, L. You, and K. S. Yngvesson, “A passive heterodyne hot electron bolometer imager operating at 850 GHz,” *IEEE Transactions on Microwave Theory and Techniques*, vol. 56, no. 5, pp. 1083–1091, 2008. 11

[27] R. J. Dengler, A. Skalare, and P. H. Siegel, “Passive and active imaging of humans for contraband detection at 640 GHz,” in *IEEE MTT-S International Microwave Symposium*, vol. 3, pp. 1591–1594, 2004. 11

[28] P. F. Goldsmith, C. T. Hsieh, G. R. Huguenin, J. Kapitzky, and E. L. Moore, “Focal plane imaging systems for millimeter wavelengths,” *Microwave Theory and Techniques, IEEE Transactions on*, vol. 41, no. 10, pp. 1664–1675, 1993. 11, 122

[29] G. S. Dow, D. C. W. Lo, Y. Guo, E. W. Lin, T. T. Chung, M. D. Biedenbender,

O. Miromontes, A. Marashi, L. Yujiri, P. S. C. Lee, M. M. Shoucri, and B. R. Allen, "Large scale W-band focal plane array for passive radiometric imaging," in *IEEE MTT-S International Microwave Symposium*, vol. 1, pp. 369–372, 1996. 11

[30] L. Yujiri, M. Shoucri, and P. Moffa, "Passive millimeter wave imaging," *Microwave Magazine, IEEE*, vol. 4, no. 3, pp. 39–50, 2003. 12

[31] L. Yujiri, "Passive millimeter wave imaging," in *Microwave Symposium Digest, 2006. IEEE MTT-S International*, pp. 98–101, 2006. 12

[32] R. Appleby, R. N. Anderton, S. Price, N. A. Salmon, G. N. Sinclair, J. R. Borrill, P. R. Coward, V. P. Papakosta, A. H. Lettington, and D. A. Robertson, "Compact real-time (video rate) passive millimeter-wave imager," vol. 3703, pp. 13–19, SPIE, 1999. 12, 103

[33] R. Appleby, R. N. Anderton, N. H. Thomson, and J. W. Jack, "The design of a real-time 94-GHz passive millimetre-wave imager for helicopter operations," in *Passive Millimetre-Wave and Terahertz Imaging and Technology* (R. Appleby, M. J. Chamberlain, and K. A. Krapels, eds.), vol. 5619, pp. 38–46, SPIE, 2004. 12, 92, 103

[34] R. G. Humphreys, S. M. Taylor, P. A. Manning, P. D. Munday, and J. Powell, "Performance of 94 GHz receivers for passive imaging," in *Passive Millimeter-Wave Imaging Technology* (R. Appleby and D. A. Wikner, eds.), vol. 6548, SPIE, 2007. 13

[35] R. Piesiewicz, C. Jansen, S. Wietzke, D. Mittleman, M. Koch, and T. Kurner, "Properties of building and plastic materials in the THz range," *International Journal of Infrared and Millimeter Waves*, vol. 28, pp. 363–371, May 2007. 14, 75, 81, 82, 89, 122

[36] E. R. Brown, J. E. Bjarnason, T. L. J. Chan, D. C. Driscoll, M. Hanson, and A. C. Gossard, "Room temperature, THz photomixing sweep oscillator and its application to spectroscopic transmission through organic materials," *Review of Scientific Instruments*, vol. 75, no. 12, pp. 5333–5342, 2004. 14

[37] J. R. Demers, R. T. Logan, and E. R. Brown, "An optically integrated coherent frequency-domain THz spectrometer with signal-to-noise ratio up to 80 dB," in *IEEE International Topical Meeting on Microwave Photonics*, pp. 92–95, 2007. 14

[38] R. Mcgee and H. B. Wallace, "Assessment of millimeter-wave and terahertz technology for detection and identification of concealed weapons and explosives," tech. rep., National Academy of Sciences, Washington, D.C. 19

[39] M. Noda, K. Hashimoto, R. Kubo, H. Tanaka, T. Mukaigawa, H. Xu, and M. Okuyama,

"A new type of dielectric bolometer mode of detector pixel using ferroelectric thin film capacitors for infrared image sensor," *Sensors and Actuators A: Physical*, vol. 77, pp. 39–44, September 1999. 22

[40] J. Maserjian, "A thin-film capacitive bolometer," *Applied Optics*, vol. 9, pp. 307+, February 1970. 22

[41] J. E. Sauvageau and D. G. Mcdonald, "Superconducting kinetic inductance bolometer," *IEEE Transactions on Magnetics*, vol. 25, no. 2, pp. 1331–1334, 1989. 22

[42] E. N. Grossman, D. G. Mcdonald, and J. E. Sauvageau, "Far-infrared kinetic-inductance detectors," *IEEE Transactions on Magnetics*, vol. 27, no. 2, pp. 2677–2680, 1991. 22

[43] R. A. Wood, "Monolithic silicon microbolometer arrays," in *Uncooled Infrared Imaging Arrays and Systems* (P. W. Kruse and D. D. Skatrud, eds.), vol. 47, pp. 43–122, Academic Press, October 1997. 22, 23

[44] E. N. Grossman, J. E. Sauvageau, and D. G. Mcdonald, "Lithographic spiral antennas at short wavelengths," *Applied Physics Letters*, vol. 59, no. 25, pp. 3225–3227, 1991. 23

[45] D. P. Neikirk, W. W. Lam, and D. B. Rutledge, "Far-infrared microbolometer detectors," *International Journal of Infrared and Millimeter Waves*, vol. 5, pp. 245–278, March 1984. 23

[46] M. E. Macdonald and E. N. Grossman, "Niobium microbolometers for far-infrared detection," *Microwave Theory and Techniques, IEEE Transactions on*, vol. 43, no. 4, pp. 893–896, 1995. 23, 36

[47] A. Rahman, G. de Lange, and Q. Hu, "Micromachined room-temperature microbolometers for millimeter-wave detection," *Applied Physics Letters*, vol. 68, no. 14, pp. 2020–2022, 1996. 23

[48] M. Gurvitch, M. A. Washington, and H. A. Huggins, "High quality refractory josephson tunnel junctions utilizing thin aluminum layers," *Applied Physics Letters*, vol. 42, no. 5, pp. 472–474, 1983. 24

[49] A. Luukanen, E. N. Grossman, A. J. Miller, P. Helistö, J. S. Penttilä, H. Sipola, and H. Seppä, "An ultra-low noise superconducting antenna-coupled microbolometer with a room-temperature read-out," *IEEE Microwave and Wireless Components Letters*, vol. 16, no. 8, pp. 464–466, 2006. 24, 30, 37, 76

[50] A. Luukanen, *High performance microbolometers and microcalorimeters: from 300 K to 100 mK*. PhD thesis, Department of Physics, University of Jyväskylä, 2003. 24, 27

[51] W. D. Floet, J. J. A. Baselmans, T. M. Klapwijk, and J. R. Gao, "Resistive transition of niobium superconducting hot-electron bolometer mixers," *Applied Physics Letters*, vol. 73, no. 19, pp. 2826–2828, 1998. 24

[52] W. D. Floet, E. Miedema, T. M. Klapwijk, and J. R. Gao, "Hotspot mixing: A framework for heterodyne mixing in superconducting hot-electron bolometers," *Applied Physics Letters*, vol. 74, no. 3, pp. 433–435, 1999. 24

[53] W. J. Skocpol, M. R. Beasley, and M. Tinkham, "Self-heating hotspots in superconducting thin-film microbridges," *Journal of Applied Physics*, vol. 45, no. 9, pp. 4054–4066, 1974. 24

[54] A. Nigro, G. Nobile, M. G. Rubino, and R. Vaglio, "Electrical resistivity of polycrystalline niobium nitride films," *Physical Review B*, vol. 37, pp. 3970+, March 1988. 25

[55] R. C. Jones, "General theory of bolometer performance," *Journal of the Optical Society of America*, vol. 43, pp. 1+, January 1953. 25

[56] J. C. Mather, "Bolometer noise: nonequilibrium theory," *Applied Optics*, vol. 21, pp. 1125–1129, March 1982. 25, 29

[57] J. C. Mather, "Bolometers: ultimate sensitivity, optimization, and amplifier coupling," *Applied Optics*, vol. 23, pp. 584+, February 1984. 25

[58] P. L. Richards, "Bolometers for infrared and millimeter waves," *Journal of Applied Physics*, vol. 76, no. 1, pp. 1–24, 1994. 25, 26

[59] D. P. Neikirk and D. B. Rutledge, "Air-bridge microbolometer for far-infrared detection," *Applied Physics Letters*, vol. 44, no. 2, pp. 153–155, 1984. 26

[60] J. S. Penttilä, H. Sipola, P. Helistö, and H. Seppä, "Low-noise readout of superconducting bolometers based on electrothermal feedback," *Superconductor Science and Technology*, vol. 19, pp. 319–322, April 2006. 28, 30, 36, 37, 76, 105

[61] P. Helistö, J. S. Penttilä, H. Sipola, L. Grönberg, F. Maibaum, A. Luukanen, and H. Seppä, "Nbn vacuum bridge bolometer arrays with room temperature readout approaching photon noise limited THz imaging applications," *IEEE Transactions on Applied Superconductivity*, vol. 17, no. 2, pp. 310–313, 2007. 30

[62] A. Luukanen, A. J. Miller, and E. N. Grossman, "Passive hyperspectral terahertz imagery for security screening using a cryogenic microbolometer," in *Passive Millimeter-Wave Imaging Technology* (R. Appleby and D. A. Wikner, eds.), vol. 5789, pp. 127–134, SPIE, 2005. 31, 92, 106, 116

[63] T. H. Büttgenbach, "An improved solution for integrated array optics in quasi-optical mm and submm receivers: the hybrid antenna," *Microwave Theory and Techniques, IEEE Transactions on*, vol. 41, no. 10, pp. 1750–1760, 1993. 34, 46, 76

[64] J. E. Carlstrom, R. L. Plambeck, and D. D. Thornton, "A continuously tunable 65-115-ghz gunn oscillator," *IEEE Transactions on Microwave Theory Techniques*, vol. 33, pp. 610–619, July 1985. 36

[65] E. N. Grossman, "The coupling of submillimeter corner-cube antennas to Gaussian beams," *Infrared Physics*, vol. 29, pp. 875–885, July 1989. 45

[66] D. B. Rutledge, D. P. Neikirk, and D. P. Kasilingam, "Integrated circuit antennas," in *Infrared and Millimeter Waves* (K. J. Button, ed.), vol. 10, pp. 1–90, New York: Academic Press, 1983. 46, 76

[67] T. H. Büttgenbach, R. E. Miller, M. J. Wengler, D. M. Watson, and T. G. Phillips, "A broad-band low-noise SIS receiver for submillimeter astronomy," *IEEE Transactions on Microwave Theory and Techniques*, vol. 36, no. 12, pp. 1720–1726, 1988. 46, 76

[68] D. F. Filipovic, S. S. Gearhart, and G. M. Rebeiz, "Double-slot antennas on extended hemispherical and elliptical silicon dielectric lenses," *Microwave Theory and Techniques, IEEE Transactions on*, vol. 41, no. 10, pp. 1738–1749, 1993. 46, 76

[69] D. L. Woolard, R. Brown, M. Pepper, and M. Kemp, "Terahertz frequency sensing and imaging: A time of reckoning future applications?," *Proceedings of the IEEE*, vol. 93, no. 10, pp. 1722–1743, 2005. 49

[70] P. H. Siegel, "Terahertz technology," *IEEE Transactions on Microwave Theory and Techniques*, vol. 50, no. 3, pp. 910–928, 2002. 49

[71] P. H. Siegel, "Terahertz technology in biology and medicine," *IEEE Transactions on Microwave Theory and Techniques*, vol. 52, no. 10, pp. 2438–2447, 2004. 49

[72] J. Randa, D. K. Walker, A. E. Cox, and R. L. Billinger, "Errors resulting from the reflectivity of calibration targets," *IEEE Transactions on Geoscience and Remote Sensing*, vol. 43, no. 1, pp. 50–58, 2005. 49

[73] K. Foster and T. Hewison, "The absolute calibration of total power millimeter-wave airborne radiometers," in *IEEE International Geoscience and Remote Sensing Symposium*, vol. 1, pp. 384–386, 1998. 49, 51

[74] J. A. Shaw and L. S. Fedor, "Improved calibration of infrared radiometers for cloud temperature remote sensing," *Optical Engineering*, vol. 32, no. 5, pp. 1002–1010, 1993. 50

[75] I. M. Mason, P. H. Sheather, J. A. Bowles, and G. Davies, "Blackbody calibration sources of high accuracy for a spaceborne infrared instrument: the Along Track Scanning Radiometer," *Applied Optics*, vol. 35, pp. 629+, February 1996. 50

[76] A. C. Parr, "A national measurement system for radiometry, photometry, and pyrometry based upon absolute detectors." 50

[77] H. W. Yoon, C. E. Gibson, and P. Y. Barnes, "Realization of the National Institute of Standards and Technology detector-based spectral irradiance scale," *Applied Optics*, vol. 41, pp. 5879–5890, October 2002. 50

[78] G. T. Fraser, C. E. Gibson, H. W. Yoon, and A. C. Parr, ""once is enough" in radiometric calibrations," *Journal of Research of the National Institute of Standards and Technology*, vol. 112, no. 1, pp. 39–51, 2007. 50

[79] F. Hengstberger, *Absolute Radiometry.* Academic Press, 1989. 50

[80] E. N. Grossman, C. R. Dietlein, and A. Luukanen, "Terahertz circularly variable filters," in *Proceedings of the 4th ESA workshop on millimetre-wave technology and applications*, pp. 353–358, 2006. 50, 122, 125, 126

[81] M. E. Macdonald, A. Alexanian, R. A. York, Z. Popovic, and E. N. Grossman, "Spectral transmittance of lossy printed resonant-grid terahertz bandpass filters," *Microwave Theory and Techniques, IEEE Transactions on*, vol. 48, no. 4, pp. 712–718, 2000. 50

[82] D. W. Porterfield, J. L. Hesler, R. Densing, E. R. Mueller, T. W. Crowe, and Weikle, "Resonant metal-mesh bandpass filters for the far infrared," *Appl. Opt.*, vol. 33, no. 25, pp. 6046+, 1994. 50

[83] R. H. Giles and T. M. Horgan, "Method for absorbing radiation." United States Patent no. 5,260,513, 1993. 50

[84] P. F. Goldsmith, R. A. Kot, and R. S. Iwasaki, "Microwave radiometer blackbody calibration

standard for use at millimeter wavelengths," *Review of Scientific Instruments*, vol. 50, no. 9, pp. 1120–1122, 1979. 51

[85] P. H. Siegel, R. H. Tuffias, and P. Goy, "A simple millimeter-wave blackbody load," in *Proceedings of the 9th international conference on space THz technology*, pp. 1–10, 1998. 51

[86] A. Cox, J. O'Connell, and J. Rice, "Initial results from the infrared calibration and infrared imaging of a microwave calibration target," in *IEEE International Conference on Geoscience and Remote Sensing Symposium*, pp. 3463–3465, 2006. 51

[87] J. B. Fowler, "A third generation water bath based blackbody source," *Journal of Research of the National Institute of Standards and Technology*, vol. 100, no. 5, pp. 591–599, 1995. 51

[88] N. P. Fox, "Trap detectors and their properties," *Metrologia*, vol. 28, no. 3, pp. 197–202, 1991. 52

[89] J. L. Gardner, "Transmission trap detectors," *Applied Optics*, vol. 33, no. 25, pp. 5914+, 1994. 52

[90] J. H. Lehman and C. L. Cromer, "Optical trap detector for calibration of optical fiber powermeters: Coupling efficiency," *Applied Optics*, vol. 41, pp. 6531–6536, November 2002. 52

[91] J. H. Lehman and C. L. Cromer, "Optical tunnel-trap detector for radiometric measurements," *Metrologia*, vol. 37, no. 5, pp. 477–480, 2000. 52

[92] B. N. Taylor and C. E. Kuyatt, *Guidelines for evaluating and expressing the uncertainty of NIST measurement results*, 1994. 56, 71

[93] "Industrial platinum resistance thermometer sensors," tech. rep., International Electrotechnical Commission, January 1996. 57

[94] J. Xu, K. W. Plaxco, J. S. Allen, J. E. Bjarnason, and E. R. Brown, "0.15–3.72 THz absorption of aqueous salts and saline solutions," *Applied Physics Letters*, vol. 90, no. 3, 2007. 60

[95] C. Ronne, L. Thrane, P.-O. åstrand, A. Wallqvist, K. V. Mikkelsen, and S. R. Keiding, "Investigation of the temperature dependence of dielectric relaxation in liquid water by THz

reflection spectroscopy and molecular dynamics simulation," *Journal of Chemical Physics*, vol. 107, no. 14, pp. 5319–5331, 1997. 60, 61, 65, 66, 73

[96] J. M. Bennet and L. Mattsson, *Introduction to surface roughness and scattering.* Washington D.C.: Optical Society of America, 1989. 62, 67

[97] E. L. Shirley, "Revised formulas for diffraction effects with point and extended sources," *Appl. Opt.*, vol. 37, pp. 6581–6590, October 1998. 63, 67

[98] E. L. Shirley, "Fraunhofer diffraction effects on total power for a planckian source," *Journal of Research of the National Institute of Standards and Technology*, vol. 106, pp. 775–779, 2001. 63, 67

[99] P. F. Goldsmith, *Quasioptical Systems.* Piscataway, NJ: IEEE Press, 1998. 68, 92, 99

[100] J. E. Bjarnason, T. L. J. Chan, A. W. M. Lee, M. A. Celis, and E. R. Brown, "Millimeter-wave, terahertz, and mid-infrared transmission through common clothing," *Applied Physics Letters*, vol. 85, no. 4, pp. 519–521, 2004. 75, 107, 122

[101] N. A. Salmon, R. Appleby, and S. Price, "Scene simulation of passive millimeter-wave images of plastic and metal objects," in *Infrared and Passive Millimeter-wave Imaging Systems: Design, Analysis, Modeling, and Testing* (R. Appleby, G. C. Holst, and D. A. Wikner, eds.), vol. 4719, pp. 397–401, SPIE, 2002. 75

[102] N. A. Salmon, "Polarimetric scene simulation in millimeter-wave radiometric imaging," in *Radar Sensor Technology and Passive Millimeter-Wave Imaging Technology* (R. Trebits, J. L. Kurtz, R. Appleby, N. A. Salmon, and D. A. Wikner, eds.), vol. 5410, pp. 260–269, SPIE, 2004. 75

[103] R. Appleby and M. L. Musselwhite, "Millimeter-wave reflectometer," in *Infrared and Passive Millimeter-wave Imaging Systems: Design, Analysis, Modeling, and Testing* (R. Appleby, G. C. Holst, and D. A. Wikner, eds.), vol. 4719, pp. 402–408, SPIE, 2002. 75

[104] A. T. Lee, P. L. Richards, S. W. Nam, B. Cabrera, and K. D. Irwin, "A superconducting bolometer with strong electrothermal feedback," *Applied Physics Letters*, vol. 69, no. 12, pp. 1801–1803, 1996. 76

[105] D. Rogers, "Private communication," 2006. 79

[106] C. F. Bohren and D. R. Huffman, *Absorption and scattering of light by small particles.* Wiley-VCH, 1998. 82

[107] M. Plonus, "Theoretical investigations of scattering from plastic foams," *IEEE Transactions on Antennas and Propagation*, vol. 13, no. 1, pp. 88–94, 1965. 84

[108] H. Suess, K. Gruener, and W. J. Wilson, "Passive millimeter-wave imaging - a tool for remote sensing," *Alta Frequenza*, vol. 58, pp. 457–465, December 1989. 92

[109] R. Appleby, R. N. Anderton, S. Price, N. A. Salmon, G. N. Sinclair, P. R. Coward, A. R. Barnes, P. D. Munday, M. Moore, A. H. Lettington, and D. A. Robertson, "Mechanically scanned real-time passive millimeter-wave imaging at 94 GHz," in *Passive Millimeter-Wave Imaging Technology and Radar Sensor Technology* (R. Appleby, D. A. Wikner, R. Trebits, and J. L. Kurtz, eds.), vol. 5077, pp. 1–6, SPIE, 2003. 92, 103

[110] K. S. Min, J. Hirokawa, K. Sakurai, M. Ando, and N. Goto, "Single-layer dipole array for linear-to-circular polarisation conversion of slotted waveguide array," *IEE Proceedings on Microwaves, Antennas and Propagation*, vol. 143, no. 3, pp. 211–216, 1996. 93

[111] S. Hollung, W. Shiroma, M. Markovic, and Z. Popović, "A quasi-optical isolator," *IEEE Microwave and Guided Wave Letters*, vol. 6, no. 5, pp. 205–206, 1996. 93

[112] W. A. Shiroma, S. C. Bundy, S. Hollung, B. D. Bauernfeind, and Z. Popović, "Cascaded active and passive quasi-optical grids," *IEEE Transactions on Microwave Theory and Techniques*, vol. 43, no. 12, pp. 2904–2909, 1995. 93

[113] J. Bornemann, "Computer-aided design of multilayered dielectric frequency-selective surfaces for circularly polarized millimeter-wave applications," *IEEE Transactions on Antennas and Propagation*, vol. 41, no. 11, pp. 1588–1591, 1993. 93

[114] H. L. Bertoni, Cheo, and T. Tamir, "Frequency-selective reflection and transmission by a periodic dielectric layer," *IEEE Transactions on Antennas and Propagation*, vol. 37, no. 1, pp. 78–83, 1989. 93

[115] L. Young, L. Robinson, and C. Hacking, "Meander-line polarizer," *IEEE Transactions on Antennas and Propagation*, vol. 21, no. 3, pp. 376–378, 1973. 93

[116] T.-K. Wu, "Meander-line polarizer for arbitrary rotation of linear polarization," *IEEE Microwave and Guided Wave Letters*, vol. 4, no. 6, pp. 199–201, 1994. 93

[117] E. Ongareau, A. Roussaud, E. Marouby, and J. R. Levrel, "Radar cross-section reduction by polarization rotation," *Microwave and Optical Technology Letters*, vol. 8, pp. 316–318, April 1995. 93

[118] D. Lerner, "A wave polarization converter for circular polarization," *IEEE Transactions on Antennas and Propagation*, vol. 13, no. 1, pp. 3–7, 1965. 93

[119] K. M. K. H. Leong and W. Shiroma, "Waffle-grid polariser," *Electronics Letters*, vol. 38, no. 22, pp. 1360–1361, 2002. 93

[120] G. G. Macfarlane, "Quasi-stationary field theory and its application to diaphragms and junctions in transmission lines and waveguides," *Proceedings of the IRE*, vol. 93, pp. 703–719, 1946. 94

[121] S. C. Bundy and Z. Popovic, "A generalized analysis for grid oscillator design," *IEEE Transactions on Microwave Theory and Techniques*, vol. 42, no. 12, pp. 2486–2491, 1994. 94

[122] Z. Popović, *Grid Oscillators.* PhD thesis, California Institute of Technology, Pasedena, CA, 1990. 96

[123] T.-K. Wu, *Frequency Selective Surface and Grid Array.* New York: John Wiley and Sons, 1995. 99

[124] S. R. Murrill, E. L. Jacobs, S. K. Moyer, C. E. Halford, S. T. Griffin, F. C. De Lucia, D. T. Petkie, and C. C. Franck, "Terahertz imaging system performance model for concealed weapon identification," in *Passive Millimetre-Wave and Terahertz Imaging II* (D. H. Titterton, S. M. Kirkpatrick, R. Stoian, R. Appleby, J. M. Chamberlain, and K. A. Krapels, eds.), vol. 5989 of *Presented at the Society of Photo-Optical Instrumentation Engineers (SPIE) Conference*, pp. 414–427, November 2005. 109, 110, 114

[125] S. R. Murrill, E. L. Jacobs, S. K. Moyer, C. E. Halford, S. T. Griffin, F. C. De Lucia, D. T. Petkie, and C. C. Franck, "Terahertz imaging system performance model for concealed-weapon identification," *Applied Optics*, vol. 47, pp. 1286–1297, March 2008. 109, 110, 114

[126] G. D. Boreman, *Modulation Transfer Function in Optical and Electro-Optical Systems.* Bellingham, WA: SPIE Press Tutorial Texts in Optical Engineering, 2001. 113

[127] M. Born and E. Wolf, *Principles of Optics: Electromagnetic Theory of Propagation, In-*

terference and Diffraction of Light. Cambridge, England: Cambridge University Press, seventh ed., October 1999. 115

[128] E. R. Brown, K. A. Mcintosh, K. B. Nichols, and C. L. Dennis, "Photomixing up to 3.8 THz in low-temperature-grown GaAs," *Applied Physics Letters*, vol. 66, no. 3, pp. 285–287, 1995. 117

[129] E. N. Grossman, C. R. Dietlein, J. D. Chisum, A. Luukanen, J. E. Bjarnasson, and E. R. Brown, "Spectral decomposition of ultra-wide-band terahertz imagery," in *Passive Millimeter-Wave Imaging Technology* (R. Appleby and D. A. Wikner, eds.), vol. 6548, SPIE, 2007. 117

[130] T. H. J. M. Brake and G. F. M. Wiegerinck, "Low-power cryocooler survey," *Cryogenics*, vol. 42, pp. 705–718, November 2002. 118

[131] E. N. Grossman, C. R. Dietlein, J. E. Bjarnason, M. D. Ramírez, M. Leivo, J. S. Penttilä, P. Helistö, and A. Luukanen, "Imaging with modular linear arrays of cryogenic Nb microbolometers," in *Passive Millimeter-Wave Imaging Technology* (R. Appleby and D. A. Wikner, eds.), vol. 6948, SPIE, 2008. 118